

Posters from ICCF-19

Padua (Italy), 13-17 April 2015

Source of images: <http://tinyurl.com/o34uvrn>

Current status of the theory and modelling effort based on fractionation

Peter L. Hagelstein
Massachusetts Institute of Technology, USA

The theory problem...

- Biggest issue is absence of energetic nuclear radiation
- Implies that it should be possible to down-convert a large 24 MeV quantum
- Need a model to do it
- But nuclei don't interact much on atomic scale
- Need a stronger interaction between nuclei and environment
- Also note that theory problem involves both known physics and new physics

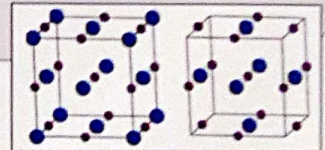
Interaction between vibrations and nuclei

- From comparison of models with experiment, know now that interactions must be pretty strong
- Second-order coupling not going to do the job
- Proposed relativistic coupling in 2012
- Have been issues along the way, but still looks like best option
- Get fundamental Hamiltonian consistent with standard model

Vacancies and D₂ inside the lattice

- D₂ cannot exist in bulk Pd because background electron density too high
- Lower electron density near vacancies
- Interested in possibility of D₂ formation in monovacancies
- Analog at right energy known for H₂ at surface site of PdH
- Vacancies thermodynamically favored above D/Pd = 0.95
- Candidate explanation for SRI loading criterion
- Consistent with Letts high current density codeposition protocol
- Could use NMR to prove/disprove

Superabundant vacancies
observed in PdH when time for
atomic self diffusion



New condensed matter Hamiltonian:

$$\hat{H} = \sum_j \mathbf{M}_j c^2 + \mathbf{a}_j \cdot c \hat{\mathbf{p}}_j + \sum_k \frac{|\hat{\mathbf{p}}_k|^2}{2m} + \sum_{j \neq j'} \frac{Z_j Z_{j'} e^2}{4\pi\epsilon_0 |\mathbf{R}_j - \mathbf{R}_{j'}|} + \sum_{k,k'} \frac{e^2}{4\pi\epsilon_0 |\mathbf{r}_j - \mathbf{r}_{j'}|} + \sum_{j,k} \frac{Z_j e^2}{4\pi\epsilon_0 |\mathbf{R}_j - \mathbf{r}_k|}$$

relativistic interaction between nuclei and vibrations electronic kinetic energy Coulomb interactions; electron-electron, nuclear-nuclear, and electron-nuclear

Multi-quantum coherent energy exchange

- How to split up big MeV quantum into lots of small meV quanta?
- Found in 2002 could be done with a lossy spin-boson model
- Numerical results, analytic results, asymptotic results, scaling laws all give consistent results for effect and rates
- But approach used only gives limit of when it works as good as possible
- Want new formulation to model between turn-on and maximum coherent energy exchange rate

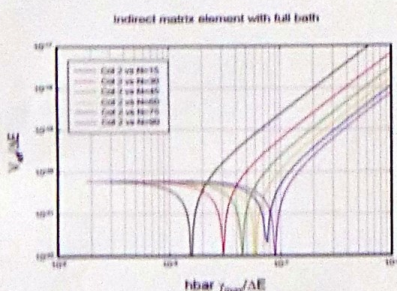
Work with more sophisticated model for fractionation:

$$\hat{H} = \Delta E \frac{\hat{S}_z}{\hbar} + \hbar \omega_0 \hat{a}^\dagger \hat{a} + V \frac{2\hat{S}_z}{\hbar} (\hat{a} + \hat{a}^\dagger) + \sum_j \epsilon_j \hat{b}_j^\dagger \hat{b}_j + \sum_j U_j (\hat{b}_j + \hat{b}_j^\dagger) (\hat{a} + \hat{a}^\dagger)$$

spin-boson model loss model

two-level systems oscillator linear coupling bath coupling between oscillator and bath

Can see enhancement due to loss first turn on...



New nuclear model:

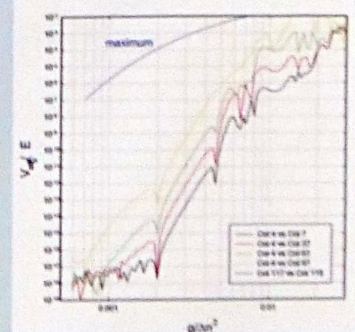
$$\hat{H} = \sum_j (\mathbf{M}_j c^2 + \mathbf{a}_j \cdot c \hat{\mathbf{p}}_j) + \sum_{j,k} \hat{\mathbf{p}}_{jk}$$

Now have first nucleon \mathbf{M} and \mathbf{a} matrices

What is new?

- Some progress working with more sophisticated models
- Wanted to see if crude model used earlier is limit of general model – some evidence now that it is
- Some ability now to work with realistic loss models
- New picture/interpretation for Karabut experiment
- Now expect to connect theory with experiment in normal regime (probably don't require anomalous regime)
- First version of new model for nucleon now consistent with general approach
- Some understanding about how to construct a model for the NANOR
- Progress on development of a simulation model for F&P experiment, also Letts 2-laser experiment

Models with modest loss show substantial multi-quantum exchange rates



- Loss in this calculation is off resonance
- So enhancement doesn't kick in until coupling gets stronger
- Maximum coupling from crude model looks to be relevant!

Electrochemical Analysis of Palladium Cathodes towards the Advancement of Reproducibly High H/Pd Loading Ratios



S. Hamm, O. Dmitriyeva, D. Knies, R. Cantwell, M. McConnell
Coolescence LLC., Boulder, CO 80301 U.S.A

Abstract

Motivation:

- A strong correlation has been found between surface impurities and H/Pd (D/Pd) loading. Impurities that promote increased loadings are referred to as "promoter" impurities.
- Therefore, it is important to understand the effects of these impurities since it is believed there is a higher probability of observing the Fleischmann-Pons Effect when D/Pd > 0.9.
- It is also important to determine how pure Pd in a pure electrolyte theoretically behaves, and whether it would be possible to achieve high loading in such a configuration.

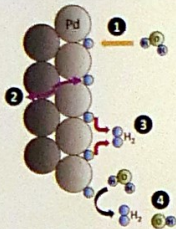
Experimental Approach:

- We are studying the electrochemical properties of surface impurities and how they affect loading/de-loading behavior using impedance spectroscopy (EIS) and chronopotentiometry (CP). Unless otherwise noted, experiments were performed in 0.1 M LiOH in H₂O.
- Copper was chosen as the investigated impurity for the bulk of this work since numerous experiments indicated it to be beneficial toward high loading, and it is easy to electrodeposit and study with electrochemical techniques. Approximately 9 mass equivalent monolayers (ML) – a total mass of roughly 70 µg and charge of about 3.8 mC cm⁻² – of Cu was electrodeposited using 0.5 mM CuSO₄.
- Our group is also currently investigating the effects of Pb, Sn, Zn, Bi, Ni, Fe, and more.

Conclusions:

- The results of our work suggest the surface impurities are the primary aspect controlling the loading, whereas crystal orientation, grain size, crack formation, etc. appear to be secondary effects (see also O. Dmitriyeva and D. Knies presentations).

Reaction Mechanisms



In alkaline solutions:

- 1) $H_2O + M + e^- \leftrightarrow M-H_{ad} + OH^-$ (Volmer)
- 2) $M-H_{ad} \leftrightarrow M-H_{ab}$ (Absorption)
- 3) $2M-H_{ab} \leftrightarrow 2M + H_2$ (Tafel)
- 4) $H_2O + M-H_{ad} + e^- \leftrightarrow M + H_2 + OH^-$ (Heyrovsky)

Note: The mechanisms are the same for H and D

Important Equation:

Simplified Butler-Volmer relationship [Mechanism (1)]:

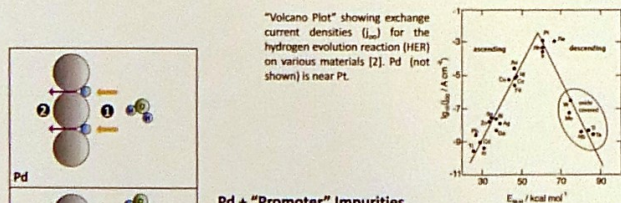
$$j_{tot} = \sum_i j_{oi} (e^{(j_{oi}/j_{tot})} - e^{-(j_{oi}/j_{tot})})$$

j_{tot} = Total current density [A cm⁻²]
 j_{oi} = Exchange current density [A cm⁻²]
 β = Symmetry coefficient
 $f = F/RT$ [V⁻¹]
 η = Overpotential [V]

Effects of Surface Impurities

Increased H/Pd (D/Pd) Loading

High D/Pd loading suggested to increase probability of observing excess heat [1]

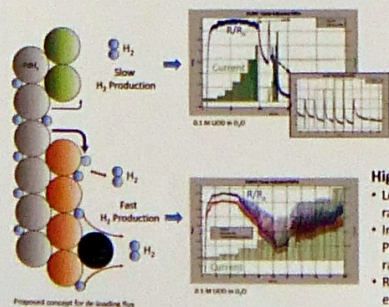


Pd + "Promoter" Impurities

- Current from Volmer reaction focused on exposed Pd due to higher exchange current density (E.C.D.)
 - Increased overpotential needed to achieve same current
 - Rate of H₂ production (specifically from (3)) reduced
 - Hydrogen chemical potential enhanced by adjacent impurities [3]
- We believe some or all of these characteristics play a role in the observed increase in the H/Pd or D/Pd ratio

High- and Low-Flux De-Loading

- High D flux also suggested to increase probability of observing excess heat [1]
- Open circuit interruptions during galvanostatic loading protocol used to test the D flux (how fast D can enter/leave the Pd).



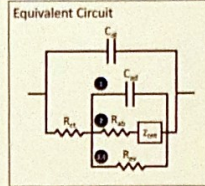
Low Flux "Promoter" Impurities

- Loaded cathodes de-load slowly
- Indicative of slower hydrogen spill-over from PdH (PdD) to impurity surface resulting in slower H₂ production
- Note: Rate is also dependent on H or D/Pd loading

High Flux "Promoter" Impurities

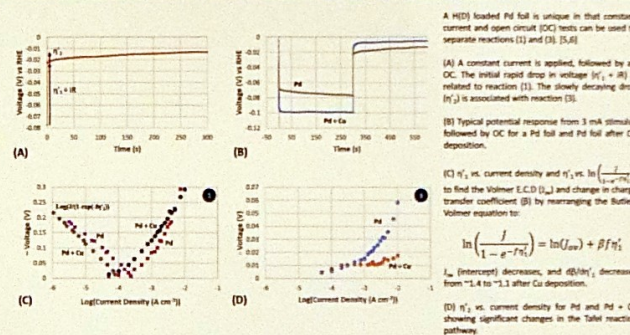
- Loaded cathodes de-load to equilibrium rapidly
- Indicative of fast hydrogen spill-over from PdH (PdD) to impurity surface resulting in rapid H₂ production
- Rate of H₂ production possibly also enhanced by H₂ recombination catalyst, e.g. Pt [4]

Electrochemical Impedance Spectroscopy

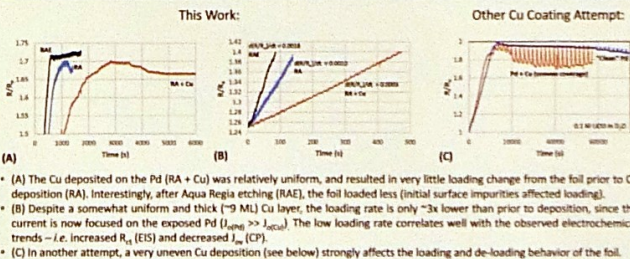


- Impedance data was fitted from 30 kHz to 100 mHz at DC voltages ranging from 0.5 to -0.2 V with a 25 mV signal amplitude. The analysis was performed by fitting the impedance data to the equivalent circuit provided above at each DC voltage point.
- (A) Cu deposition increased the double-layer capacitance (C_{dl}), and thus surface area, by about a factor of two.
- (B) Due to the poor H coverage on Cu at these potentials, the adsorbed capacitance (C_{ad}) is much smaller than before deposition.
- (C) Since $j_{H_{ad}} \ll j_{H_{dep}}$ the Cu-blocked sites increase the charge transfer resistance (R_{ct}).
- (D) The low H coverage on Cu decreases the rate of H₂ evolution, as shown by a significant increase in R_{wp} .

Chronopotentiometry

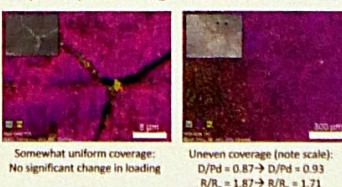


Loading Results



Future Work

Impurity Coverage Matters



Initial studies imply that impurity coverage matters – good coverage affects loading less than bad coverage.

- Further investigate how uniform or uneven impurity coverage affects electrochemical properties and loading.
- Develop methods for controlled deposition (will depend on surface structure).
- Take measurements in split cell to prevent Pt deposition during tests.
- Different types of impurities are currently under investigation.

Conclusions

- Surface impurities clearly affect the total H adsorption coverage, H₂ evolution rate, and rate of absorption and desorption. Electrochemical measurement techniques, such as EIS and Chronopotentiometry, are very useful techniques in investigating the surface reactions and effects of impurities.
- As once proposed, [1] a thin film or some amount of surface coverage of impurities appears to be a simple answer to the question, "How do you reproducibly achieve high D/Pd loading ratios?"
- Whether or not it is the only way is another issue, and stresses the importance of performing experiments in configurations that are as clean as possible (e.g. no copper leads, solder joints, or exposed bolts, even in the electrolytic cell headspace).

References:

- [1] M. C. H. MacKinnon, et al. "New Hydrogen Energy Research at SRL" ECCF-6 NHE Session, 1996.
- [2] R. Quinon, et al. Beilstein J. Nanotechnol. 5, 2014, 840-854
- [3] B. E. Conway, G. Jerkiewicz. J. Electroanal. Chem., 357, 1993, 47-66
- [4] M. D. Marcinkowski, et al. Nature Materials, 12, 2013, 523-528
- [5] T. Maekawa, M. Enyo. Electrochimica Acta, 26(5), 1981, 607-614
- [6] T. Green, D. Britz. J. Electroanal. Chem. 412, 1996, 59-66.

AN ESSAY ON THE UNIFYING THEORY OF NATURAL FORCES

STRUCTURE OF NEUTRON AND PROTON

Mass – Antimass – Dark Mass – Nuclear magnetic moment

TABLE OF CONTENTS

FIRST PART :Showing some equivalences

1. Introduction
 2. Relation of mass and magnetic moment between neutron, proton and electron
 3. Relation between mass of neutron and its dipolar magnetic moment
 4. Schema of the neutron (mass and electromagnetism)
 5. From neutron to proton
 6. The creation of the electron and the antineutrino
 7. The binding energy between nucleons
 8. Conclusion of first part
- Annexes :Schemas 1(1) and 1 (2)
 Schemas 2(1) and 2 (2)
 Schemas 3(1) to 3 (17)
 Schemas 4(1) and 4 (2)
 Figures : binding energy of various atomic nuclei

SECOND PART : Creation of mass, electro-magnetism, pure energy external to the neutron trunk

1. Summary of first part
2. Creation of mass
3. Creation of electro-magnetism
4. Balance of electro-magnetism
5. Outcome of this mechanism
6. Pure energy
7. Conclusion

THIRD PART : Evidences of mass modification

1. Summary of previous part
2. Muon
3. Mesons
4. Baryons
5. Conclusion

FOURTH PART : Generalisation of the system of massification/demassification

1. Introduction
2. The first particles/antiparticles
3. Constitution of neutron
4. The gravitational force

CONCLUSIONS

1. Purpose of the theory
2. Discontinuity of matter
3. Constitution of the neutron
4. Gravitation
5. The action/reaction of the observer – the stroboscopic effect
6. Conclusions according to the map of the universe photographed by the satellite Planck and former satellites
7. Composition of the matter
8. Hierarchy of forces
9. Unitary theory of material universe

Philippe HATT

October 2013

On internet : philippehatt.com

ATOMIC NUCLEI

BINDING ENERGY

Structure of the Atomic Nuclei

TABLE OF CONTENTS

First part: Atomic nuclei binding energy till ${}_8\text{O}^{16}$

1. Hypothesis for the creation of these atomic nuclei
2. Binding energy for each nucleus
 - 2.1. Binding energy of α particle
 - 2.2. Binding energy of other substructures of the nucleus
 - 2.3. Summary
3. Bonds reversibility
4. Competition among bonds
5. Stability of the nucleus and symmetry in the nucleus
 - 5.1. Nuclei made up only of α particles
 - 5.2. Nuclei made up of α particles and N and P external to α particles
6. Attachments – Figures

Second part: Atomic nuclei binding energy from ${}_8\text{O}^{17}$ to ${}_{83}\text{Bi}^{209}$

1. Introduction
 - 1.1. Reference to the general hypothesis
 - 1.2. Binding energy value limit
 - 1.2.1. Remarks concerning this formula
 - 1.2.2. Binding energy limitation causes
2. Analysis of binding energy in some nuclei
3. Attachments – Figures
4. Attachment – Table: atomic nuclei binding energy from ${}_8\text{O}^{17}$ to ${}_{30}\text{Zn}^{68}$
5. Attachment – Table: atomic nuclei binding energy from ${}_{31}\text{Ga}^{69}$ to ${}_{83}\text{Pb}^{204}$
6. Study of the «degree of relationships» among nuclei

Third part: Atomic nuclei binding energy from ${}_{82}\text{Pb}^{206}$ to ${}_{94}\text{Pu}^{239}$

1. Introduction
 - 1.1. Field of study
 - 1.2. Application for the basic formula
 - 1.3. Structure attempt for ${}_{92}\text{U}^{238}$
 - 1.4. Difference of nature of the two types of ${}_{92}\text{U}^{238}$ bonds
2. Uranium family
3. Actinium family
4. Thorium family
5. Neptunium family

Philippe HATT

October 2013

On internet : philippehatt.com



A Study on the Excess Heat Generation in Ni-H Gas Discharge Systems

Chongen Huang, Yue Wang, Kang Shi, Shuichao Lin, Zhongqun Tian

College of Chemistry and Chemical Engineering, Xiamen University, China

e-mail: zqtian@xmu.edu.cn

Introduction

Recently significant progress was achieved in Ni-H gas discharge systems. Defkalion Green Technologies (DGT) reported the excess heat in the Ni-H gas discharge systems in July 2013^[1]. To confirm this very interesting phenomenon, we constructed two gas discharge systems used nickel and hydrogen.

Experiments

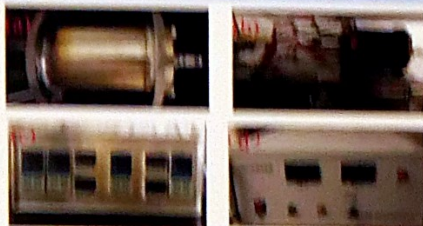


Fig. 1 (a) Reactor device of spark plug, (b) Reactor device of high voltage electrode, (c) The recorder with controlling and detecting, (d) High-voltage DC Power Supply

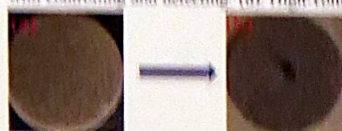


Fig. 3 (a) Ni foam before experiment, (b) Ni foam after experiment

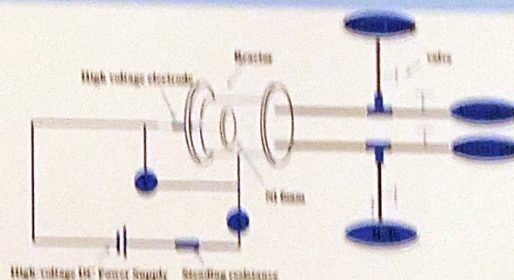


Fig. 2 The circuit of gases and discharge



Fig. 4 Experiment procedure

Results

In the spark plug cell, we investigated the heat effect at different pressures and temperatures, but no excess heat was observed. In the high voltage electrode cell, in several experiments we observed about 20 Watts excess heat when the cell was exposed to H_2 gas at a pressure of 0.2 MPa, which is about 14% of the input power (Fig. 5 (a) and Fig. 5 (b)); we also used the deuterium instead of hydrogen, then observed the heat after death (Fig. 6(a) and Fig. 6(b)). However, we cannot reproduce these phenomena. The more detailed experiments have been performed and will be discussed.

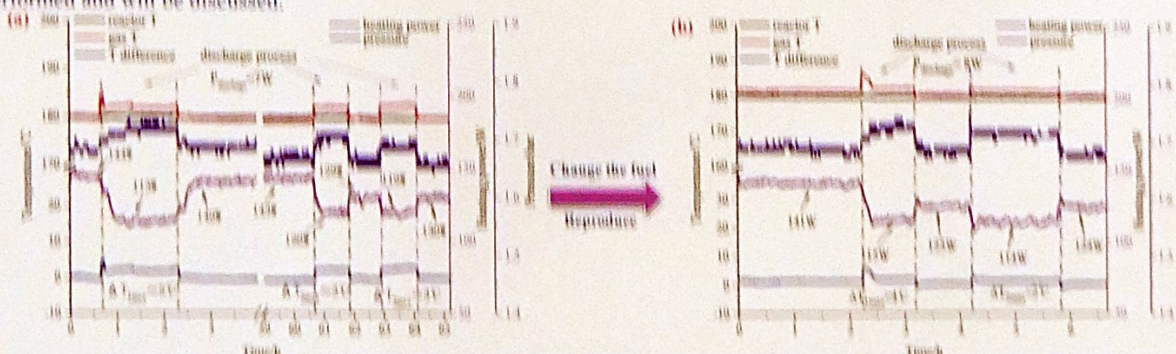


Fig. 5 (a) The abnormal phenomenon of Ni-H discharge experiment in the high voltage electrode device, (b) Reproduces the abnormal phenomenon

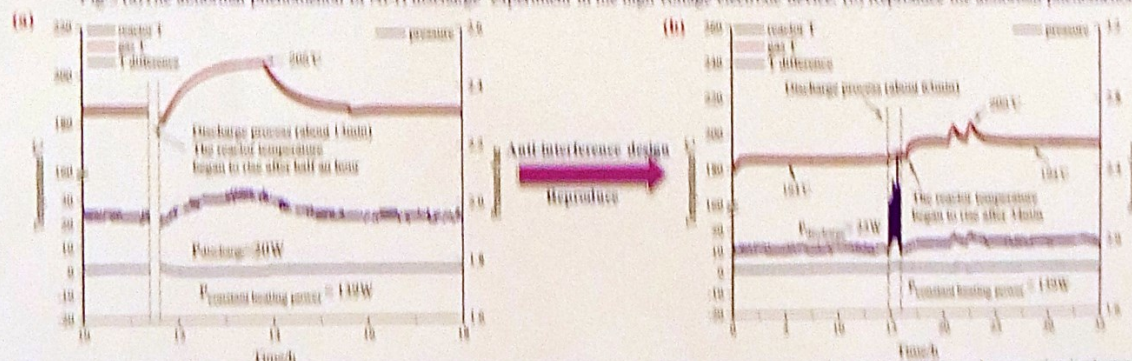


Fig. 6 The heat after death was observed after using the deuterium instead of hydrogen. (a) The data were not recorded during discharge, because the discharge current was not stable which caused computer crashed. (b) The data were recorded by computer normally during discharge, with the addition of anti-interference design.

References

- [1] Y. E. Kim, J. Hadjichristou, "Theoretical Analysis and Reaction Mechanisms for Experimental Results of Hydrogen-Nickel Systems", RCF-18, Columbia, Missouri, 2013.

We are grateful for the financial support by the National Natural Science Fund Committee of China (Program Nos. 31130003).

Observation of RF Emissions in Electrochemical Loading Experiments

D.A. Kidwell,¹ D.D. Dominguez,² K.S. Grabowski,¹ L.F. DeChiaro, Jr.,² and D.L. Knies¹

¹Naval Research Laboratory, Washington, DC 20375, USA
²Naval Research Inc., Alexandria, VA 22304, USA
³Naval Surface Warfare Center Dahlgren, Dahlgren, VA, USA
⁴Corrosion, LLC, Boulder, CO 80501, USA
 (202) 375-3075 David.Kidwell@nrl.navy.mil



Background

- Palladium and palladium-rhodium foil cathodes were electrochemically loaded with deuterium from alkaline solutions of heavy water in specially-designed closed calorimeter cells (Figures 1 & 2)[1].
- Excess energy bursts were observed in the range 2.4 kJ to 44.3 kJ in a small number of these experiments[1].
- Intense RF coincident with the bursts was observed peaking at different frequencies in different cells from about 450 kHz and extending into the MHz range [2].

What is the source of this RF?

Calorimetry Design

Figure 1 - Design of Electrochemical Cells. Designed to be as clean as possible using only PEEK, Pt wires, and Palladium recombination leads with some PVC.



Figure 1 - Internal Design of Heat Calorimeter



One of the heat inserts showing the Palladium recombination and external heat sink. The center is 16 plated AuCu (NPL version).



Shells with two inserts. This is immersed in a precision water bath controlled to 0.01°C. This precise control is necessary for accurate calorimetry.

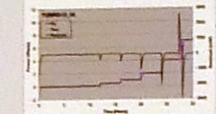


Four precision heat transferable calorimeter. Because of the precise temperature control, the system is stable to 1 mK for days.

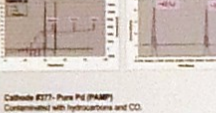
Heat Observations

Three electrolysis cells showed excess heat while being monitored for RF

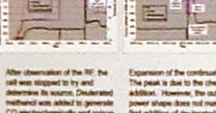
Cathode #54 - Pd₂W₂ Additions not intentionally made



Cathode #60 - Pd₂W₂ Additions as noted



Cathode #377 - Pure Pd (PAMP) Contaminated with hydrocarbons and CO. Additions as noted

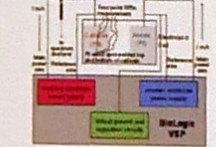


After observation of the RF, the cell was stopped to try and determine its source. Discharged methanol was added to generate CO electrochemically and poison the surface. The black line is the excess power with the spikes due to the chemical addition.

Expansion of the configuration. The peak is due to the chemical addition. However, the output power shape does not match the first addition of disordered methanol shown on the left. The long-term heat has unknown origin.

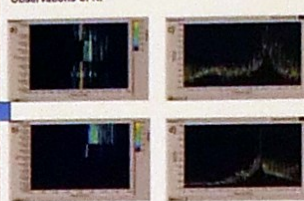
Electrical Set-up and Data Acquisition

- Electrochemistry powered by a Biologic VSP
- RF measured by Rohde & Schwarz RFSD30 (Cathodes #54 and #60) or Signalhound (Cathode #377) frequency analyzers.
- Data recorded with the VSP and Labview programs
- Electrochemistry data taken 1 (VSP)
- Calorimetry data taken 1 (VSP) on Labview
- Frequency data taken 1 (VSP) on Labview

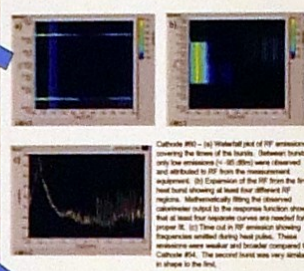


Electrical set-up for Cathode #377. Cathodes #54 and #60 are similar but do not have a four-point probe and reduced a resistor in the main power wire as a cross-correlation of the current supplied by the VSP.

Observations of RF



Cathode #54 - (a) Waterfall plot of RF emission hours before pulse but no excess heat is apparent. The intense emissions at 5.5 MHz of ~30 dB are unusual. (b) Expanded waterfall plot of RF emissions during heat pulse. (c) Time cut in RF emissions showing frequencies emitted before heat pulse. (d) Time cut in RF emissions showing shift in frequencies during heat pulse from 5.8 MHz to 5.5 MHz.



Cathode #60 - (a) Waterfall plot of RF emissions covering the lines of the bursts. Between bursts, only low emissions < 80 dBm were observed and attributed to RF from the measurement equipment. (b) Expansion of the RF from the first heat burst showing at least four different RF regions. Mathematically fitting the observed spectrum yielded the response function shown that at least four separate curves are needed for a proper fit. (c) Time cut in RF emission showing frequencies emitted during heat pulse. These emissions were weaker and broader compared to Cathode #54. The second burst was very similar in shape to the first.



Cathode #377 - (a) Waterfall plot of RF emissions during the period marked with a red arrow. RF was being monitored and almost non-existent throughout the reloaded run except where noted. The initial electrolysis had two primary frequencies at 4.79 MHz and 4.82 MHz whereas the reloaded showed only a broad 4.79 MHz. (b) Waterfall plot of RF emissions during second RF burst. (c-d) Time cuts during the two RF bursts. Note the overtones.

Discussion

RF from an electrochemical cell is unusual. Is it an instrumental artifact?

Arguments against RF being an Instrumental Artifact

- Amplification needed for a RLC, LC, or RLC circuit to oscillate
- Frequencies observed should be too high for the op-amps used in the VSP
- Pick-up of an external signal unlikely
- Cathodes #54 and #60 were monitored in a room shielded from external RF
- Why it ceased immediately when Cathode #377 was stopped would be unexplained.
- RF stopped and started spontaneously
- Frequencies vary greatly with resistance (see below)
- How could a loose connection return to the exact resistance?
- Frequencies not sharp
- Frequencies not the same
- RF rarely present

Arguments for RF being an Instrumental Artifact

- Potentiostats can cause oscillations under certain conditions
- Something changes in the cell to initiate a resonance condition for the VSP
- Toroidal RF pick-up in a one-turn inductor and wire (or inside VSP) is the capacitor
- Could be a LC or RLC oscillator
- As a model, an entirely resistive configuration was constructed (Figure 3)
- Observed frequency varied substantially with the resistance of R1 (Figure 4)
- Change in cell resistance (R2) does not matter
- Resistance may be removed without affecting the frequencies observed
- RF frequency changed from Cathode #54 to #377
- Cannot now reproduce frequency of Cathode #54
- Did some component change over time?
- Cathode #60 had frequencies at ~450 kHz
- Was the RF in Cathode #60 due to a short that overloaded the power supply?
- This is the second harmonic of the main power supply at 150 kHz?
- Why was 150/200 kHz not observed? Was it there?

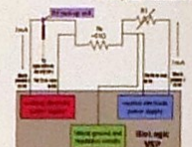


Figure 3 - Experimental design for mimicking Cathode #377. The RF spectrum was taken with a Signalhound 5444D spectrum analyzer scanned from 5 MHz to 20 MHz using 3000 points. RF was varied from 0.6 kΩ. RF was not observed with direct connections nor with resistances above 25Ω.

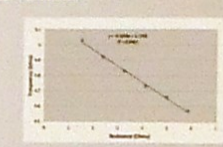


Figure 4 - Variation in frequency vs. resistance from set-up in Figure 3. The resistance of R1 was varied using a potentiometer which checked on a meter 480Ω (calibrated with the potentiometer). The resistance reported does not include resistance of the connectors, which were the same connectors used for Cathode #377. A 3.4 kΩ resistor was calculated to produce 4.82 MHz - the frequency observed from Cathode #377. The frequency decreases not linear with resistance 1/Ω or 1/Ω², and was nearly linear.

Conclusions

- RF was sometimes observed in cells undergoing electrochemical loading.
- Spectrum dependent upon operating conditions and the presence of excess heat production.
- A common signal near 5 MHz could be frequency shifted and its intensity increased (Cathode #60) or decreased (Cathode #54) by excess heat production.
- The source of the RF may arise from inside the cell, but the origin from the cathode or anode is unknown.
- RF generation of these frequencies is unusual with an unknown cause.
- The RF frequency is too high to originate from electrochemistry but may be due to diathermy heating between lattice sites in highly loaded Pd.
- Because RF can be generated under certain conditions, these observations must be interpreted cautiously.

References

- [1] A discussion of the calorimeter set-up and experimental details has appeared in: D.D. Dominguez, D.A. Kidwell, K.S. Grabowski, D.L. Knies, A.E. Miller, and J.H. Wadsworth, "Excess Energy in Palladium-Form Type Electrochemical Experiments", *J. Condensed Matter Sci. Ser.* 14 (2014) 15-28.
- [2] A preliminary account of this work has appeared in: D.A. Kidwell, D.D. Dominguez, K.S. Grabowski, and L.F. DeChiaro, Jr., "Observation of radio frequency emissions from electrochemical loading experiments", *Current Science Special Section: Low Energy Nuclear Reactions*, 188 (2015) 519-521.

Acknowledgements

The views, opinions, and/or findings contained in this presentation are those of the presenter and should not be interpreted as representing the official views or policies, either expressed or implied, of the Naval Research Laboratory or the Department of Defense. Distribution unlimited.

HIGH-ENERGETIC METAL NANO-CLUSTER PLASMOID AND ITS SOFT X-RADIATION

Klimov A., Grigorenko A., Efimov A., Sidorenko M., Soloviev A., Tolkunov B., Evstigneev N., Ryabkov O.
Limited Liability Company "New Inflow"

A.Klimov@newinflow.ru



Abstract

Artificial stable microwave (MW) plasmoid was obtained and studied by Kapitza P. in swirl gas flow at the first time [1]. Physical properties of a longitudinal heterogeneous plasmoid (plasma formation with erosive nano-clusters) created by capacity coupled high-frequency (HF) discharge in high-speed swirl flow have been studied in our works in details. This work is continuation of previous ones [2]–[4] and others. It was obtained that there is extra power release in heterogeneous plasmoid created by combined discharge. The measured COP in this plasmoid was about 2 ± 10 . We suppose that this extra power release in heterogeneous plasmoid is connected with LENR. The obtained experimental results (COP, optical spectra, soft X-ray spectra, chemical composition of dusty particles) prove our suggestion.

Main Ideas. Our approach to LENR.

- Heterogeneous vortex plasmoid (plasma+ metal nano-clusters) [Klimov A.]
- Resonance between plasma electron matter waves and nano-cluster diameter (or surface plasmon- EM wave resonance). [Klimov A., Magnitskii N.]
- Creation of low momentum neutron-like particles. [Magnitskii N.]
- Interaction of low momentum neutron-like particle flux with condensed matter. [Evstigneev N.]

Experimental set up: Plasmoid Vortex Reactors

Main Tasks of this work are the followings:

1. Creation of plasmoid vortex reactor (PVR) with high value of COP.
2. Creation of theoretical physical model of LENR in PVR.

Characteristics and parameters of PVR:

1. Mean extra power output $1 \div 10$ kW
2. COP $\approx 2 \div 10$
3. Testing gas mixture $H_2O : Ar$
4. Mass gas flow < 10 G/s
5. Combined discharge HF+DC
6. Mean power input $0.1 \div 1$ kW



Figure 1: Underwater PWR colorimetry and PWR coaxial gas flow. 1 - Tesla HF generator; 2 - swirl generator; 3 - anode; 4 - nozzle-cathode; 5 - ejector; 6 - flow meter.

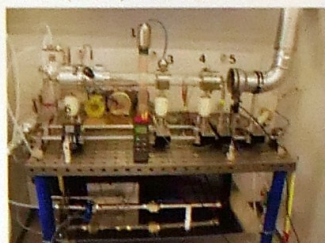


Figure 2: Combined Discharge: HFD+ PRD. Gas mixture $Ar : H_2O = 10 : 1$. Axial velocity V_z is closed tangential velocity V_t : $V_z \sim V_t \sim 30$ m/s, $P_z \sim 1.5$ Bar. 1 - swirl generator; 2 - water steam injector; 3 - erosive metal clusters; 4 - cathode.

Figure 3: PVR. Mixture $H_2O : Ar = 4 : 1$. $K \geq 10$. Anode and Cathode are shown.

Optical Spectrum of Heterogeneous Plasmoid

Swirl flow. Tangential velocity $V_t \sim V_z \sim 30$ m/s.
 $T_e \sim 6000 - 7000$ K; $T_R \sim 2300$ K; $T_b \sim 2000$ K.
 $T_e \gg T_R$

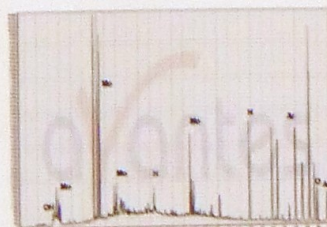


Figure 4: Non-stable plasmoid.

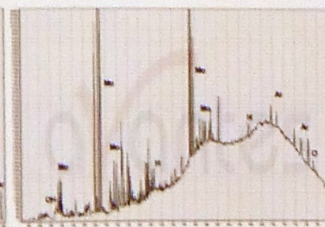


Figure 5: Stable plasmoid \rightarrow total H_2 absorption.

Nano-Cluster Metal-Hydrogen Fuel

Specific heat power of "nano-cluster fuel".
Metal Flow Rate in PVR: $\delta M \approx 10^{-3}$ g/s $\Rightarrow \delta N \approx 10^{19}$ atoms/s.
Extra power output in PVR: $\delta P \approx 3$ kW.
Specific heat power of "nano-cluster fuel": $[Q = \delta P / \delta N = 10^6 \text{ eV/atom}]$



Figure 6: High-Speed Video Frames of Heterogeneous Plasmoid.

X-Radiation from Heterogeneous Plasmoid

Spectrometer X-123SDD records soft X radiation ($0.1 \div 30$ keV) in heterogeneous plasmoid. X-receiver is arranged at different cross sections of PVR testing section and cross sections behind nozzle at $L = 1 \div 100$ cm from it.

- Heterogeneous plasmoid behind PVR nozzle is γ -radioactive. Soft X-radiation $100 \div 10000$ eV from this plasmoid. X-radiation decrement is very small (radiation intensity decrease is about 20% at $L = 100$ cm).
- The main pike $E_1 = 1.3$ keV in X-spectrum is closed to quantum energy of $K_{\alpha 1}$ aluminum line $E_{Al} = 1.487$ keV and $K_{\alpha 1}$ magnesium line $E_{Mg} = 1.254$ keV.
- Additional pikes are located at range up to 10 keV. The pike $E_2 = 4 \div 4.6$ keV corresponds to sum of resonant T_{α}, V, Cr lines.
- It is revealed that maximal value of COP is realized at maximal X - radiation from plasmoid namely.

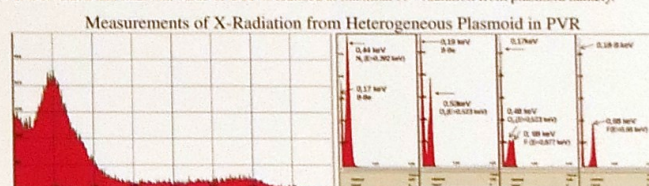


Figure 7: X - Radiation from Heterogeneous Plasma. Figure 8: Spatial Evolution of X - Spectra from Heterogeneous Plasma in PVR. The combined discharge (DC+HF), a mean power - 500W, the hot electrode cathode.

Transmutation of Chemical Elements in Heterogeneous Plasmoid

There is chemical element transmutation in heterogeneous plasmoid. Results obtained by optical spectroscopy, ion mass spectroscopy, X - spectroscopy and α - spectroscopy prove our suggestion about transmutation.

Typical results on chemical element transmutation are shown in the figures. These results are obtained by ion mass spectroscopy. Note that dusty particle composition is the following: $Ni \sim 15\%$, $Si \sim 50\%$, $Fe \sim 9\%$, $Cu \sim 5\%$. Remember that initial composition of Ni -electrode is the following: $Ni \sim 99.99\%$. There is also considerable composition change of exposed electrode surface also. The concentrations of the following chemical elements $Na, Al, Cu, Cr, Mn, Mg, Si, Fe$ are increased considerably on the electrode surface.

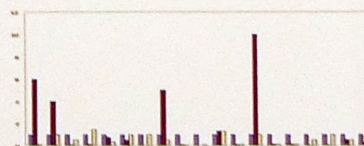


Figure 9: Ion mass spectrometry of Ni -electrodes. Initial electrode; activated electrode (surface); exposed electrode (under surface).

	Si	Ni	Fe	C	Al	Cu	Co	K	Mg
Atom, %	50	14.7	8.9	8.8	6.2	5.1	1.8	1.3	0.4
Mol, %	31	19.2	10.9	2.3	4.7	7.2	2.4	1.1	0.2

Table 1: Dusty particle composition in PVR. Ion Mass spectroscopy analysis. Ni -electrodes 99.99%.

Main Results

1. Parameters of the heterogeneous non-equilibrium plasma are measured in the experimental set up PVR. An electronic temperature estimated by processing of the optical spectra is about $T_e \sim 6000 \div 7000$ K. Planks temperature estimated by the continuous cluster spectrum is about $T_b \sim 2000$ K. A rotational temperature estimated by the molecular band of $AlCl_3$ is about $T_R \sim 2300$ K (aluminum electrodes are used in the experiment). So, it is revealed that there is non-equilibrium heterogeneous plasma in the swirl flow; $T_e \gg T_R, T_b$. According our opinion LERN in nano-cluster plasmoid may be connected with extra energy release in the PVR.
2. It is revealed that the heterogeneous non-equilibrium plasmoid is an intensive source of soft X - radiation of $1 \div 10$ keV quantum energy.
3. There is transmutation of chemical elements in heterogeneous nano-cluster plasmoid. This conclusion is proved by different diagnostic methods, namely: optic spectroscopy, ion mass spectroscopy, X - radiation spectroscopy, α - spectroscopy.
4. $COP \approx 2 \div 10$ is measured in PVR. Estimation of specific energy of " $Ni - H$ fuel" is about 1 KeV/atom.

References

- [1] Kapitza P., "Free plasma filament in high frequency field at high pressure", Zhur. Exp. Teoret. Fiz. vol. 57, no. 6, pp.1801-1806, 1969
- [2] Klimov A., "Vortex Plasmoids Created by High-Frequency Discharges", Atmosphere and Ionosphere: Dynamics, Processes, Monitoring, Springer, Berlin, pp.251-273, 2012.
- [3] Klimov A., Evstigneev N., Moralev I. et al., Vortex Control by Combined Electric Discharge Plasma, AIAA Paper 2013-1040, 51th AIAA Aerospace Sciences Meeting, Dallas, Texas, 2013, P.15
- [4] Klimov A., Calorimetric Measurements in Vortex, Proc. 12th Conf. CNTCE, M. 2005, p.248
- [5] Patent application RU (11) 2014111582, accepted.

Acknowledgements

This work is supported by limited liability company New Inflow. We thank Mr. V. Avdeyehik, Mr. O. Grebenkin, prof. F. Zaitsev, prof. N. Magnitskii, for interest to this Work and fruitful discussions.

ON THE KINETIC CALCULATIONS OF ELEMENTS TRANSMUTATIONS IN THE PRESENCE OF COLD NEUTRON FLUX

Burov D., Evstigneev N., Klimov A., Magnitskii N., Ryabkov O., Zaitsev F.,
Limited Liability Company "New Inflow"

N.Evstigneev@newinflow.ru



http://www.newinflow.ru

Abstract

Our work is based on the hypothesis that at least some of the LENR anomalies (e.g. excess heat production, transmutations [7]) could be explained by appearance of cold or ultracold neutron flux in the LENR active sites [1], [2] and others. There is no common explanation on how these neutrons could be created or how strong gamma radiation from them being captured by nearby atoms could be shielded. However, some qualitative predictions could be derived from this hypothesis even without exact knowledge of neutron production rates. We developed our calculation code supposing the following assumptions. Initially active site contains atoms of chemical elements present in the experiment before it starts with further exposure to the neutron flux of given intensity and energy spectrum (which are for unknown parameters to be estimated yet). Our main goal is to figure out whether some product chemical elements could prevail in such processes and compare them to the conceivably new elements found in LENR experiments. Our preliminary calculations show that at least at some energies of neutron flux certain elements products expose abundance over the others (Li, Mg, Si, S, and Ca). By choosing different sets of initial elements we were able to get large amounts of Carbon and Oxygen.

Main Ideas. Our approach to LENR.

- Heterogeneous vortex plasmoid (plasma+ metal nano-clusters) [Klimov A.]
- Resonance between plasma electron matter waves and nano-cluster diameter (or surface plasmon- EM wave resonance). [Klimov A., Magnitskii N.]
- Creation of low momentum neutron-like particles. [Magnitskii N.]
- Interaction of low momentum neutron-like particle flux with condensed matter. [Evstigneev N.]

Problem Statement

Introduction. There are plenty of evidences of new (absent in original setup composition) chemical elements production during LENR experiments. This production is attributed to unknown nuclear processes. Terms "transmutations" and "elemental anomalies" are usually used to label these phenomena [1], [5] – [6]. There are also evidences of isotopic abundances changes. For example, in [1] possibility of all hydrogen isotopes (up to unstable $4H$) production through the capture of neutrons by hydrogen is considered. The subsequent β^- decay of $4H$ is expected to lead to $4He$. Perhaps the most famous variation among all such hypotheses is Widom and Larsen theory [2]. However all these theoretical constructions have several common bottlenecks:

- Neutron production mechanism is not clear (it is usually accepted that neutrons somehow could be produced from hydrogen).
- Absence of strong gamma rays explanation.
- Quantitative analysis of neutron capture process dynamics.

In the present work its supposed that first two points can be resolved in the context of new mathematical theory of physical vacuum by prof. N.Magnitskii, [3, 4].

Investigation of the last one constitutes the substance of this work.

Problem statement. There were earlier researches where product elements distribution in case of the "neutron" hypothesis was analyzed and compared to the distribution observed in LENR experiments [2], [8]. These tries were based on statistical approaches. Neutron scattering cross section $f(A)$ as a function of nucleus mass A was taken as theoretical prediction of product elements and isotopes distribution. Example of comparative figure can be seen in [8]. On the other hand, it is clear that final distribution of elements after influence of neutron flux depends on interplay of two main factors, which are: rates of neutron captures and decay rates of newly formed radioactive isotopes. Capture cross sections and decay types and half-lives are known experimental data. One could leave neutron production rate and its kinetic energy as free model parameters. In order to simulate this process of interaction between neutrons and matter we used numerical simulation in the present work.

Governing equations and Cauchy problem

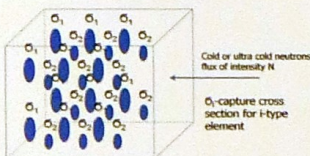


Figure 1: Problem setup for LM neutron captures process simulation.

Cold or ultra cold neutrons production is postulated (any specific mechanism is not involved into consideration). For that problem one can consider the theories, mentioned above. We assume (to a first approximation) that capture cross sections and decay rates in normal environment can be used, i.e. LENR environment does not influence somehow on these processes. Spatially uniform problem is considered for the simplicity state. Program takes into account different isotopes but does not distinguish between nuclear isomers and nuclear excited states with code realization conducted in Python™. Simplified figure for the problem setup of a volume containing elements under consideration is given on Fig.1.

We turn now to the mathematical formulation of the problem. Let X_0 - be the initial concentration distribution of chemical elements in the, supposedly, LENR sites, let N be a neutron flux, prescribed by the information from the experiment (usually estimated through hydrogen absorption rate and measured energy output), $T_{eff}^{Z,A}$ be the half-life time for the element with the concentration $X_{eff}^{Z,A}$, T be the time of an experiment + the time of observation after. Also, let the (n, γ) reaction section $\sigma_{eff}^{Z,A}(E)$ for all chemical elements be known as a function of neutron energy E (we obtain it from open source physical databases, i.e. <https://www-nds.iaea.org/>). We also denote X_T be the final concentration of chemical elements. Then, the Cauchy problem is stated as:

For all given values, described above, find X_T , that:

$$\frac{dX_{eff}^{Z,A}}{dt} = -\sigma_{eff}^{Z,A} X_{eff}^{Z,A} N + \sigma_{eff}^{Z,A-1} X_{eff}^{Z,A-1} N - X_{eff}^{Z,A} k_{Z,A}^{Z,A} (\delta_{\alpha}^{Z,A} + \delta_{\beta}^{Z,A} + \delta_{\gamma}^{Z,A}) + X_{eff}^{Z-1,A} k_{Z-1,A}^{Z-1,A} \delta_{\beta}^{Z-1,A} + X_{eff}^{Z+1,A} k_{Z+1,A}^{Z+1,A} \delta_{\beta}^{Z+1,A}, 0 < t \leq T. \quad (1)$$

$$\delta_{\alpha}^{Z,A} + \delta_{\beta}^{Z,A} + \delta_{\gamma}^{Z,A} \leq 1, \forall \{Z, A\} \in X; k_{Z,A}^{Z,A} = \frac{\ln(2)}{T_{eff}^{Z,A}} \quad (2)$$

And:

$$\sigma_{eff}^{Z,A} = \int_0^{+\infty} \sigma_{eff}^{Z,A}(E) \rho(E) dE, \text{ such, that } \int_0^{+\infty} \rho(E) dE = 1. \quad (3)$$

We use $\rho(E)$ be either monochromatic, or χ^2 distribution.

Numerical method

All this data is fed into the calculation module, thus producing final elements distribution X_T . This distribution is then cross-checked with measurements from experimental data and from papers, see [5], [7]. In the present code we are considering the following reactions, described in the equations (1):

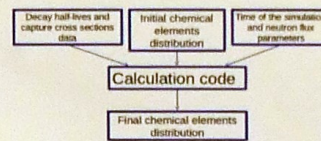
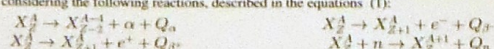


Figure 2: Schematics of the calculation code.

The huge system of about 3500 ODES (1) is being integrated using implicit numerical method. The code was extensively benchmarked and shows excellent agreement with model and well known experimental data.

Results

This research is primarily aimed at comparison of modeled data and experimental data from [7]. Parameters in the numerical experiment were chosen among other things basing on the physical experiment conditions.

Initial abundance corresponded to the one found in electrode (Ni) with all its impurities. Physical time in the range from 1 sec to 600 sec was considered in simulations. Neutron kinetic energies in modeling varied in wide range from $1 \cdot 10^{-5}$ eV up to 0.2 eV. Simulation consisted of two consecutive stages: the "active" one (nonzero neutron flux) and the "passive" one (decays only).

Comparison of relative (normalized to initial amounts) concentrations. Elements with biggest abundance shifts are picked out. Experimental ones are Na, Al, Ca, Mn, Cr . Calculation ones are $F, Na, Mg, Al, Ca, Mn, Cr$, see Fig.3,4

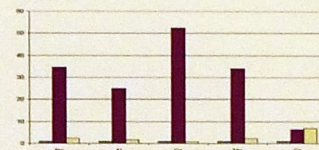


Figure 3: Experimental chemical element distribution from [7] in LENR sites.



Figure 4: Numerical stimulation of chemical element distribution for the experimental condition.

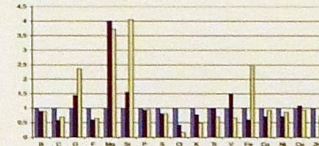


Figure 5: Experimental chemical element distribution from [7] in LENR sites.

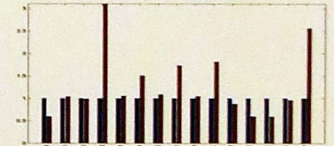


Figure 6: Numerical stimulation of chemical element distribution for the experimental condition.

Comparison of relative concentrations of remainder elements is shown on Fig.5,6 for longer time span. Experimental Mg abundance increased considerably too (though not as much as in the calculation). On the other hand, significant deviation is observed for a number of elements (F, Zn).

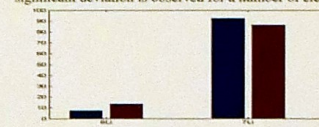


Figure 7: $6Li/7Li$ shift simulation and experimental (in $6Li$ favor) were announced in, e.g. [7].

In addition, some authors of experiment papers and surveys devoted to element transmutations point out the fact that more often there is a shift in isotopic abundance towards heavier isotopes. This process is natural to the considered model and, hence, can be easily obtained. On the other hand, there are claims of the opposite process, particularly $6Li/7Li$ ratio shifts

It turned out that such dynamics may arise in some cases according to the model. It can happen when neutron capture velocity is lower for lighter isotope and its part in natural abundance is also lower. For example, Fig.7 below shows how natural abundance of $6Li/7Li$ equal to 7.50/92.41 changed to 13.5/86.5.

Conclusions

Dynamics of element distribution mainly is "upwards" in terms of atomic number. This rule is only violated by alpha-decay which is more specific for heavy elements. Thus, the given model suggests that in order to get various transmutation products one should consider some sort of "seed", that is, light element. Our computation experiments usually deal with either oxygen or boron in that role.

One can surely conclude that the hydrogen cannot serve as a "seed" for transmutation chains as far as current model is concerned. Instability of $5He$ is the reason.

Assumed kinetic energies of neutrons and neutron flux intensity turned out to be mutually inverse parameters. Seemingly, it has an explanation in the fact that most elements' cross sections obey $\sim 1/v$ asymptotics for a rather wide energy range. A rather stable and settled pattern of generated elements is observed. Generally, those elements are C, O, F, Mg, Si, S, K (to a smaller extent), Ca .

Our future work will be focused on increase of physical parameters as well as on the inverse problem.

References

- [1] R. Godes, R. George, F. Tazella, M. McKubre, Controlled Electron Capture and the Path toward Commercialization, J. Condensed Matter Nucl. Sci., vol.13 pp.127137, 2014.
- [2] A. Widom, L. Larsen Ultra low momentum neutron catalyzed nuclear reactions on metallic hydride surfaces, Eur. Phys. J. C vol.46.1 pp. 107-111, 2006.
- [3] N.A. Magnitskii, Ethereal Model of Neutron, IJRSET, Vol. 3, Issue 12, p.17808-17814, 2014.
- [4] N.A. Magnitskii, Ethereal Models of Electron and Proton, IJRSET, Vol. 3, Issue 11, p.17585-17594, 2014.
- [5] A. Klimov Creation of New Chemical Elements in Water by HF Plasmoid, Proc. Intern. Conf. RCCNT BL-08, Sochi-Dagomys, Russia, pp.15-25, 2008.
- [6] V. Nassisi, G. Carretto and A. Lorusso, Modification of PdH2 and PdD2 Thin Films processed by HeNe Laser, JCMNS, 5, pp.16, 2011.
- [7] A. Klimov, A. Efimov, et al. High-Energetic Nano-Cluster Plasmoid and Its Soft X-radiation, to appear in proceedings of RCCNT-19, 2015.
- [8] F. Scholkmann, David J. Nagel Statistical Analysis of Transmutation Data from Low-energy Nuclear Reaction Experiments and Comparison with a Model-based Prediction of Widom and Larsen // J. Condensed Matter Nucl. Sci. 13 (2014) 485-494.

Acknowledgements

This work is supported by limited liability company New Inflow. We thank Mr. V. Avdeychik and Mr. O. Grebenkin for interest to this Work and fruitful discussions.

On specifics of DD neutron generation along low energy nanosecond vacuum discharge with deuterium-loaded Pd anode

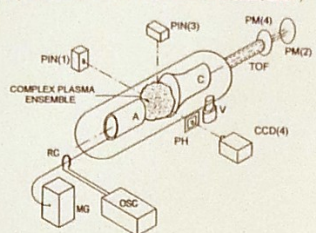
Yu. K. Kurilenkov, V.T.Karpukhin and S.Yu.Guskov¹

Joint Inst. for High Temperatures, Moscow, Russia ; ¹Lebedev Physics Institute, Moscow, Russia

Generation of DD neutrons from microfusion at the interelectrode space of a low energy nanosecond vacuum discharge with deuterium-loaded Pd anode has been demonstrated recently [1]. The principal role of a *virtual cathode* (VC) and the corresponding deep potential well (PW) formed in the interelectrode space are recognised under particle-in-cell (PIC) simulation using a fully electrodynamic code. The calculated depth of the *quasistationary* PW of the VC is about 50-60 kV, and the deuterons being trapped by this well accelerate up to energy of few tens keV that provides DD nuclear synthesis under head-on deuterons collisions (IEC scheme) [1].

Meanwhile, the PIC modeling of particle dynamics and processes in vacuum discharge shows qualitatively, in particular, what is going there during the first 1-2 nsec after voltage applied. During this time the autoelectron beam extracted from the cathode is reaching the deuterium-loaded Pd anode and starts to interact with anode surface. In comparison with the later on processes of virtual cathode and potential well formation, this relatively fast initial stage of discharge in our experiment is still poorly understood. Nevertheless, experiment shows that the beginning of the interaction of the autoelectron beams with deuterium-loaded Pd anode is followed by time-of-flight (TOF) signal from DD 2,45 MeV neutrons rather often.

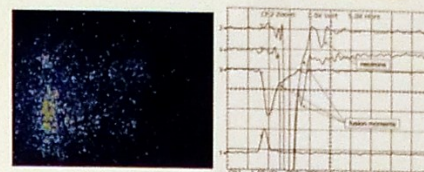
IECF scheme for DD nuclear synthesis based on vacuum discharge (M.Skowronek and Yu.K.Kurilenkov 2003, 2006)



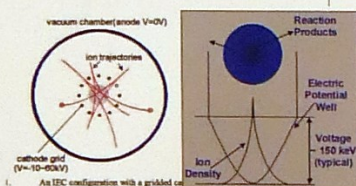
- Parameters of discharge: ≈ 1 J of total energy, $U=70$ kV, $t=50$ nsec, $I_{max}=1$ kA, $TOF=30-90$ cm, $P_{min} \approx 10^{-7}$ mbar.

Observation of DD microfusion accompanied by moderate neutron yield

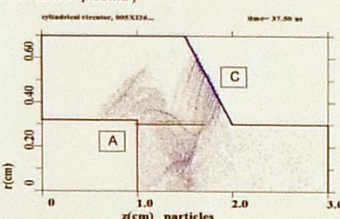
$D(D,n)He^3 \rightarrow 2.45$ MeV neutrons
• neutrons signature - 45, 8 nsec; TOF delayed signal from fusion moment



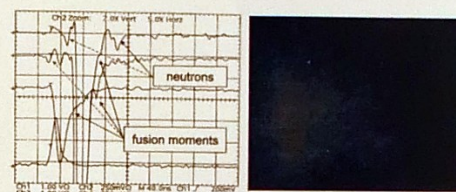
Inertial electrostatic confinement fusion (IECF) general scheme (J.Santarius; K. Yoshikawa)



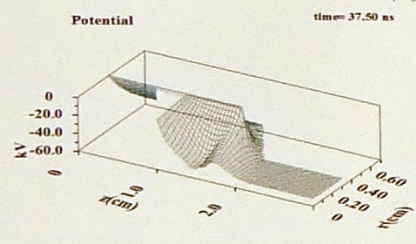
Example of particles dynamics by KARAT code (blue - beam electrons, red - ions accelerated by VC, green - anode plasma)



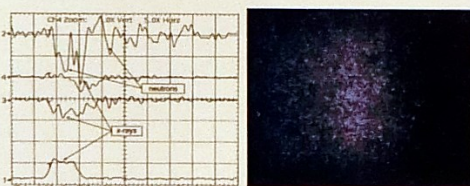
next shot from same experimental series (as above): neutron yield is observed when virtual cathode and potential well are forming along the pulse as well as sometime at very initial stage of discharge also



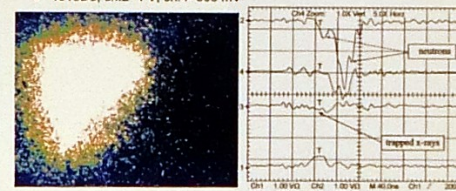
Typical single potential well (PW) at interelectrode space (modeling for real experimental conditions)



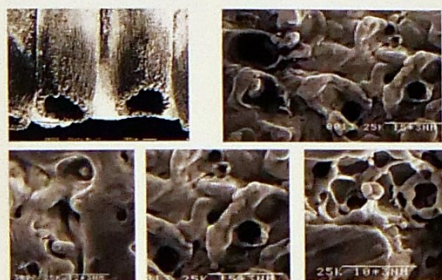
Oscillograms and CCD image of the shot with "coronal" anode (12 Pd deuterium-loaded tubes), where neutrons from initial stage do prevail (0518D7). (Pd anode surface is represented partially on CCD also)



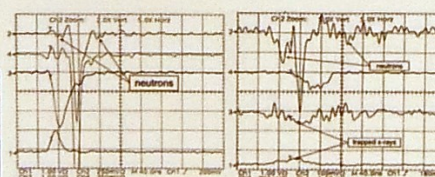
dense interelectrode ensemble with multiple fusion and essential x-rays trapping (« microreactor »)
Fast deuterium ions are trapped ("D" - deuterium cluster" is essential channel of DD fusion)
High pulsating neutron yield and almost no x-rays yield (it provides to register just mainly neutrons at PM4 also)
• 1018D5, ch.2 - 1 V, ch.4 - 500 mV



Pd anode tubes surface morphology



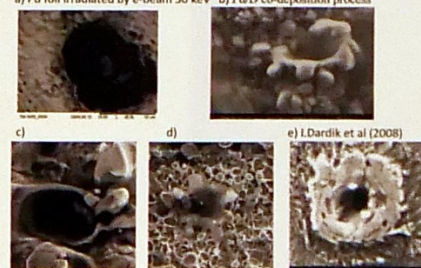
- 1) X-rays dynamics in regime 5, where the piece of paraffin have been located between plasma source and photomultipliers 4 and 2 (left).
- 2) X-rays dynamics in regime 6 for anode with 12 Pd tubes ("coronal" anode) (right)



Examples of craters on Pd surface:

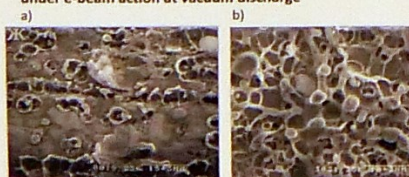
A.Lipson et al 2009(a); S.Szpak et al 2008(b); Yu. Kurilenkov et al (c,d)

a) Pd foil irradiated by e-beam 30 keV b) Pd/D co-deposition process



Examples of Pd surface (Yu. Kurilenkov et al 2011):

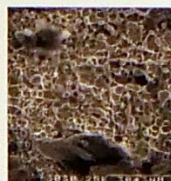
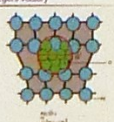
- a) example of craters line track
- b) Pd surface as integrated multichannel microreactor under e-beam action at vacuum discharge



A.G. Lipson, B.J. Heuser, G.H. Miley et al. "Transport and Magnetic Anomalies in Hydrogen-Cycled Pd Foil with a Thermally-Grown Oxide Below 70 K", Phys. Rev. B 72, 082541 (2005)

Metal deuterides upon e-beam irradiation (A.Lipson, J.Chernov et al 2009); Ultra-dense D-cluster target (Miley 2010); Pd anode craters (Kurilenkov 2011)

Edge dislocation core in Pd with H₂ "metallic" hydrogen phase: Dislocation core is a nanotube with radius $R_{nt} \approx b$ (Burgers vector)



We may conclude from the detailed time-of-flight (TOF) analysis of the available experimental data that the initial stage of discharge is also accompanied by a certain neutron yield, which is changing in a more random manner from shot to shot in comparison with the yield from synthesis in the PW at the second stage of the discharge [1]. Qualitatively, similar data on statistically significant emissions of the DD-reaction products, as well as high energy alpha particles have been registered under electron beam stimulation of the D-desorption from Pd/PdO Dx targets [2]. We may assume that micro pores, micro cracks, dislocations (furnished by dense deuterium) and so on, at deuterium-loaded Pd anode represent potential natural array of micro channels for certain number of microfusions near the surface at initial stage of discharge [1]. Neutrons generation at initial stage might be related with lattice-assisted DD synthesis triggered by e-beam irradiation of deuterium-loaded Pd anode surface. The appearing of neutrons at very initial stage of discharge and explosive fulfillment of interelectrode space by nanoclusters might be correlated, if both effect is manifestation of anode ectons (explosive center [3]) of nuclear origin [1].

[1] Yu.K. Kurilenkov et al. *Contrib. Plasma Phys.* 51, No.5 (2011) 427 - 443
[2] I.P. Chernov, A.S. Rusetskii et al. *JETP* 139 (2011) 1088, A.G.Lipson et al. 15th Int. Conf. Condensed Matter Nuclear Physics, Rome, 2009.
[3] G.A. Mesyats. *Cathode Phenomena in a Vacuum Discharge*. Moscow, 2000



Methods for the Investigation of F&P Experiments Electrodes Material Key Features

S. Lecci, E. Castagna, A. Lampasi, M. Sansovini, F. Sarto, A. Torre, V. Violante RdA

ENEA, Technical Unit of Fusion, Lab. of Fusion Nuclear Technologies - Via Enrico Fermi, 45 - 00044 Frascati (Rome) ITALY

ABSTRACT: Material characteristics play a crucial role in Fleischman and Pons type electrochemical experiments [1]. The metallurgy (in particular grain size distribution, grain boundary morphology, crystallographic orientation and material hardness), the surface structure (as roughness, Power Spectral Density Function, surface pattern), and the chemical composition are considered to be, among others, critical features, crucial in determining the electrode properties. An overview of the instruments and techniques used in the investigation of such key features is given, paying attention to their specific potentialities and limitations.

INTRODUCTION: Many years of activity performing Fleischman and Pons calorimetric experiments have shown us that the right material properties are essential to achieve positive results both in terms of good loading of hydrogen and deuterium in the cathodes and excess of power occurrence [2]. The low reproducibility of the latter is now strongly believed to be due to a low reproducibility of many or some of the characteristics of the electrodes material, which are necessary for it to arise [3]. These characteristics are not only difficult to reproduce during the manufacture of the cathodes but even to identify with a good level of accuracy and completeness. A very complex and different set of instruments would be required to perform a complete characterization of the electrodes, nevertheless, with the variety of instrumentation at our disposal, we are able to widely analyze the cathodes, spanning over different levels of characterization, which can go from the metallurgical structure to the electrochemical properties.

CHEMICAL COMPOSITION: The chemical composition of the material is one of the major characteristics to check and can heavily influence other main features and the cathodes electrochemical behavior [4]. It's a parameter which is constantly kept under control during the different stages of the production of the cathodes and even after the experiment. Its analysis can reveal important information which are fundamental for the correct interpretation of the experimental results. For the compositional analysis we can rely on two main instruments, which are an EDS equipped Scanning Electron Microscope (Fig. 1) and a Secondary Ion Mass Spectrometer (Fig. 2). The **Energy Dispersive X-ray Spectrometry** is a powerful analytical technique that allows for fast, non-destructive, elemental analysis, chemical characterization and extensive mapping of a sample. Our system consists of an EVO40 ZEISS Microscope equipped with an Oxford Instruments INCA x-sight EDS Detector with INCA Energy software. This instrument is very easy to use, allows for the analysis of many samples in relatively little time and is simple to maintain. Some weak points are a quite high limit of detection (0.1-0.5%) and a large volume of interaction between the beam and the sample. This instrument is used, mainly, to: check the composition of our cathodes during the production process (Fig. 3) and after the electrolysis; explore the nature of the impurities that can be found on the cathodes surface (Fig. 4), which are believed to heavily condition the cathode behavior; map and highlight inhomogeneous or preferential distribution, for example near the surface (Fig. 5) or at the grain boundaries (Fig. 6).

The **Secondary Ions Mass Spectrometry** is a technique used for the analysis of the composition of surfaces. In our activity, the SIMS is used less often than the EDX, mainly for the analysis of the raw material used to prepare the cathodes, and for the in-depth analysis of the surface deposits. Compared to the EDS, it can reach much lower limits of detection (in the order of the ppm) at the cost of high operating times and partial destruction of the sample.

METALLURGY: There are different characteristics pertinent to the metallurgy, that we believe to be fundamental in order to obtain good cathodes, that we are able to investigate by means of, mainly, a Vickers indenter (Fig. 7) and an EBSD equipped SEM. The hardness of any batch, either commercial or self-made, used in the manufacture of the foils is checked by a Leitz Vickers indenter. Different measures are made, after many stages of the process which lead to the finished cathode, to control the hardness of the material in respect to the metallurgical treatments. **Electron Backscatter Diffraction** analysis is a technique performed to determine the crystallographic orientation, the grain size distribution

and many other important features of the materials (Fig. 8). Each electrode manufactured must be checked to see if it fits the desired conditions of these parameters and eventually correlate the occurrence of excess heat with the crystallographic structure [5]. Our instrumentation consists of an Oxford Instruments Nordlys II EBSD Detector with HKL CHANNEL 5 Acquisition and Data Processing software, capable of a spatial resolution down to 10x nm. This kind of analysis can be very time consuming, especially if performed on a high number of samples, moreover, the surface of the analyzed material needs to be very smooth.

SURFACE: The surface of the palladium cathode is thought to be a major feature for the occurrence of the excess of power, so, the control of the surface is a critical issue [6]. Being the result of the whole range of processes that the material underwent, the surface can differ greatly between different samples (Fig. 9). The **SEM** is a powerful instrument for the analysis of the surface, as it is relatively easy and inexpensive to use, allows for the observation of many samples at a time at a wide range of resolutions and does not need a complex sample preparation. Our instrument is a ZEISS EVO-40 with Zeiss SmartSEM software suite, which is able of a max resolution of 3nm @ 30kV, an acceleration Voltage of 0.2 to 30kV, a range of magnification from 7 to 1,000,000x and is equipped with a 4 sectors detector for backscattered electrons. Unfortunately, these are ideal performances, difficult to obtain in the operating environment, and for an observation at high magnification a FESEM would have been, sometimes, of extreme usefulness. Another useful instrument that we use systematically for the analysis of the cathode surface is the **Atomic Force Microscope**. Our instrument is an Asping Perception Device (Fig. 10), with a scanner having a maximum scan area of 40x40 microns and a z-axis range of 5 microns, the tip is a Veeco MLCT-AUNM-10 one, with height range from 2.5 microns to 3.5 microns and 20 microns of nominal radius. The AFM is usually operated with a scan area of 30x30 microns and a resolution of 512x512 points, which results in a sampling period of about 58 nm. AFM gives a direct measurement of the tri-dimensional (3-D) surface height profile, which was used to calculate the Power Spectral Density (Fig. 11). That parameter is believed to be indicative of the probability of the occurrence of the excess heat [7-8], so it is an important one to monitor. The main weakness of this instrument is that the portion of the surface analyzed is very small, so there is need for a very large number of analysis on the same electrode to well represent the variety of the surface.

ELECTROCHEMICAL CHARACTERISTICS: Recent work [9] is aiming at investigating the cathodes by means of electrochemical techniques such as **Electrochemical Impedance Spectroscopy** (Fig. 12) and **Cyclic Voltammetry** (Fig. 13). Differences in the electrochemical behavior of the cathodes reflect differences in the material composition or structure that can be highlighted with such sophisticated techniques. The instrumentation used consists of two Bio-Logic Portable Potentiostat/Galvanostat, an SP-200 and an SP-240 (Fig. 14), controlled by EC-Lab Software. The scope of this work is to try to identify new properties, yet unknown, that will allow to discriminate active from inactive materials.

CONCLUSIONS: The range of analyses that we are able to perform for the investigation of F&P experiments electrodes material key features allows us to extensively characterize the cathodes used. Different properties of the electrodes can be determined, as the chemical composition, the crystal orientation, the grain distribution, the material hardness, the structure of the surface and its roughness, the presence and the nature of surface contaminants and some electrochemical properties. Even though the instrumentation used is appropriate, much could be done to increase the range of analyses and their quality. Several characteristics, fundamental for the occurrence of the F&P effect, could still be out of our reach, their identification requiring extremely performing (or, perhaps, yet unavailable) instrumentation.

REFERENCES:

Fig. 1 - Picture of the S.E.M.

Fig. 2 - Picture of the SIMS.

Fig. 3 - EDS spectrum and quantitative analysis results table on a prepared material ideally 90%Pd, 10%Ru, 5% Fe and 5% Cu.

Fig. 4 - analysis of impurities on a cathode surface (Al in red, Zr in green and Pd in blue).

Fig. 5 - EDS spectra at different energies could highlight a higher concentration of some elements near the surface.

Fig. 6 - EDS mapping showing segregation of oxides near the grain boundaries of a palladium cathode.

Fig. 7 - Vickers indenter used for the material hardness test.

Fig. 8 - Orientation maps, Grain Size distributions and Pole figures of different materials used in the manufacture of the cathodes.

Fig. 9 - Four pictures, at the same magnification, that shows the variety of morphologies that different samples surfaces can have.

Fig. 10 - Picture of the A.F.M.

Fig. 11 - AFM images of different cathodes and relative PSD.

Fig. 12 - Different EIS from two different cathodes.

Fig. 13 - CV from a Pd cathode.

Fig. 14 - Picture of the Bio-Logic SP-240.



Synthesis and characterization of Pd-Ni-ZrO₂ composite materials for LENR investigations

E. Marano, A. Castellero, M. Baricco

Università degli Studi di Torino and NIS Excellence Centre



ICC-F-19
International Conference on
Condensed Matter Nuclear Science

Aim of the work

1. Synthesis and characterization of Pd-Ni nanoparticles embedded in ZrO₂ matrix for investigations on LENR effects in hydrogen isotopes atmosphere, as first proposed by Y. Arata et al.¹ and Kimura et al.²
2. Optimization of amorphization and oxidation processes.
3. Effect of nickel addition on glass formation and oxidation kinetics.

Starting elements purity:

Pd: 99.9% (met. basis)
Ni: 99.97% (met. basis)
Zr: 99.8% (met. basis)

Materials and Methods

The composite material was prepared following the *procedure* described in ², consisting in the following steps:

- 1) Melting pure elements in arc furnace.
- 2) Amorphous ribbon formation by planar flow casting at 42 m/s.
- 3) Oxidation for 24 h at 330°C in air in a muffle oven.

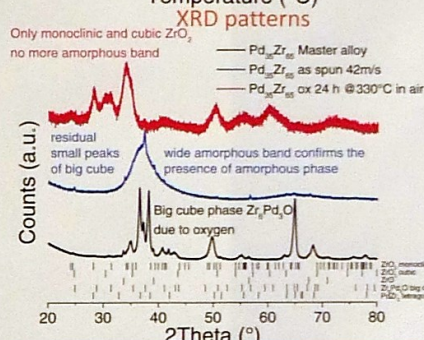
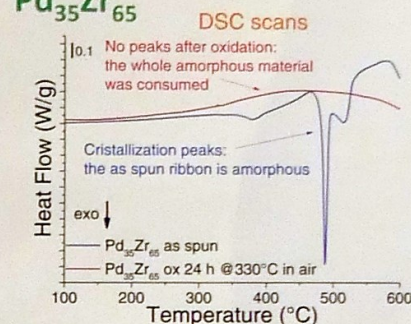
Characterization techniques:

- Differential Scanning Calorimetry (DSC) in Ar flow with 20°C/min scan rate up to 600°C.
- X-Ray powder Diffraction (XRD) with Cu anode.

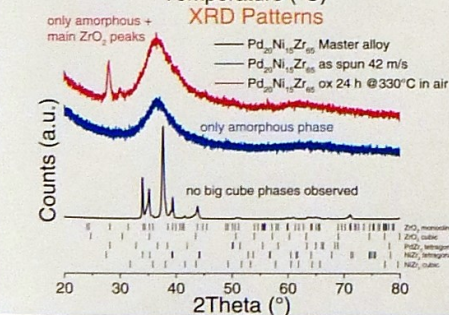
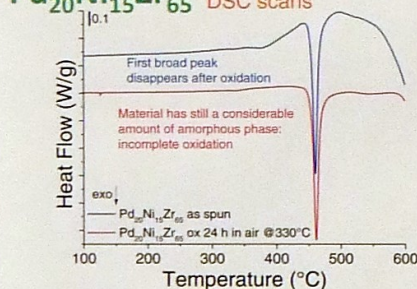
Nominal compositions

Pd ₃₅ Zr ₆₅
Pd ₂₀ Ni ₁₅ Zr ₆₅
Pd ₁₅ Ni ₂₀ Zr ₆₅
Pd ₅ Ni ₃₀ Zr ₆₅
Ni ₃₅ Zr ₆₅

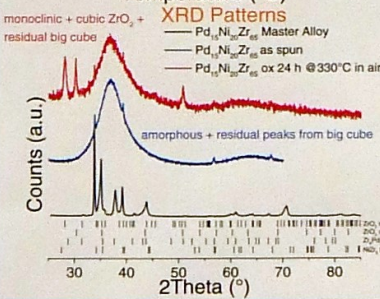
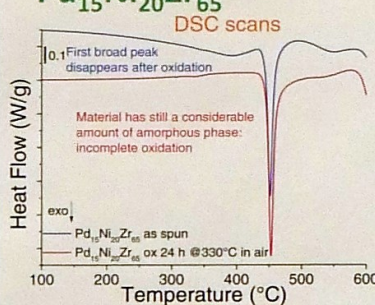
Pd₃₅Zr₆₅



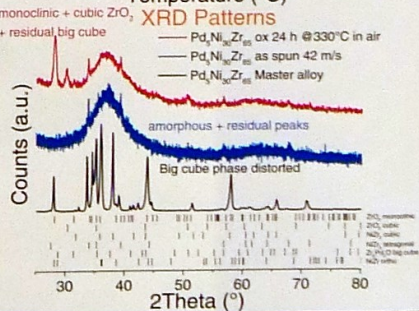
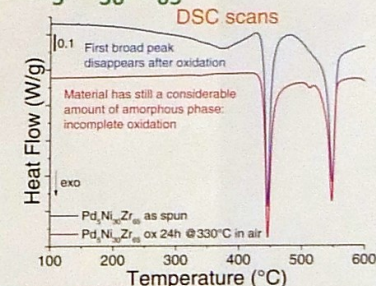
Pd₂₀Ni₁₅Zr₆₅



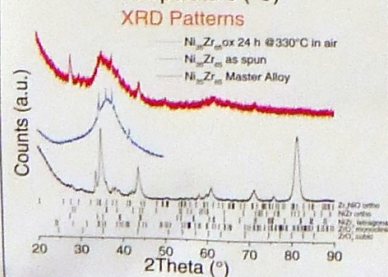
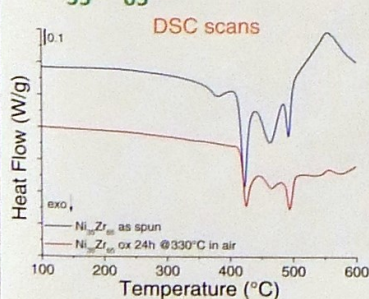
Pd₁₅Ni₂₀Zr₆₅



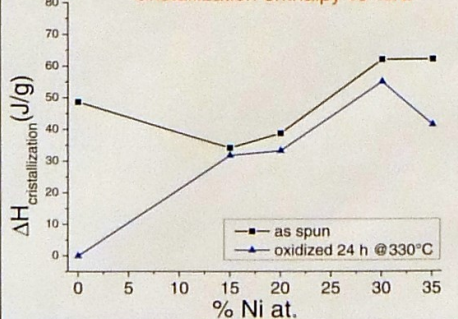
Pd₅Ni₃₀Zr₆₅



Ni₃₅Zr₆₅



Cristallization enthalpy vs %Ni



Future works

- Microstructural characterization of oxidized samples by TEM observations (size and distribution of metallic nanoparticles in the oxide matrix).
- Study of the interaction between oxidized samples and hydrogen isotopes by DSC and calorimetry measurements.

Conclusions

- Big cube Zr₂Ni-type phase formation because of oxygen contamination in the master alloys.
- Amorphization for all compositions, with a small fraction of residual big cube phase.
- The presence of nickel considerably slows down the oxidation reaction, leaving a significant amount of amorphous phase together with oxide phases.
- Only amorphous Pd₃₅Zr₆₅ oxidizes completely at 330°C, suggesting the formation of the composite material (Pd nanoparticles embedded in ZrO₂ matrix).

¹ Y. Arata, Y. C. Zhang, Establishment of the "Solid Fusion" Reactor, ICCF-14, Washington, DC, 2008

² H. A. Kimura, A. Inoue, T. Masumoto, The oxidation of amorphous Zr-base binary alloys in air, Corrosion Science **35**(5), 1993, pp909-915.

Nature of the deep-Dirac levels

*A. Meulenber¹, J.L. Paillet²

¹ Science for Humanity Trust, Inc., USA, mules333@gmail.com
² Aix-Marseille University, France jean-luc.paillet@club-internet.fr

Abstract

Maly and Va'vra (M&V) in 1993 [1] and 1995 [2] presented a computational evaluation of the Dirac equations that included the 'anomalous' solution. The regular solutions of these equations are the basis for modern quantum mechanical predictions for comparison with the experimental values of atomic-electron orbital energies. The other solution, discussed in the literature for over 55 years, is relativistic and considered anomalous because its predicted levels are very deep (up to 511 keV) and have never been observed. Nevertheless, the existence of these deep levels provides a ready explanation of the mechanism for penetration of the Coulomb barrier and the means of D-D fusion below the He fragmentation levels. Since these levels also provide the basis for all of the other cold fusion observations (both PdD and NiH systems), it is important that arguments for and against the Dirac model be examined. The theoretical support for this anomalous solution is provided in a companion paper in this conference [3].

This presentation seeks to update the deep-orbit information provided in a poster at ICCF-17 [4], to describe the nature of these deep-Dirac levels (DDLs) [5], to report on additional, but unpublished, results presented by Va'vra in 1998 [6], and to correct some interpretations of the model that Va'vra has provided in 2013 [7]. There are some unusual properties of the DDLs relative to those of the known atomic orbitals.

Interpretation of the DDL properties, based on the non-relativistic solutions, leads to misunderstandings and further rejection of the concept of the deep levels. We hope to clarify this situation and indicate the importance of the calculations for cold fusion models. Cold fusion results provide a basis for understanding the DDLs and the proposed new fields of femto-physics and femto-chemistry.

Excerpts from four Maly and Va'vra papers on deep Dirac levels:

Published in Fusion Technology, Vol. 24, November 1993

ELECTRON TRANSITIONS ON DEEP DIRAC LEVELS I

J. A. Maly, J. Va'vra

ABSTRACT

The original solutions of the Schrodinger relativistic equation and the Dirac equations for hydrogen-like atoms were analyzed for the possible existence of some other electron levels, which were not originally derived. It was found that besides the known atomic levels, each atom should also have the Deep Dirac Levels (DDL). The electron transition on such DDL would produce large amounts of atomic energy (400 - 510 keV per transition depending on the Z of the atom). ...

4. CALCULATIONS OF NEW ENERGY LEVELS

A computer program was written which calculates atomic energy levels for Relativistic Schrodinger levels E1S(-), E2S(-) in table 1a, Dirac levels ED1(-) and ED2(-) in table 2a, and the non-relativistic Schrodinger levels E(N, Z) given by a simple Bohr formula.

Table 1a. Relativistic Schrodinger Levels for H (Z=1) in eV.

E(N, Z)	N	M	E1S	E2S
1s	1	0	-13.6056582	-507.271 937 800
2s	2	0	-3.401 457	-13.605 652
2p	2	1	-3.401 457	-13.603 699
3s	3	0	-1.511 759	-1.511 747
3p	3	1	-1.511 759	-1.511 746
3d	3	2	-1.511 759	-1.511 746
4s	4	0	-0.850 354	-0.850 356
4p	4	1	-0.850 354	-0.850 356
4d	4	2	-0.850 354	-0.850 356
5s	5	0	-0.544 228	-0.544 228
5p	5	1	-0.544 228	-0.544 228
5d	5	2	-0.544 228	-0.544 228
6s	6	0	-0.377 936	-0.377 936
6p	6	1	-0.377 936	-0.377 936
6d	6	2	-0.377 936	-0.377 936
7s	7	0	-0.279 942	-0.279 942
7p	7	1	-0.279 942	-0.279 942
7d	7	2	-0.279 942	-0.279 942

* Negative energy states, not observable.

Table 1b. Dirac Levels of Hydrogen-Like Atoms for H (Z=1) in eV.

E(N, Z)	N	M	K	L1	L2	E2D
1s	1	0	1	0	0	-13.605873
2s	2	0	2	1	0	-3.401434
2p	2	1	1	0	0	-3.401479
3s	3	0	3	2	1	-1.511746
3p	3	1	2	1	0	-1.511750
3d	3	2	1	0	0	-1.511764
4s	4	0	4	3	2	-0.850356
4p	4	1	3	2	1	-0.850357
4d	4	2	2	1	0	-0.850359
5s	5	0	5	4	3	-0.544228
5p	5	1	4	3	2	-0.544228
5d	5	2	3	2	1	-0.544228
6s	6	0	6	5	4	-0.377936
6p	6	1	5	4	3	-0.377936
6d	6	2	4	3	2	-0.377936
7s	7	0	7	6	5	-0.279942
7p	7	1	6	5	4	-0.279942
7d	7	2	5	4	3	-0.279942

Published in Fusion Technology, Vol. 27, Jan. 1995

ELECTRON TRANSITIONS ON DEEP DIRAC LEVELS II

J. A. Maly, J. Va'vra

ABSTRACT

... In this paper we give an estimate of the size of the DDL atoms and we propose a physics explanation how to excite the DDL transitions.

The main point of this chapter is that the size of atoms with all electrons on the DDL levels can be very small. Under certain conditions (1×10^9), such atoms with all electrons on the DDL levels might participate in the secondary nuclear reactions.

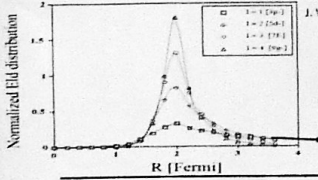
4. NUCLEAR AND CHEMICAL BEHAVIOR OF THE DDL ATOMS

The 'collapsed' atoms of H and He with all their electrons on the DDL could behave almost as neutral particles with a substantially reduced Coulomb barrier, and they could participate at some level in the nuclear reactions.

November 25, 1998, Siegen University, Germany

ON A POSSIBILITY OF EXISTENCE OF NEW ATOMIC LEVELS, WHICH WERE NEGLECTED THEORETICALLY AND NOT MEASURED EXPERIMENTALLY

J. Va'vra



note: The different orbitals all peak at the same distance from the nucleus. However, the lower magnitude binding energies (e.g., 3p) have extended 'tails' that reduce their average depth in the potential well.

A NEW WAY TO EXPLAIN THE 511 KEV SIGNAL FROM THE CENTER OF THE GALAXY AND SOME DARK MATTER EXPERIMENTS

J. Va'vra

Astronomy & Astrophysics, June 11, 2013

ABSTRACT

... In this paper, we propose an alternative explanation: the observed signal is due to atomic transitions to 'small hydrogen atom,' where electron is captured by proton on a small tight orbit around proton. ...

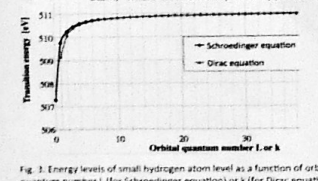


Fig. 3. Energy levels of small hydrogen atom level as a function of orbital quantum number L (for Schrodinger equation) or h (for Dirac equation).

To estimate electron energy on hydrogen DDL levels approximately, we will use a simplification of calculating the Bohr radius (see Fig. 5) from energy levels, which then allows an easy estimate of electron equivalent orbit energy (see Fig. 6) using the de Broglie formula. This is naive, but it leads to interesting predictions.

Note: Va'vra properly plots results of the anomalous Dirac solution in Fig. 3, which provides the transition energy (binding energy) of an electron to the various DDL states. However, he then assumes that the Heisenberg Uncertainty Principle (HUP) and deBroglie formula applies to these results and extends them (Figs. 5 & 6) to the electron kinetic energies and orbital radii.

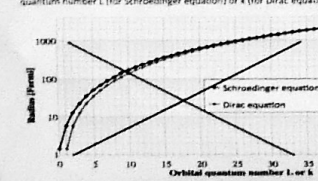


Fig. 5. Bohr radius as a function of orbital quantum number.

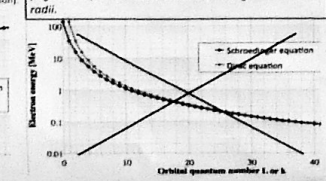


Fig. 6. Electron orbit energy as a function of orbital quantum number.

These predicted results follow the pattern of atomic orbitals, but are inconsistent with calculated results for DDLs.

Atomic orbitals vs the relativistic Schrodinger electron deep levels (EDLs) and the deep Dirac levels (DDLs)

Atomic electron orbitals are very well known and understood. Until Maly and Va'vra (M&V) did so in the early 1990's, the multiplicity of relativistic-electron deep levels (EDLs) had not been explored in the literature. The basic premise of any deep levels has been improperly challenged for over 45 years (see companion poster [3]), therefore no one has 'bothered' to publish predictions beyond the 'ground-state' of these deep orbitals.

With the advent of powerful computers, the task of solving the relevant equations became much easier and M&V (see left-side panel) did so in the context of cold fusion (CF). What are the properties of the EDLs and why are they important to CF? First, why do we refer to the electron deep levels as deep Dirac levels when they are also predicted by the Klein Gordon (K-G) equation that is equivalent to the relativistic Schrodinger equation? It is in response to early arguments against the K-G prediction of deep-orbits. The fact that it was valid for spinless particles was interpreted to mean that it was not valid for spin 1/2 particles. These arguments ignored the fact that the Schrodinger equation (also valid only for spinless particles) had been used for decades to describe electron orbitals. M&V buried this argument by showing that the relativistic Schrodinger and the Dirac equations also predicted the deep levels. Furthermore, the effect of spin on the hydrogen atom calculation for the deep levels had an effect of only 2 keV out of over 500 keV. Thus:

Relativity introduces new electron states with binding-energies at ~500 keV. Spin affects these levels by only ~2 keV.

What are some similarities between atomic orbitals and EDLs?

- Both sets of orbits are solutions of the same equations – they have identical starting assumptions and potentials.
 - The solutions are a sequence that:
 - in the atomic case, depends on the electron orbital radius, energy, and angular momentum, along with the electron momentum, mass, and velocity (i.e., the deBroglie wavelength, $\lambda_e = h/mv$).
 - in the EDL case, also depends on relativity (in some to-be-determined manner?)
 - could involve relativity in both atomic and EDL orbits. It is just not noticeable in the low-energy atomic orbits.
- The sequences are related to the cyclical nature of something related to waves periodically returning to identical conditions.
 - This depends on the conservation laws of energy and momentum (linear and angular).
 - Mathematically, closed integration about a path gives a zero result. Thus, no change occurs and a stable point is set. Closure depends on conditions being identical in all 'dimensions'.
 - In an orbit, the angular momentum vector could remain 'fixed' if so, it would not be a source of the periodicity. However, if torque were applied, the vector would precess and periodic motion would be introduced.
 - It is assumed that the deBroglie wavelength is also based on some form of precession. Spin would be a logical assumption, but, the Schrodinger equations predict the discrete deep levels without resorting to spin.
 - Does the dependence on the deBroglie wavelength provide an equivalent to precession of a spin vector?
- A consistent model results if precession from different torques are considered for electrons in linear and orbital motion.
 - Relativity & deBroglie wavelengths
 - Relativity & angular velocity
- Relativistic effects, strong enough to increase electron mass, would be the cause of the deep orbits.

What are some differences between atomic orbitals and EDLs?

Comparison is based mainly on the Maly and Va'vra results from the tables on the left.

- The obvious differences are expressed in the level energy vs average electron-orbital radius.
- The EDL orbits are close enough to the nucleus that the Coulomb potential at the atomic-orbital levels is no longer a valid assumption. The virial theorem, predicting $KE = PE/2$ for a $1/r$ potential, is no longer generally valid. Nevertheless, for near-circular orbits, an electron only sees the $1/r$ potential, not the repulsive central core.
- The angular momentum of atomic-electron orbitals is sufficient to produce and receive photons as the energy-exchange medium. This is not the case for the EDLs where the angular momentum is on the order of $h/100$. This is where Va'vra's EDL story goes wrong. It is not the solutions of the Schrodinger or Dirac equations that are in error; it is in their being misinterpreted (see his paragraph below Fig. 3) and then the extrapolation of this error (Figs. 5 & 6).
- The relativistic models predict many new and different energy levels:
 - Negative-energy levels (for positrons and anti-protons)
 - Electron deep levels that are not matched by positron deep levels.
 - This is a symmetry-breaking effect.
- The relativistic mass increase, as an EDL electron gets closer to the nucleus and as its velocity approaches that of the speed of light, means that the higher-n EDL orbits are, on average, closer to the nucleus. This is unlike Va'vra's incorrect prediction in Fig. 6 based on the Heisenberg uncertainty principle. The basis of the quantized EDLs is still to be determined.
- Relativistic effects break the degeneracy in many of the atomic-electron levels.
- The kinetic energy and mass increases of relativistic electrons nearer to the nucleus are consistent with decreasing radii of more-nearly circular DDL orbits.
 - Classical relativistic deep-electron orbits exist. These orbits are not quantized.
 - The low-angular momentum orbitals of high-n DDL levels cannot exist, because they cannot cross the repulsive barrier.
 - The high-angular momentum orbitals of high-n levels may not exist, because they do not 'touch' the repulsive barrier?
- The selection rules differ for the EDLs and DDLs and the atomic-electron orbitals:
 - The atomic-electron levels exist for all positive integer n values.
 - The relativistic deep levels exist only for alternating integer n values. The relativistic Schrodinger levels exist only for odd integers. The relativistic Dirac levels exist only for even integers.
 - The alternation of levels is a relativistic effect.
 - The odd/even selection rules result from the spin effect.
- The multiple levels predicted for the deep orbits are similar to those for the atomic orbits in some respects, not in others.
 - They exist. There is not just a single level.
 - There is an integer change in the solutions of the wave equations between both deep and atomic orbitals.
 - The binding energy increases with ang. mom. for deep orbits (decreasing with higher ang. mom. in atomic orbitals).
 - The difference between atomic levels is associated with h (i.e., the deBroglie wavelength).
 - The difference in deep levels cannot be associated with h .
 - The source of periodicity in the deep levels must be related to something beyond the deBroglie wavelength. There is insufficient angular momentum for electrons at these levels for any integer change.
 - There must be another (as yet unproven) source of periodicity from relativistic effects

Comparisons between, and questions about, electron deep levels (EDLs) predicted by the relativistic Schrodinger equation and the deep Dirac levels (DDLs)?

- Neither EDLs nor DDLs are symmetric between the electrons and positrons.
- There are the same number of positron states and electron states in the Schrodinger results.
- There are more positron states than electron states in the Dirac results. Is this a result of spin? If so, why?
- Relativity has broken symmetry in both cases. Is this a valid conclusion or an artifact of the calculation? Would these same results appear if the calculation were instead carried out for positrons and anti-protons?
- Spin has a large effect on the deep levels. (Nevertheless, it is small relative to the relativistic effect.)
- Spin introduces a new quantum number and, in the deep region, a reordering of the old numbers.
- The new quantum number is related to spin and, while also related to relativity, it exists only in the spin 1/2 development of the Dirac equations. Therefore, its separate identity does not depend on relativity.
- The deep orbits are related to relativity.
- If the deep orbits are separated by alternating integers, what do the integers represent?

Conclusions

Relativity has brought a solution to the central-body problem out of the center of the potential into a series of deep levels available to electrons.

- Heavier particle orbits are predicted within the nucleus.
- The Coulomb potential is modified in the near-field by the angular momentum barrier, which is modified by the increasing relativistic mass with increasing kinetic energy.

The deep orbits are 'quantized' with respect to an unknown source, apparently not related to the deBroglie wavelength or to the Planck constant.

Increased angular momentum, circularizes the deep-electron orbit and allows it to move closer to the proton.

References

- J. A. Maly, J. Va'vra, "Electron Transitions on Deep Dirac Levels," Fusion Technology, vol. 24, p. 307, 1993
- J. A. Maly and J. Va'vra, "Electron Transitions on Deep Dirac Levels II," Fusion Technology, vol. 27, January pp. 59-70, 1995
- J. L. Paillet, A. Meulenber, "Basis for electron deep orbits of the hydrogen atom," poster in this conference
- A. Meulenber and K. P. Sinha, "Deep-electron orbits in Cold Fusion," 17th International Conference on Condensed Matter Nuclear Science, Daejeon, Korea, 12-17 February 2012, J. Condensed Matter Nuclear Sci. 13 (2014), 368-377
- A. Meulenber, "Deep-orbit electron radiation absorption and emission," ICCF-18, 18th Int. Conf. on Cond. Matter Nuclear Science, Columbia, Missouri, 25/07/2013, <http://hdl.handle.net/10355/36501>
- J. Va'vra, "On a possibility of existence of new atomic levels, which were neglected theoretically and not measured experimentally," presented at Siegen University, Germany, November 25, 1998
- J. Va'vra, "A new way to explain the 511 keV signal from the center of the Galaxy and some dark matter experiments," Astronomy & Astrophysics <http://arxiv.org/abs/1304.0833>

Thermodynamic and Kinetic Factors Concerning The D+D Fusion Reaction for the Pd/D System

Melvin H. Miles and Iraj Parchamzad
Department of Chemistry, University of LaVerne
LaVerne, CA USA 91750
(mmiles@laverne.edu)

ICCF - 19

Padua, Italy

13-17 April 2015

Thermodynamic Definitions

$$H = U + PV$$

$$G = U + PV - TS = H - TS$$

At Constant T: $\Delta G = \Delta H - T\Delta S$

At Constant P with only P-V work

$$\Delta H = \Delta U + P\Delta V = (q - P\Delta V) + P\Delta V = q$$

For Spontaneous (Possible) Reaction

$$(\Delta G)_{T,P} < 0$$

$$(\Delta H)_{T,P} < 0 \text{ (less useful)}$$

Kinetics for D+D → He-4 Eyring Rate Theory

$$\text{Rate} = d(\text{He-4})/dt = -1/2 d(\text{D})/dt = k[\text{D}]^2 \text{ where } n=0, 1, 2, \dots$$

Assume zero-order Reaction (n=0)

$$\text{Rate} = d(\text{He-4})/dt = k$$

For $P_A = 100 \text{ mW}$, $T = 300 \text{ K}$, Pd electrode $0.2 \text{ cm} \times 2 \text{ cm}$
 $k = 2.6174 \times 10^{12} \text{ He-4/s}$

Eyring Rate Theory

$$k = (k_B T/h) e^{-\Delta G^\ddagger/RT} = A e^{-\Delta G^\ddagger/RT}$$

$$\Delta G^\ddagger = -RT \ln(kh/k_B T) = 13,700 \text{ Jmol}^{-1}$$

$$E_a = \Delta G^\ddagger + T\Delta S^\ddagger + RT = 16,152 \text{ Jmol}^{-1}$$

Using $1 \text{ eV} = 96485 \text{ Jmol}^{-1}$

$$E_a = 0.167 \text{ eV} \quad \text{Eyring Theory}$$

Activation Energy (Diffusion of Deuterons in Palladium)

$$E_a = 0.206 \text{ eV} \quad \text{for } T = 218 - 333 \text{ K}$$

(V. Fukai, "The Metal-Hydrogen System: Basic Bulk Properties"
Springer-Verlag, Berlin, 1992, pp. 229-231)

Assumptions for Excess Power at 300K for Pd Electrode (0.2x2.0 cm)

$P_A \text{ (mW)}$	$E_a \text{ (eV)}$
22.5	0.206
50.0	0.185
100.0	0.168
200.0	0.145

$$V(\text{Pd}) = 0.063 \text{ cm}^3 \quad (P_A = 63 \text{ mW})$$

Eyring Rate Theory Comments

Applications

"...the theory of absolute reaction rates is not merely a theory of the kinetics of chemical reactions; it is one that can, in principle, be applied to any process involving a rearrangement of matter, that is to say, any rate process." (p. vii, preface).

Entropy of Activation, ΔS^\ddagger

"...in many reactions the activated state will resemble very closely the final state." (p. 24).

"...a negative value of ΔS^\ddagger implies a small probability of the formation of the activated state." (p. 24).

S. Glasstone, K.J. Laidler and H. Eyring, "The Theory of Rate Processes", McGraw-Hill, N.Y. 1941

Importance of Symmetry (High Deuteron Concentrations)

Palladium Rods

Line of High D^+ Concentration for Concentric Symmetry



Palladium Cube

Point of High D^+ Concentration



"...use a flat sheet or small diameter palladium rod cathode. These shapes avoided the corner part of a cubic structure (the bulk), which tended to heat faster than the surface."
C.G. Beaudette, "Excess Heat-Why Cold Fusion Research Prevailed", 2nd Edition, 2002, pp. 36-37.

Irregular Palladium Shapes → Low Deuteron Concentrations

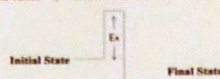
Thermodynamic and Kinetics

Thermodynamics

- Initial State → Final State
 $\text{D} + \text{D} \rightarrow \text{He-4}$
- No Information On Rate of Reaction
- Changes In Thermodynamic Properties
 ΔU (Internal Energy) ΔS (Entropy)
 ΔH (Enthalpy) ΔG (Gibbs Energy)

Kinetics

- Reaction Rates
- Reaction Order
- Activation Energy (E_a)



Thermodynamics For $\text{D} + \text{D} \rightarrow \text{He-4}$ (at $T = 298.15 \text{ K}$ and $P = 10^5 \text{ Pa}$)

$$\Delta H = \Delta_r H^\circ = -23.846478 \times 10^{12} \text{ Jmol}^{-1}$$

$$(\Delta E = \Delta mc^2 = \Delta_r H^\circ)$$

$$\Delta S = S^\circ(\text{He-4}) - 2 S^\circ(\text{D}) = -120.548 \text{ Jmol}^{-1}\text{K}^{-1}$$

$$\Delta G = \Delta H - T\Delta S = \Delta H = -23.8084 \times 10^{12} \text{ Jmol}^{-1}$$

- D+D Fusion To Form He-4 Is Thermodynamically Possible At Room Temperatures
- Thermodynamic Provides No Information On Reaction Rate or Coulombic Barrier
- Favorable Thermodynamics Allows Possibility of Catalysis or New Reaction Pathways To Increase Reaction Rate
- Large and Negative Entropy Change

Table of Thermodynamic Values at 298.15 K and 10^5 Pa

	298.15 K	10^5 Pa
$\Delta H \text{ (Jmol}^{-1}\text{)}$	-2.30084×10^{12}	-2.30292×10^{12}
$\Delta S \text{ (Jmol}^{-1}\text{K}^{-1}\text{)}$	-120.548	-385.010
$\Delta G \text{ (Jmol}^{-1}\text{)}$	-2.30084×10^{12}	-2.26442×10^{12}

Experimental Measurement of Diffusion of Deuterium In Palladium

Experimental $E_a = 0.206 \text{ eV}$ (Fukai, pp. 229-231)
Eyring Rate Theory $E_a = 0.168$

- Suggests that the D+D fusion reaction in palladium may be controlled by the diffusion of D atoms (or D^+ ions) into some fusion reaction zone.
- Supports Assumption of Zero-Order Reaction.
- Conditions for Zero-Order Reactions --
"Only a small fraction of the reactant molecules are in a location or state in which they are able to react. This fraction is continually replenished from the larger pool."
"Zero-Order reactions are typically found when a material that is required for the reaction to proceed, such as a surface or a catalyst, is saturated by the reactants".
- Possibly Pseudo-Zero Order Reaction
Rate = $k[\text{D}] = k'$ where D remains relatively constant.

Possible Fusion Reaction Zones (Electrochemical Double Layers)

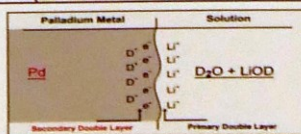


Figure 1. Schematic representation of double layers as possible reaction zones for D+D fusion involving the palladium electrode.

Regions of High D^+ and e^- concentrations.

- Explains Incubation Period (Surface Blocking by Silicates).
- Explains Need for High D Loadings (for Secondary Double Layer).
- Explains Need for Large Current Densities (Intensifies Double Layer Structure)
- Explains Flux (Reaction Requires Movement of D^+ Across Reaction Zone).

SUMMARY

- Based on Thermodynamics, D+D Fusion to Form Helium-4 Is Possible at Room Temperatures.
- Eyring Rate Theory Supports an Activation Energy Consistent with Deuterium Diffusion in Palladium.
- Eyring Rate Theory Consistent with a Zero-Order Reaction.
- Special Reaction Zones are Required for Fusion.
- Reaction Zones Involve only Very Small Fractions of the D/Pd Atoms.
- Typical Half-Life ($t_{1/2}$) Is More Than 1000 years.

Review of Thermodynamic Laws

Basic State Functions (U, S, P, V, T)

First Law $\Delta U = q + w$

Second Law $\Delta S \geq dq/T$

Third Law $S \rightarrow 0 \text{ as } T \rightarrow 0$

First Law "You can't win. You can only break even"

Second Law "You can break even only at Absolute Zero ($T = 0 \text{ K}$)"
($EH = w/q = 1 - T_f/T_i$)

Third Law "You can never reach Absolute Zero"

Thermodynamics For $\text{D} + \text{D} \rightarrow \text{He-4}$ (at $T = 10^6 \text{ K}$)

Heat Capacities For Monatomic Gases; $C_p = 5R/2 = 20.686 \text{ Jmol}^{-1}\text{K}^{-1}$

$$\Delta C_p = S(\text{He-4}) - 2 S(\text{D}) = -20.786 \text{ Jmol}^{-1}\text{K}^{-1}$$

Kirchhoff's Law For Enthalpy

$$\Delta H(T_2) = \Delta H(T_1) + \Delta C_p(T_2 - T_1) = -2.30292 \times 10^{12} \text{ Jmol}^{-1} \quad (T = 10^6 \text{ K})$$

Effect of Temperature on Entropy

$$\Delta S(T_2) = \Delta S(T_1) + \Delta C_p \ln(T_2/T_1) = -385.010 \text{ Jmol}^{-1}\text{K}^{-1} \quad (T = 10^6 \text{ K})$$

Effect of Temperature on Gibbs Energy

$$\Delta G(T_2) = \Delta H(T_2) - T_2 \Delta S(T_2) = -2.26442 \times 10^{12} \text{ Jmol}^{-1}$$

Change In Mass

(CODATA, NIST, November 2012)

Nuclear Reactions

$$\Delta G = \Delta H - T\Delta S = \Delta H - q = \Delta mc^2 \quad (\Delta H \gg T\Delta S)$$

Example $\text{D} + \text{D} \rightarrow \text{He-4}$

$$\text{D} \quad (1875.612889 \text{ MeV}) \quad \text{He-4} \quad 3727.379240 \text{ MeV}$$

$$\Delta G = q = -23.846478 \text{ MeV} \quad (\text{Possible})$$

Example $p^+ + e^- \rightarrow n$

$$p^+ \quad (938.272086 \text{ MeV}) \quad n \quad (939.565379 \text{ MeV})$$

$$e^- \quad (0.51099 \text{ MeV})$$

$$\Delta G = q = +0.782334 \text{ MeV}$$

(Not possible without this added energy)

Half-Life of Typical D+D Fusion Reaction in the Pd/D System

$A + B \rightarrow \text{Products}$

$$\text{Rate} = -dA/dt = k \quad (\text{Zero-order})$$

$$dA = -k dt$$

$$A = A_0 - kt$$

$$t_{1/2} = A_0/2k$$

$$\text{Pd} \quad (0.2 \text{ cm} \times 2.0 \text{ cm}) \rightarrow [\text{D}]_0 = 3.86 \times 10^{22} \text{ atoms (for D/Pd} = 0.9)$$

$$k = 2.6174 \times 10^{12} \text{ atoms/s for } 0.100 \text{ W excess power}$$

$$t_{1/2} = 3.86 \times 10^{22} \text{ atoms} / (4 \times 2.6174 \times 10^{12} \text{ atoms/s}) = 3.687 \times 10^{10} \text{ s}$$

$$t_{1/2} = 1170 \text{ years} \quad (P_A = 0.100 \text{ W})$$

Electromigration / Preparata (Large Excess Power Effect)

- Long Palladium Wires of Small Diameters (50 μ).
- Flow of Current Along Wire Plus Electrolysis Current
- Produces Flux of Deuterons (D^+) Towards Negative End of Wire. Creates Region of High D^+ and e^- Concentration.
- Wire Encapsulated Near Negative End.
- Large Excess Power Effects / Melting of Palladium Wire.

References

G. Preparata, M. Scroletti and M. Verpillé, "Isobaric Calorimetry on Modified Fleischmann-Pons Cells", J. Electroanal. Chem., 411, 9-18 (1996).

(See also ICCF-6 Proceedings, Vol.1, pp. 136-143).

Acknowledgments

- Discussions with Professor Bockris in 2012 - 2013.
- Support from an Anonymous Fund at the Denver Foundation Through Dixie State University.
- Adjunct Faculty Position at the University of LaVerne.

Transmutations of elements by electrolysis, with light water and Copper electrodes.

Renzo Mondaini
ISCN member, Italy, e-mail: remond@tin.it

You get transmutations of elements by electrolysis, with a solution of Potassium Carbonate K_2CO_3 in light water and Copper electrodes.

The first LENR is a cold fusion: $^{16}_8O + ^{16}_8O \rightarrow ^{32}_{16}S$

This is achieved with the anode and cathode of Copper, powered by 12 Volt DC, and with a low to medium concentration of the solution.

The second LENR is a cold fission: $^{39}_{19}K - ^{16}_8O \rightarrow ^{23}_{11}Na$

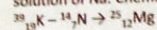
This is achieved with a high concentration of the solution.

At average concentrations, varying the size of the anode, it has the transition from one to another LENR; anode with small surface, generates the first reaction, anode with a large surface, generates the second reaction.

The tests of the first reaction are macroscopic, then visual: it produces 80% less Oxygen, and Sulfur compounds are created, many orders of magnitude higher than the impurities present in the electrolytic cell. Chemical analyzes have confirmed what was seen with the naked eye.

The tests of the second reaction, are not visible to the naked eye, since it seems to provide a simple water electrolysis, with production of Hydrogen and Oxygen in proportions 2-1, according to the Laws of Faraday.

However, performing this electrolysis for several days, adding distilled water for replenishing the water lost by evaporation, and replacing the anode when it is consumed, is obtained at the end a solution of Na. Chemical analyzes confirm the absence of K; but the presence of Mg, in significant quantity, one can assume its presence with the following third LENR of cold fission:



CAMPIONE	1106200	RICEVIMENTO	03/03/2011	PAGINA	1 di 1		
RAPPORTO DI PROVA n° 1106200							
Denominazione	Prodotto Campione solido Campionamento effettuato dal Committente						
DESCRIZIONE PROVA	RISULTATO	U	U.M.	LQ	LIMITI DI LEGGE	METODO	NOTE
Zolfo totale	53000	---	mg/kg	10	---	UNI13657	---

Metodi: UNI13657 = UNI EN 13657:2004 + EPA 6010C 2007 - Data inizio: 03/03/2011 Data fine: 11/03/2011

Chemical analysis of the solid sample, obtained by evaporation of the solution.

The sample weighed about 2 grams, and appeared to have been produced 0.1 grams of sulfur; the equivalent of 2-3 grains of rice.

2. Risultati

2.1. Campione solido

Elemento	Conc.
Na	7,483
Cu	52,53
P	0,04
S	0,02
Ca	0,03

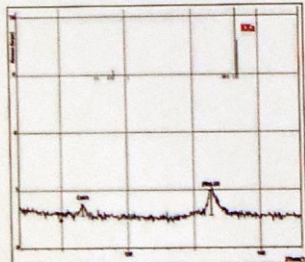


Fig. 1 - Spettro di fluorescenza a raggi X del campione solido nella regione del potassio - Kα (Kα). Picco del potassio assente.

X-ray fluorescence spectrum of the solid sample, in the region of the potassium. Potassium absent.

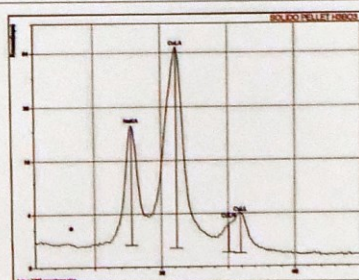


Fig. 2 - Spettro di fluorescenza a raggi X del campione solido, nella regione del sodio - Na (NaKα) e rame - Cu (CuKα).

X-ray fluorescence spectrum of the solid sample, in the region of the sodium and copper.

2.2. Campione liquido

Elemento	Conc.
Na	3,141
Cu	0,2
S	0,06

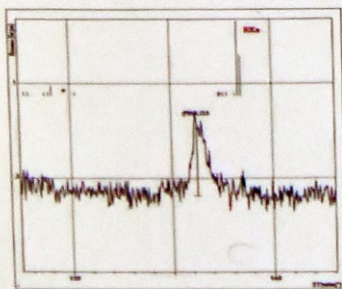


Fig. 3 - Spettro di fluorescenza a raggi X del campione liquido nella regione del potassio - Kα (Kα). Picco del potassio assente.

X-ray fluorescence spectrum of the liquid sample, in the region of the potassium. Peak potassium absent.

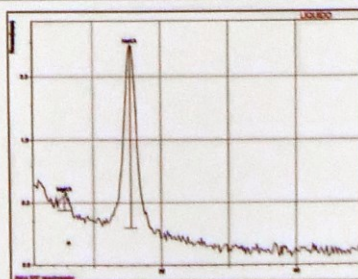
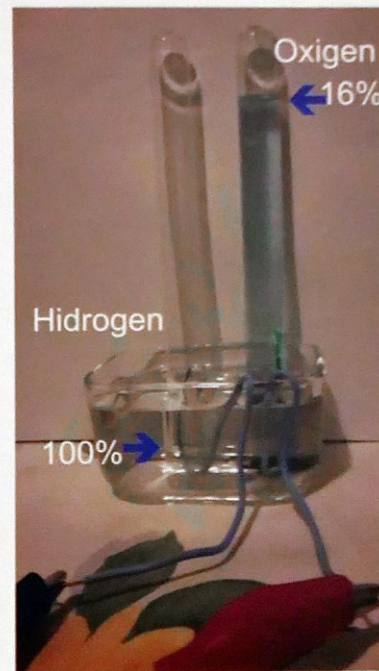
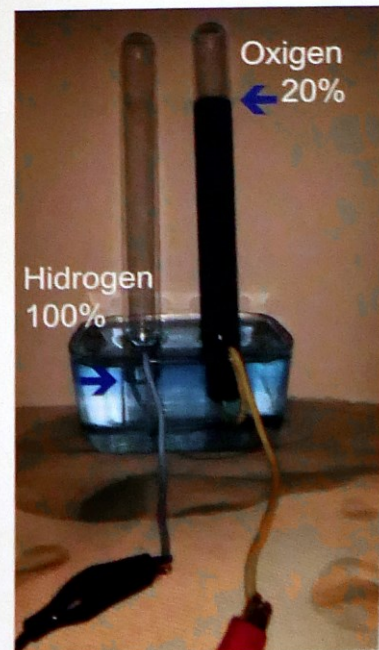


Fig. 4 - Spettro di fluorescenza a raggi X del campione liquido nella regione del sodio - Na (NaKα) e rame - Cu (CuKα). Si nota presenza di Na e piccole quantità di Mg. Il picco di CuLα (visibile in Fig.2) è assente per la scarsa quantità di Cu e il fatto che l'analisi dei liquidi viene effettuata in He e non in vuoto come per i solidi.

X-ray fluorescence spectrum of the sample liquid, in the region of the sodium and copper. It is noted the presence of Na, and small amounts of Mg. The peak CuLα (visible in Fig.2) is absent for the low amount of Cu, and the fact that the analysis of liquids is carried out in He, and not in vacuum as for solids.



Low concentration solution:
The first LENR starts $^{16}_8O + ^{16}_8O \rightarrow ^{32}_{16}S$



Slightly more concentrated solution:
The first LENR starts $^{16}_8O + ^{16}_8O \rightarrow ^{32}_{16}S$
and the beginning of the second LENR $^{39}_{19}K - ^{16}_8O \rightarrow ^{23}_{11}Na$

The Basis for Electron Deep Orbits of the Hydrogen Atom

J. L. Paillet¹, A. Meulenberg²

¹Aix-Marseille University, France,

jean-luc.paillet@club-internet.fr

²Science for Humanity Trust, Inc., USA

Abstract

We look into the difficult question of electron deep levels in the hydrogen atom, the importance of the deep orbits for research in the LENR domain, and some general considerations on these orbits as "anomalous" (and usually rejected) solutions of the relativistic quantum equations.

Arguments against the deep orbits are stated and addressed. Most of the problems are related to the singularity of the Coulomb potential when considering the nucleus as a point charge. They can be easily resolved when considering a more realistic potential with finite value inside the nucleus.

We consider specific works on deep orbits as solutions of the relativistic Schrödinger and of the Dirac equations, named Dirac Deep Levels (DDLs). The latter presents the most complete solution and development for spin 1/2 particles, and includes an infinite family of DDL solutions. We examine particularities of these DDL solutions and more generally of the anomalous solutions. Next we analyze the methods for, and the properties of, the solutions that include a corrected potential inside the nucleus, and we examine the questions raised by this new element.

Open questions remain: what is the physical meaning of the quantum numbers determining the DDL levels; how can angular momentum, two orders-of-magnitude lower than values associated with the Planck constant, still separate energy levels.

Companions papers: - *The Nature of the Deep Dirac Levels*. A.Meulenberg, J.L.Paillet

- *The Basis for femto-molecules and -ions created from femto-atoms*. A.Meulenberg, J.L.Paillet

Electron deep orbits are:

- Electron bound states of hydrogen atom with mean radius of order femto-meters
- Levels predicted by *relativistic* Schrodinger (Klein-Gordon) and Dirac equations (called Deep-Dirac Levels, or DDLs)
- Quantum states of "anomalous" solutions, usually rejected because the wave-function has a singular point at $r=0$.

Cold Fusion interest in deep orbits

Femto-atoms with deep-orbit electrons can:

1. facilitate **cold fusion inside condensed matter**
 - Tightly bound electrons provide super-strong screening
2. avoid **nuclear fragmentation** in a d-d fusion process
 - Potential energy of deep orbits draws mass from proton
3. increase the **rate of near-field, radiant-energy, transfer** between an excited nucleus and the surrounding lattice
4. create **femto-molecules** and combine with lattice nuclei for transmutation without energetic radiations

Principal arguments against the anomalous solutions of the Hydrogen Atom

1. the wave function has a singular point at the origin
It includes a factor f such that $f \propto r^{-2}$ where $s > 0$
2. the wave function cannot be square integrable
Behavior of $|R(r)|^2 r^2$ at the origin
3. the orthogonality of eigenvectors cannot be satisfied
Condition for Dirac solution components: $(f_k^* g_k - f_k g_k^*) > 0$ when $r \rightarrow 0$,
4. a paradoxical relationship between the coupling constant α and the binding energy
If one imagines that α decreases, then $|BE|$ increases. BE : Binding Energy

Resolution of these questions

- 1., 2., 3. are related to the singularity of the Coulomb potential with a point nucleus \Rightarrow
- (i) To compute DDL orbits with a finite potential inside the nucleus
or
- (ii) To compute with the electron *anomalous magnetic moment*, which "regularizes" the Coulomb potential, by repulsive terms in V'

$$D_r = \begin{pmatrix} mc^2 + V(r) & \hbar c \left(-\frac{d}{dr} + \frac{k}{r} \right) - \mu_a V'(r) \\ \hbar c \left(-\frac{d}{dr} + \frac{k}{r} \right) - \mu_a V'(r) & mc^2 - V(r) \end{pmatrix} \quad V = C/r \Rightarrow V' = -C/r^2$$

- 4. results from an ill-defined context: $\alpha = e^2/\hbar c$
 $\Rightarrow \alpha$ is entangled with three fundamental constants, but are they really constant in the limit as α goes to zero?

Open questions and future work

- What is the effect of adding **nuclear spin** to the Hamiltonian?
- **Special relativity** seems decisive for finding DDLs solutions. Why?
- DDLs are in an **extreme EM field** \Rightarrow strengthening of special known effects?
- Computation of the radial functions after **correcting potential** from $r = 0$ to infinity, and computation of the electron density
- Computation with taking into account the **anomalous electron magnetic moment**

Conclusions

Arguments against the anomalous solution of the Dirac equations for the Coulomb potential were **presumed** to be applicable to the hydrogen atom

They were not, since an atom has **no known singularity**.

A better representation of the H atom gives **2 valid solutions** to both the relativistic Schrodinger and Dirac equations.

Cold fusion provides strong evidence for the existence of these electron deep levels and these levels provide a basis for understanding CF (see refs) and for physics and chemistry research beyond CF.

Deep orbits solutions obtained by means of the Dirac equation - Works of Maly & Va'vra

Dirac equation with external Coulomb potential $V = \alpha \hbar c / r$

$$E^2 = \mathbf{p}^2 c^2 + m^2 c^4 \longrightarrow (i \hbar \partial_t + i \hbar \boldsymbol{\alpha} \cdot \nabla - \beta m c^2 + V) \Psi(t, \mathbf{x}) = 0$$

- Spin-orbit interaction \Rightarrow angular momentum Q number k defined from Total Angular Momentum $\mathbf{J} = \mathbf{L} + \mathbf{S}$ (4-D)
- Corresponding physical effect: electron precession

$$\alpha \cdot \mathbf{p} = \frac{1}{r} (\boldsymbol{\alpha} \cdot \mathbf{x}) (\mathbf{p} \cdot \mathbf{x}) + \frac{i \hbar}{r} \beta K \longrightarrow \hbar K = \beta (\Sigma \cdot \mathbf{L} + \hbar) \longrightarrow \hbar^2 K^2 = \mathbf{J}^2 + \frac{1}{4} \hbar^2$$

- Dirac relativistic corrections

$$H' = mc^2 + \frac{\mathbf{p}^2}{2m} + V - \frac{\mathbf{p}^4}{8m^3 c^2} + \frac{1}{2m^3 c^2} \frac{1}{r} \frac{dV}{dr} \boldsymbol{\sigma} \cdot \mathbf{L} + \frac{\hbar^2}{8m^2 c^2} \Delta V$$

Rest mass Usual KE correction Spin-orbit (Larmor-Thomas prec.) Darwin

"Anomalous" solutions

- Radial equations define a parameter s , with $s^2 = k^2 - \alpha^2$
- If taking the square root with sign "+" \rightarrow regular energy solutions
- else \rightarrow anomalous solutions, usually rejected.

$$E = mc^2 \left[1 + \frac{\alpha^2}{(n' - \sqrt{k^2 - \alpha^2})^2} \right]^{-1/2} \quad n': \text{radial quantum number}$$

Work of Maly and Va'vra :

1. Solutions from both relativistic Schrodinger and Dirac Eqs.
2. Solutions with usual Coulomb potential, next
3. Solutions with corrected Coulomb potential with finite potential inside the nucleus

Features of the DDL solutions

- There is an *infinite* set of DDL solutions
- DDL solution when $n' = k \Rightarrow$ Total energy $E \sim mc^2 (\alpha/2k)$
 $\Rightarrow E \ll mc^2$
- The binding energy $|BE| = |TE - mc^2|$ is near mc^2 , $|BE| > 509 \text{ keV}$
- The DDL orbits are very deep: mean radius r of order fm
- When k increases, then $|BE|$ increases and r decreases

References for this paper

- J.A. Maly, J.Vavra. *Electron Transitions on Deep Dirac Levels I*, Fusion Technol., **24**, p.307, 1993.
J. Maly and J.Va'vra, *Electron Transitions on Deep Dirac Levels II*, Fusion Technol., **27**, January 1995.
Jan Naudts. *On the hydrido state of the relativistic hydrogen atom*. arXiv:physics/0507193v2, August 2005.
B. Thaller. *The Dirac Equation*, Springer-Verlag, 1992.
L.I. Schiff. *Quantum Mechanics*. 3e Edition. Mc Graw Publ. Comp., 1968.
J.J. Sakurai, J.Napolitano. *Modern Quantum Mechanics*, 2d Ed. Addison-Wesley

Cold fusion papers based on electron deep levels

- A. Meulenberg and K.P. Sinha, "Extensions to Physics: Low-Energy Nuclear Reactions," presented at Space, Propulsion & Energy Sciences International Forum (SPESIF-11), March 15-17, 2011.
Meulenberg, A., Sinha KP (2009) Tunneling Beneath the Fragmentation Level. Proc. of 15th Int. Conf. on Cond. Matter Nucl. Sci. (ICCF-15), Rome, Italy
Meulenberg, A., Sinha KP (2010) Tunneling Beneath the 4He* Fragmentation Energy. J Cond Matter Nucl Sci, JCMNS 4:241-255
Meulenberg, A. "From the Naught Orbit to He4 Ground State" 16th International Conference on Condensed Matter Nuclear Science, Chennai, February 6 -11, 2011, JCMNS-10 p 15 - 29 (2013)
A. Meulenberg and K.P. Sinha, "New Visions of Physics through the Microscope of Cold Fusion" Invited paper, ICCF-17, Daejeon, Korea, August, 2012, J. Cond. Matter Nucl. Sci. **13** (2014), 378-390
A. Meulenberg and K.P. Sinha, "Deep-Orbit-Electron Radiation Emission in Decay from 4H* to 4He," 17th International Conference on Condensed Matter Nuclear Science, Daejeon, Korea, 12-17 August, 2012, J. Condensed Matter Nucl. Sci. **13** (2014), 357-368
A. Meulenberg, "Femto-atoms and Transmutation," 17th International Conference on Condensed Matter Nuclear Science, Daejeon, Korea, 12-17 August, 2012, J. Condensed Matter Nucl. Sci. **13** (2014), 346-357
A. Meulenberg, "Femto-Helium and PdO Transmutation," ICCF-18, 18th Int. Conf. on Cond. Matter Nuclear Science, Columbia, Missouri, 25/07/2013, <http://hdl.handle.net/10355/36500>, (to be published in JCMNS, Vol 15)
A. Meulenberg and K.P. Sinha, Deep-electron Orbits in Cold Fusion. 17th International Conference on Condensed Matter Nuclear Science, Daejeon, Korea, 12-17 August, 2012, Journal of Condensed Matter Nuclear Science **13** (2014) 368-377

The Launch of a New Plan on Condensed Matter Nuclear Science at Tohoku University

YASUHIRO WAMURA¹, SHOTA KASAGI², HIROSHI KUNAGA³,
HIDEKI YOSHINO⁴, TAKESHI ITOH⁵, MASAMICHI HATHORI⁶,
TADAMICHI MIYANO⁷

¹CONDENSED MATTER NUCLEAR REACTION RESEARCH CENTER FOR
ENVIRONMENTAL IMPACT, TOHOKU UNIVERSITY, JAPAN
²TOYOTA CENTRAL R&D LAB., JAPAN
³TOHOKU UNIVERSITY, JAPAN
⁴TOHOKU UNIVERSITY, JAPAN
⁵TOHOKU UNIVERSITY, JAPAN
⁶TOHOKU UNIVERSITY, JAPAN
⁷TOHOKU UNIVERSITY, JAPAN

Contents

1. Background
 - 1-1 Tohoku University
 - 1-2 Mitsubishi Heavy Industries, Ltd.
 - 1-3 Clean Planet Inc.
2. Condensed Matter Nuclear Reaction Division (April 2015 ~)
 - 2-1 Purpose of the Division
 - 2-2 Organization of the Division
 - 2-3 Outline of Research Plan
3. Concluding Remarks

1. Background

Tohoku University

Prof. Kasagi

[Fundamental Research on CMNR (screening etc.)]

Mitsubishi Heavy Industries, Ltd.

Iwamura, Itoh, Tsugano

[Deuterium Permeation Transmutation Experiments]

Clean Planet Inc.

Toshino, Hatfist, Igarashi

[Excess Heat Experiments with Dr. Mizuno]

1-1 Tohoku University (1)

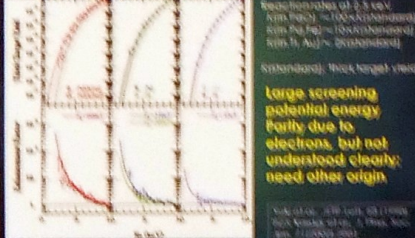
Low-energy deuteron generator at Tohoku Univ.



- $E_d = 0 \sim 100 \text{ keV}$
 $0.5 \sim 100 \text{ keV}$: acceleration mode
 $0 \sim 0.5 \text{ keV}$: deceleration mode
- I_d up to 500 μA

1-1 Tohoku University (2)

Anomalous enhanced DD reaction in metal

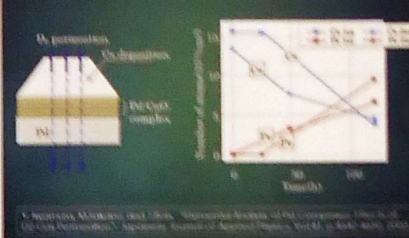


Reaction rates of $D+D$ and $D+T$ are 100% (standard) from the point of view of the standard reaction. However, the reaction rate of $D+D$ is 100% (standard) from the point of view of the standard reaction. However, the reaction rate of $D+D$ is 100% (standard) from the point of view of the standard reaction.

Large screening potential energy partly due to electrons, but not understood clearly; need other origin

1-2 Mitsubishi Heavy Industries (1)

Deuterium Permeation Transmutation Experiments



1-2 Mitsubishi Heavy Industries (2)

Summary of Transmutation Reactions observed so far



1-2 Mitsubishi Heavy Industries (2)

Summary of Transmutation Reactions observed so far

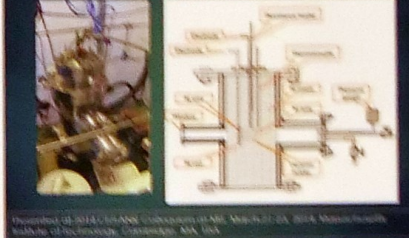
1-2 Mitsubishi Heavy Industries (3)

Independent Reproduction Experiments by Toyota Central R&D Labs.



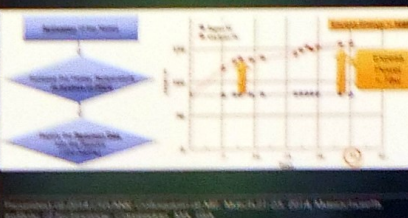
1-3 Clean Planet Inc. (1)

Experimental Set-up



1-3 Clean Planet Inc. (2)

Excess Heat Generation



Presented at 2014 CMNR Symposium at MIT, March 21-25, 2014, Massachusetts Institute of Technology, Cambridge, MA, USA

2. Condensed Matter Nuclear Reaction Division (April 2015 ~)

It belongs to
Research Center for Electron Photon Science,
Tohoku University, Sendai,
Japan



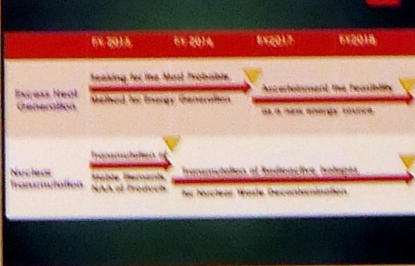
2-1 Purpose of the Division

1. Fundamental Research on Condensed Matter Nuclear Reaction (CMNR)
 - Systematic Data on CMNR
 - Improve the reliability of Measurement of CMNR
2. Development of a New Energy Generation Method
 - Most Probable Method for Energy Generation
 - Ascertain the Feasibility as a new energy source
3. Development of a New Nuclear Waste Decontamination Method
 - Enhance the rate of transmutation
 - Supported by the IMPACT R&D Program

2-2 Organization of the Division



2-3 Outline of Research Plan



3. Concluding Remarks

- This is the first official research division created for condensed matter nuclear reaction (CMNR) and its application in Japan.
- At this division, we will obtain fundamental data on nuclear reaction in anomalous heat generation phenomena, as well as in nuclear transmutation phenomena.
- We hope to bring revolutionary changes to the world through the conceptual change of conventional nuclear reaction.

Backup Slides

ImPACT R&D Program

Reduction and Resource Recycle of High Level Radioactive Wastes with Nuclear Transmutation

To obtain nuclear reaction data for long-lived fission products, and to confirm the world's first nuclear reaction path for conversion to short-lived nuclides or stable nuclides.

- Project 1: Development of separation and recovery technologies
- Project 2: Obtained nuclear reaction data, a new nuclear reaction model
- Project 3: Reaction theory modeling and simulation
- Project 4: Evaluation of nuclear transmutation system and development of experimental technologies
- Project 5: Process concept for design

A part of this project

Members of the Division

- Research Center for Electron Photon Science, Tohoku University, Japan
 - Shota Kasagi
 - Yasuhiko Wamura
 - Hideaki Yoshino
- Clean Planet Inc., Japan
 - Hideaki Yoshino
 - Takeshi Itoh
 - Masamichi Hatori
- HEAD, Japan
 - Tadamichi Miyano

Lifetime of Hot Spots

Jacques Ruer
jr.ruer@orange.fr

INTRODUCTION

Some LENR experiments show that energetic events are taking place at the surface of the cathodes, described as hot spots, reaction bursts, or micro-explosions [1-9]. In some cases, small-sized craters are seen after the experience, with features inviting to consider that a high temperature was briefly developed during their formation. As a general trend, such reactions seem to happen in very small spots and to last a very short time. The origin of the energy together with the complete formation process remain to be understood.

A model has been developed in order to give an insight on the potential lifetime of such hot spots and to show the relationships between the hot spot size, the energy input, the reaction kinetics and the peak temperature reached during an event.



Figure 1: Large crater with a rounded shape. There are evident signs of melting of the ejected material, some of it solidified around the crater rim. The diameter of this crater is 50 μm . The original point of the explosion seems to be located several tens of μm below the surface [3].

SIMULATION

Let us consider a given volume of the cathode metal which delineates the site of the energetic event. The site is simulated as a hemisphere with a radius R (m) located just at the surface of the cathode. The energy E (J) is released uniformly within this volume at a constant rate during the reaction time τ (s). The energy input can be related to a potential temperature rise according to the formula:

$$(1) \Delta T_{\text{max}} = E / (2/3 \pi R^3 \cdot \rho \cdot c) \quad \text{where } \rho \text{ is the specific mass of the metal (12023 kg.m}^{-3} \text{ for Pd)} \\ \text{and } c \text{ is the specific heat (245 J.kg}^{-1} \text{ for Pd)}$$

ΔT_{max} would correspond to the temperature rise of a perfectly adiabatic phenomenon.

COOLING MODES

The hot spots lose the heat via 3 different cooling mechanisms: 1) radiation by the surface – 2) convection in the liquid electrolyte – 3) conduction within the surrounding metal. In order to clarify the relative influence of the different modes of cooling, we consider an hypothetical site which is a half-sphere with a diameter of 100 μm . (radius $R = 50 \mu\text{m}$). Table 1 shows the heat flows of the different cooling modes. The order of magnitude of the various modes can be obtained by the following equations:

Conduction: (2) $F_{\text{conduction}} = S \cdot \lambda / R \cdot \Delta T = 2 \pi R^2 \cdot \lambda / R \cdot \Delta T$ where λ is the metal thermal conductivity (71 W.m⁻¹.K⁻¹ for Pd)

Convection: Because the phenomenon is very rapid, the heat transfer to the liquid at the onset of the convection can be approached as a pure conduction transfer:

(3) $F_{\text{convection}} = S \cdot \lambda_{\text{e}} / R \cdot \Delta T = \pi R^2 \cdot \lambda_{\text{e}} / R \cdot \Delta T$ where λ_{e} is the liquid thermal conductivity (0.6 W.m⁻¹.K⁻¹ for D₂O)

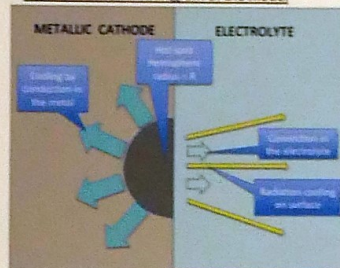
Radiation: If the hot spot radiates like a black body, the heat flux is: (4) $F_{\text{radiation}} = S \cdot \sigma \cdot (T^4 - T_a^4) = \pi R^2 \cdot \sigma \cdot (T^4 - T_a^4)$ where σ is the Stefan-Boltzmann constant and T_a the bath temperature

Table 1: comparison of the heat flow rates at the initial cooling of a large 100 μm diameter hot spot ($R = 50 \mu\text{m}$)

Heat transfer mode	Conduction within the cathodic metal	Convection into the electrolyte	Radiation at surface
Hypothetical temperature rise	100 K	100 K	100 K (2000 K)
Heat flow	2.23 W	0.01 W	8 μW (7 mW)
Relative influence	0.996	0.004	0 (0.003)

Conduction is the main mode of cooling. Radiation has little influence, even at very high temperature. For smaller hot spots, the relative influence of radiation is even lower. Therefore, the model takes only conduction into account to calculate the temperature evolution. The model is built on a Excel spreadsheet, using the classical Fourier equation in spherical form.

Figure 2: Schematic diagram of the model



RESULTS

Figure 3: Examples of temperature evolution for a 10 μm diameter hot spot ($A = 345 \text{ ns}$) Influence of the reaction time τ

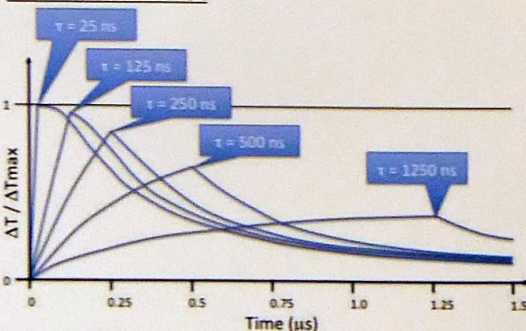


Figure 3 shows an example of the temperature evolution of hot spots with a 10 μm diameter ($R = 5 \mu\text{m}$), for various reaction times τ .

The results of the model indicate that the peak temperature is close to the adiabatic value ΔT_{max} , if the reaction time τ is shorter than a characteristic value A . This one can be derived from the equations (1) and (2):

$$(5) A = E / F_{\text{conduction}} = 1/3 R^2 \cdot \rho \cdot c / \lambda$$

It can be inferred that the peak temperature is related to the reaction time by the following relationships:

$$(6) \tau < A \rightarrow \Delta T = \Delta T_{\text{max}} \quad - \quad \tau > A \rightarrow \Delta T / \Delta T_{\text{max}} = A / \tau$$

Table 2 – Characteristic cooling time and peak temperature elevation reached following the duration of the heat generation event on palladium cathodes

Crater diameter: 2 μm - Characteristic cooling time $A = 13 \text{ ns}$				
Event duration τ :	$\ll A$	10 ns	100 ns	300 ns
Relative peak $\Delta T / \Delta T_{\text{max}}$:	1.0	0.86	0.22	0.09
Crater diameter: 10 μm - Characteristic cooling time $A = 345 \text{ ns}$				
Event duration τ :	$\ll A$	2 μs	20 μs	40 μs
Relative peak $\Delta T / \Delta T_{\text{max}}$:	1.0	0.65	0.12	0.07

CONCLUSIONS

Small sized hot spots, as they are observed on Pd cathodes, have a very short lifetime. Their heat is rapidly dissipated by conduction into the surrounding metal. Radiation cooling at the surface is almost negligible even at high temperature, as well as convective cooling by the liquid electrolyte. If the hot spots which create craters with melted debris result from LENR, the model shows that the reaction time must be shorter than A (It may be several orders of magnitude lower, what this model cannot predict).

If the hot spots result from chemical processes, the reaction times are in general much longer than A and the peak temperature can only be limited.

However, it should be remembered that some craters, not related to hot spots, may result from the mechanical interaction of hydrogen with the metal structure, e.g. blisters.

REFERENCES

- [1] D. Cirillo and V. Iorio, Transmutation of metal at low energy in a confined plasma in water, 2004, ICCF 11
- [2] Y. Toriyabe et al., Elemental analysis of palladium electrodes after Pd/Pd light water critical electrolysis, 2005, ICCF 12
- [3] S. Szpak, P.A. Mosier-Boss and F.E. Gordon, Experimental evidence for LENR in a polarized Pd/D lattice, NOAA 2006 Naval S&T Partnership Conference, Washington DC, <http://lenr-canr.org/acrobat/SzpakExperiment.pdf>
- [4] W. Zhang and J. Dash, Excess heat reproducibility and evidence of anomalous elements after electrolysis in Pd/D₂O + H₂SO₄ electrolysis cells, 2007, ICCF 13
- [5] I. Dardik, T. Zilov, H. Branner, A. El-Boher, E. Greenspan, B. Khachaturov, V. Krakov, S. Lesin, A. Shapiro and M. Turlin, Ultra-sonically-excited electrolysis experiments at energetics technologies, 2008, ICCF 14
- [6] David J. Nagel, Characteristics and energetics of craters in LENR experimental materials, J. Condensed Matter Nucl. Sci. 10 (2013) 1–14.
- [7] Y. E. Kim, Theory of Bose-Einstein condensation mechanism for deuteron-induced nuclear reactions in micro/nano-scale metal grains and particles, Naturwissenschaften, Published online 14 May 2008, DOI 10.1007/s00114-009-0537-6
- [8] Y. E. Kim, The Explanation of Low Energy Nuclear Reaction, Infinite Energy Press, 2014
- [9] J. Ruer, Simulation of Crater Formation on LENR Cathodes Surfaces, 2013, J. Condensed Matter Nucl. Sci. 12 (2013) 1–16

LENR INVEST OVERVIEW

Management Team



Tyler van
Houwelingen



Michael
(Rocket)
Halem



Dr. Antoine
Guillemain

We believe that a new era in energy is coming

Our Mission is to enable and promote LENR technologies and IP through selected investments and synergies.

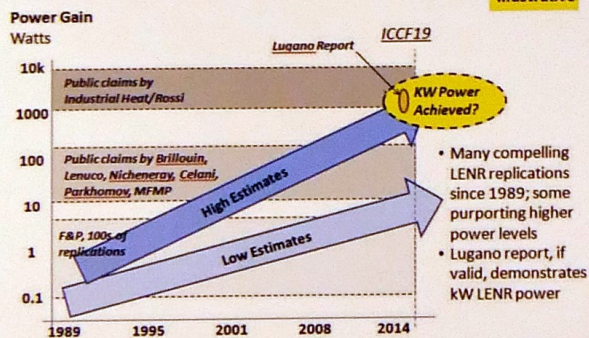
Our Strategy is to bridge the gap between a lab demo and an industrial prototype, by funding companies at this early stage. We also work as a technology watcher to keep both the investors and the companies we invest in, updated with the latest industry developments and strategy.

LENR-INVEST HAS INVESTED IN 5 LENR LEADERS

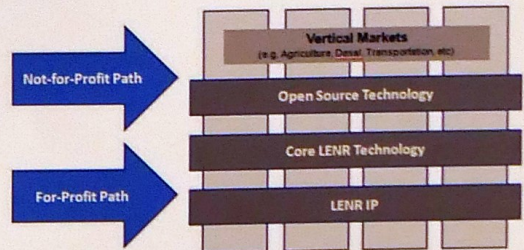
Firm	Leader	Location	Date
Lenuco	Prof. George Miley	Champagne, Illinois	3/14
Brillouin	Robert Godes	Berkeley, California	4/14
Investment not yet public			4/15
LENR-Cars	Nicolas Chauvin	Lausanne, Switzerland	7/14
LERNProof	Tyler VH	Grand Haven, Michigan	3/14

LENR MAY BE APPROACHING COMMERCIAL LEVELS

Illustrative



PATHS TO LENR COMMERCIALIZATION



We are looking for early stage firms, scientists and/or entrepreneurs who have strong LENR core technology, Intellectual Property or vertical LENR applications

An example of the nuclear active environment (NAE) in the cold fusion

Tetsuo Sawada
(Nihon Univ., Hosei Univ.)

Deuteron ratio and the symmetrized Maxwell eqs.

It is interesting that the deuteron ratio D/H of the comet Tyurimov-Gerashimenko is around 3 times large compared to that of the earth. It seems to suggest that the nuclear reaction $d+d \rightarrow \alpha$ proceeds on the earth or on the planets with magnetic field such as the earth or the Mercury. It is evident that the density of the magnetic monopole is relatively high in the neighborhood of the north or the south geo-magnetic poles.

$$\begin{aligned} \text{rot } \vec{H} - \frac{\partial \vec{D}}{\partial t} &= \vec{i} \\ \text{rot } \vec{E} + \frac{\partial \vec{B}}{\partial t} &= * \vec{i} \\ \text{div } \vec{B} &= * \rho \\ \text{div } \vec{D} &= \rho \end{aligned}$$

Above equations are the symmetrized Maxwell equations. In the limit of $*\rho=0$ and $*\vec{i}=0$, they reduce to the ordinary Maxwell equations.

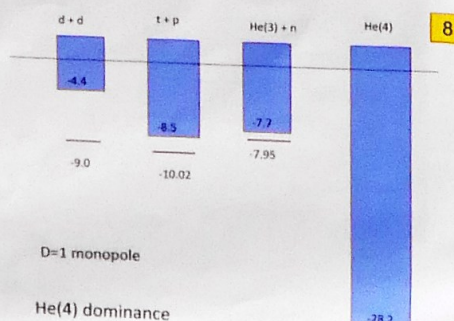
Charge quantization condition of Dirac and Schwinger

If we remember that in the quantum theory, a component of the angular momentum L can assume only the half-integer multiple of \hbar , we arrive at the charge quantization condition: $DZ *ee/c = (\hbar/2) n$ with $n=0, \pm 1, \pm 2$ in which $*e$ and e are the smallest non-zero values of $*Q$ and Q respectively.

Z is the electric charge number and D is the magnetic counterpart of Z , $D=1$ and $D=2$ are for the Dirac's and Schwinger's magnetic monopole respectively.

The most important conclusion of the charge quantization condition is the super-strong nature of the interaction between the magnetic mono-poles. $*e^2/\hbar c = 137/4$, which is the magnetic counterpart of the ordinary fine structure constant, namely $e^2/\hbar c = 1/137$. When we examine the nuclear reaction in the external magnetic Coulomb potential, we must include $*ee$ term.

Hamiltonian [1]
The Hamiltonian H of the deuteron- magnetic monopole system ($*e$ - d) is:
 $H = H_0^d + H_0^e + V_N$ with $H_0 = \frac{1}{2m} (-i\vec{\nabla} - Z\vec{A})^2 + \kappa_{sd} (*ee/2m_p) F(r) (\vec{\sigma} \cdot \vec{r})/r^3$
 \vec{A} is the vector potential whose rotation is the magnetic field strength, which is the magnetic Coulomb field in our case: $\text{rot } \vec{A} = \vec{B} = *e \vec{r}/r^2$. κ_{sd} is the magnetic moment of the nucleon in the unit of the nuclear magneton $e/2m_n$. $F(r)$ of the last term is the form factor of the proton and neutron.
 V_N is the nuclear potential between nucleons. In order to estimate the binding energy of the ground state of the d - $*e$ system the variational calculation is applied, in which $\langle \Psi | H | \Psi \rangle / \langle \Psi | \Psi \rangle$ is minimized. It turns out that the binding energy of d - $*e$ is $B_{d-*e} = 2.3$ MeV. Since the nuclear cold fusion starts after two deuterons are trapped in the ground state of d - $*e$, the starting energy level is $E = -2(2.2 + 2.3) = -9.0$ MeV. When the cold fusion starts from $E = -9.0$ MeV, it cannot reach to the continuous spectrum of t - p and $\text{He}(3)+n$ because of the energy conservation (shown as the horizontal green line). On the other hand, concerning the channel $\text{He}(4)$, it stays open and the magnetic monopole can emit the α -particle with the kinetic energy $T_{\alpha} = (28.2 - 9.0) = 19.2$ MeV.



Magnetic charge density, Maxwell equations

It is believed that in the process of the big-bang, the magnetic monopoles, which are the magnetically charged particles, are produced abundantly. However as the universe expands the density of the magnetic monopole decreases and today it becomes the rare particle. $*\rho=0$ and $*\vec{i}=0$, in which $*\rho$ and $*\vec{i}$ are the magnetic charge density and the magnetic current density respectively.

$$\begin{aligned} \text{rot } \vec{H} - \frac{\partial \vec{D}}{\partial t} &= \vec{i} \\ \text{rot } \vec{E} + \frac{\partial \vec{B}}{\partial t} &= 0 \\ \text{div } \vec{B} &= 0 \\ \text{div } \vec{D} &= \rho \end{aligned}$$

Maxwell equations above do not have the duality invariance, which means interchange of the electric and the magnetic objects: $D \rightarrow B$, $B \rightarrow D$ and $\rho \rightarrow * \rho$, $* \rho \rightarrow -\rho$ etc.

Extra angular momentum of the $*Q$ - Q system

In 1970's, quantum mechanics of the magnetic monopole and the electrically charged particle ($*Q$ - Q) has been studied extensively. Their most important difference from the ordinary quantum system is the appearance of the extra angular momentum in addition to the ordinary orbital angular momentum term L_{orb} :
 $L = m \vec{r} \times \vec{v} + (*QQ/c) \vec{r}$
where \vec{r} is the unit vector connecting magnetic charge $*Q$ and the electric charge Q .

The second term of the L is obtained if we evaluate the integration $\vec{r} \cdot \vec{p}$ of the angular momentum density $\vec{E} \times \vec{H}/c$ of the electro-magnetic field, where $\vec{H} = Q * (\vec{r} / r^3)$ and $\vec{E} = Q ((\vec{r} \cdot \vec{r}) / (r^3 - r^2))$, namely the Coulombic fields produced by Q at $\vec{r}=0$ and $*Q$ at $\vec{r}=0$.

Magnetic monopole as the catalyst of the cold fusion reaction

Magnetic Coulomb field produced by the magnetic monopole can attract the particles with the magnetic dipole moment such as the proton, the neutron or the deuteron. On the other hand, α -particle cannot be attracted, since its spin is zero. By solving the Schrödinger equation with the Hamiltonian given in the next page, we can determine the distorted outgoing wave of the α -particle, and also the wave functions of the bound states of p - $*e$, n - $*e$ and d - $*e$ which are calculated by the standard method. It is interesting to consider when two deuterons are trapped by the same magnetic monopole $*e$, since the orbit radius of d is around several fm., two deuterons must fuse to become more stable α -particle, and it is simply emitted. So the fresh magnetic monopole $*e$ remains, it starts to attract surrounding deuterons again. In this way $*e$ plays the role of the catalyst of the nuclear cold fusion: $d+d \rightarrow \alpha$.

It turns out that binding energy B of d - $*e$, t - $*e$ and $\text{He}(3)+n$ are 2.3, 1.52 and 0.25 MeV, respectively. So if we start from the ground state of d - $*e$ ($E = -9.0$ MeV) it cannot transit to t - p and $\text{He}(3)+n$ channels, on the other hand it can emit $\text{He}(4)$ with kinetic energy 19.2 MeV. (see the figure)

Hamiltonian [2]

The Hamiltonian of the nucleon- magnetic monopole system (N - $*e$) is

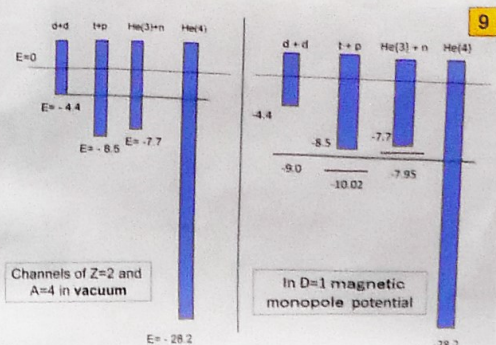
$$H_0 = \frac{1}{2m} (-i\vec{\nabla} - Z\vec{A})^2 + V_m(r)$$

The interaction term V_m of N - $*e$ is

$$V_m(r) = -\kappa_{sd} (e/2m_p) (*e/r^2) \vec{\sigma} \cdot \vec{r} F(r) \quad \text{where}$$

$$F(r) = 1 - e^{-ar} (1 + ar + a^2 r^2 / 2) \quad \text{with } a = 6.04 \mu_m^{-1}.$$

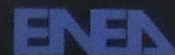
The size parameter a in the form factor function $F(r)$ relates to the radius of the nucleon by $\bar{r}^2 = 12/a^2$ which means the radius of proton is 0.811 fm.





Department of Physics
Center for Emerging Energy Sciences
at Texas Tech University

The Center to Study Anomalous Heat Effects [AHE] at Texas Tech University



Tara A. Scarborough¹, Robert Duncan¹, Michael McKubre² & Vittorio Violante³

¹Texas Tech University, ²SRI International, ³ENEA - Frascati

Motivation

The Center for Emerging Energy Sciences at Texas Tech University (CEES) has been established to explore critical parameters in the observation of the anomalous heat effects. A large number of experiments report the production of heat from metal samples loaded with hydrogen or deuterium in amounts that often thousands of times greater than the enthalpies of possible chemical reactions. The effect is anomalous because there is no agreed-to mechanism¹, and particle radiation rates are not reported at levels that are consistent with any known nuclear process.

Basis of Work

Heat-helium correlation was first documented by Miles² and co-workers in 1991 stating convincing evidence that their measured excess enthalpy correlated with $D+D \rightarrow {}^3\text{He} + 23.4 \text{ MeV}$ fusion reaction. These same results have been reported by at least seven laboratories in three countries (including two of the present authors in three different experimental modes at SRI and ENEA).

While necessary improvements have been made to calorimetry, triggering and data acquisition, much is still left to be understood about the process and mechanisms of excess heat release. The intent of the work described here is not to verify nuclear processes, specifically, but to gain a fundamental understanding of the mechanisms at play. Extensive materials characterization and eventual full reproducibility is the framework upon which the work performed at the AHE Center at Texas Tech University (TTU) will be built upon, permitting direct correlation of excess heat production to materials properties that will point to the mechanism of this currently anomalous effect.

Strategy

Sufficient characterization of the metal foils both before and after their use in electrolytic cells is a critical path for correlation studies. While this characterization technique has yet to be standardized, the authors have embarked upon a path to define the necessary information to identify parameters that correlate with anomalous heat release.

Large scale, high resolution imaging is essential to investigate surface features of the cathodes. This will be achieved by use of atomic force microscope (AFM), scanning electron microscope (SEM), and confocal microscope (CM). Each of these are available at the Imaging Center at TTU which shares the same building as the AHE Center at Texas Tech.

To achieve nanometer resolution of areas $\sim 1 \times 4 \text{ cm}$ will require automated image acquisition and stitching software integrated with the SEM to register location. The registration will allow for the user to easily return to regions of interest for imaging at a higher resolution. Foils included here were provided by the Violante Group at ENEA³.



Initial SEM image of Pd foil comprising 30 individual images that were stitched together.

Contact with FEI regarding equipment upgrades for this project resulted in small demonstration in which the palladium foil was scanned and automatically stitched together as the scan progressed. The images below show resolution of this composite scan at several levels of magnification.

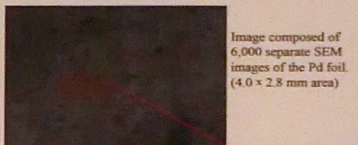
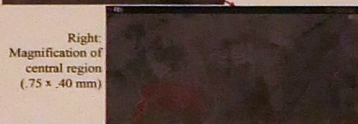


Image composed of 6,000 separate SEM images of the Pd foil. ($4.0 \times 2.8 \text{ mm}$ area)

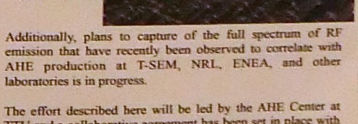
Right: Magnification of central region ($.75 \times .40 \text{ mm}$)



Left: Further magnification of central region ($.18 \times .07 \text{ mm}$)



Right: Magnification of central region ($.02 \times .01 \text{ mm}$)



Additionally, plans to capture the full spectrum of RF emission that have recently been observed to correlate with AHE production at T-SEM, NRL, ENEA, and other laboratories is in progress.

The effort described here will be led by the AHE Center at TTU and a collaborative agreement has been set in place with ENEA - Frascati (the Violante Group) to lead the further study of heat-helium correlations.

References

1. E. Storms, "The Science of Low Energy Nuclear Reactions", World Scientific, 2007.
2. M. Miles, B. F. Bush, G. S. Ostrom and J. J. Lagowski, "Heat and helium measurements in cold fusion experiments", in Proc. ICCF2, Italy, 1991, p. 363.
3. V. Violante, E. Castagna, S. Lecci, G. Pagano, M. Samonini and F. Sarto, "RF detection and anomalous heat production during electrochemical loading of deuterium in palladium", JAL, 2, 3/2014.
4. M. C. McKubre, F. L. Tancella, P. Topsis and P. L. Hagelstein, "The emergence of a coherent explanation for anomalies observed in D/D and H/D systems: evidence for 'He' and 'He' production", in Proc. ICCF8, Italy, 2000.
5. M. Agreola, E. Castagna, L. Capobianco, L. D'Alessandro, G. Macrì, F. Sarto, A. Rinaldi, V. Santoro, V. Violante, M. McKubre, F. Tancella, C. Sibilla, "Some Recent Results at ENEA", Proc. ICCF12, Japan, 2005, p.117.
6. F. L. Tancella, J. Bao, M. C. McKubre and P. L. Hagelstein, "Trapped nuclear energy release from palladium deuteride", SRI Final Report to ENEA on Contract H07RA1-08-AR05, 2012.
7. M. C. McKubre, J. Bao and F. L. Tancella, "Calorimetric studies of the destructive stimulation of palladium and nickel thin wires", in Proc. ICCF17, Korea, 2012.

Special Thanks:

Violante Group (ENEA - Frascati) • Doni Davis (Siemens)
Dr. Lin & Dr. Zhao (TTU Imaging Center) • Oxford Instruments & FEI - Houston
Undergraduate Laboratory Assistants: Thomas Hayes, Daniel Ballinger, & Chrome Akene

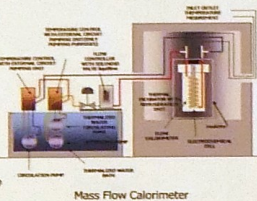
Experimental Variations

Electrolytic Cells

Based upon the pioneering work of Fleischmann and Pons, which has been further perfected by McKubre⁴, Violante⁵, and other authors, correlation and rates of excess heat and helium production of deuterium and/or hydrogen loaded palladium foils will be investigated. While this work will continue at the established ENEA facility, the AHE Center at Texas Tech will establish working cells to begin testing characterization techniques, described in Strategy, in the next few months.

When satisfactory operation is achieved at Frascati, closely similar apparatus will be assembled in the AHE Center at TTU to check site-to-site repeatability. It is possible that a third laboratory will be selected in the future to further check repeatability.

We have purchased a PXIe system from National Instruments to aid in the data acquisition and processing necessary for calorimetric results. The system is equipped with an Intel Core i7, 12-bit oscilloscope/digitizers, DMMS, 26.5 GHz spectrum analyzer, simultaneous data acquisition (ADC/DAC + DIO + Timing/Triggering), and 5.7 TB RAID drive.

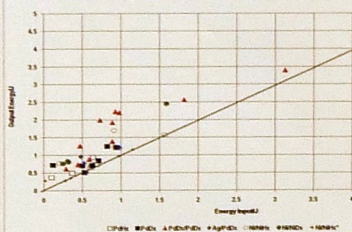


Mass Flow Calorimeter

Exploding Wires

Considerable effort has been made towards decreasing data acquisition times, and therefore experimental setup and turnover times. As such, deuterium loading of palladium wires has emerged as a feasible alternative to foils. However, the process of loading the wires requires ultra-pure reagents in an ultra-clean environment, which introduces a different set of experimental requirements.

The image below summarizes initial efforts made by Tancella, Bao, and McKubre^{6,7} to use of electrolytically loaded wires of various composition. The area below the line represents a region of no anomalous heat release, points above the line exhibit a significant percentage of excess heat.



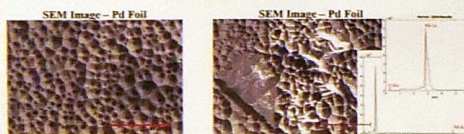
The AHE Center at TTU will be exploring the parameter space developed here in pursuit of correlations between the extent of heat release and helium production. Once operation is reached, site-to-site repeatability will be checked at Frascati.

Facility Establishment

Preliminary Results

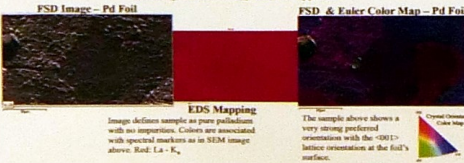
During the last three months, we have investigated the necessary components for sufficient optical characterization of the electrolytic foils. Currently we have use of a Hitachi S4300 SEM which can be upgraded to provide surface feature resolution at the nanometer-scale, Energy Dispersive X-ray Spectroscopy (EDS) results for compositional information, and Forward Scatter Detector (FSD) imaging to detail the crystal structure orientation of the entire surface of each foil.

Individual Images



Multi-Frame Images

These images are the result of 33 stitched individual images with 30% overlap to guarantee feature matching. No smoothing has been applied.



Custom Cryogenic Design

To initiate work on the exploding wire variations, Janis Research has assisted in the development of a custom research cryostat designed to operate with liquid argon (87K), liquid nitrogen (77K), or liquid helium (4K).

The expected consumption rate of LA is $\sim 0.4 \text{ L/hr}$ with radiation baffles and bubble diffusers to ensure thermal stability of boil-off measurements before and during experimentation. Neutron and gamma ray transparent windows have been included in line with wires for emission detection with AmpTek X-123 Charge Drift Detectors.



Mass Spectrometry

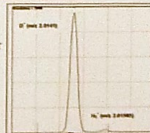
The AHE Center at TTU is in the process of establishing three separate methods of low-AMU mass detection for use in the previously mentioned experimental designs.

Leak Detection

The Pfeiffer ASM 340 leak detector is calibrated for detection of H_2 , He , and H_2 , with a minimum detection rate of $< 5 \cdot 10^{-12} \text{ Torr l/s}$. This apparatus will be used to ensure that all seals are hermetic, but can also be utilized as a baseline calibration for background levels of the species listed above.

Gas Chromatography - Mass Spectrometer (GC-MS)

The JOEL GCMate is a compact double focusing mass spectrometer that incorporates a gas chromatograph before a traditional mass spectrometer that has a range that extends as low as m/z 1 to 3000. The figure to the right was obtained from JOEL by monitoring H_2^+ and D^+ from a mixture of D_2O and H_2O (mass difference of 0.00155 amu) with a resolving power of 3400.



This instrument matches that used at ENEA - Frascati to facilitate in experimental repeatability once the AHE Center at TTU receives the mass flow calorimeter as described above.

Fourier Transform Ion Cyclotron Resonance (FT-ICR)

The Quanta Advance Mass Spectrometer utilizes a 1 Tesla magnet field ideal for confining small masses and lower voltages for small mass ion control. The piezo-electrically driven injection valve controls size and duration of sample sizes down to picoliter volumes while maintaining a consistent 10^{-10} Torr base pressure. Currently equipped with a 5 MHz waveform generator, the lowest detectable mass is 5.6 amu with a resolution of approximately 10,000, as it was originally designed for masses 2-1000, but utilizing the second harmonic helium and hydrogen can be trapped. Upgrading to a 40 MHz generator would move detection limit to masses greater than 0.7 amu with a resolution of 400,000 for hydrogen and 200,000 for helium.

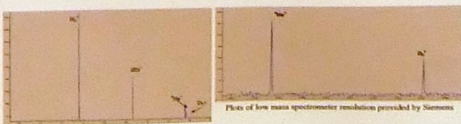


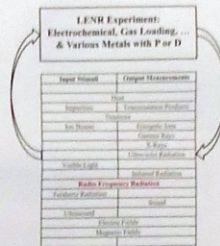
Photo of low mass spectrometer resolution provided by Siemens

Electromagnetic and Electronic Frequencies Associated with Heat Production During Electrochemical Loading of Deuterium into Palladium

Felix Scholkmann¹, David J. Nagel², Louis F. DeChiaro³
¹ Bellinzona 10, 8033 Zurich, Switzerland, Felix.Scholkmann@gmail.com
² The George Washington University, Washington DC, 20052, USA
³ Naval Surface Warfare Center, Dahlgren VA, 22448, USA

ICCF-19
 13-17 April 2015
 Padova, Italy

Input Stimuli and Output Measurements for LENR Experiments



This paper reviews the literature on the application of RF fields to LENR cells, and the appearance of RF frequencies within LENR experiments, and considers possible mechanisms involving RF receipt and generation.

Presentations and Papers on RF and LENR

There are two papers on the application of RF fields to LENR electrochemical cells:

Bockris et al. 1993
 Cravens 1994

Both of these showed an increase in excess power with application of RF. They imply some type of coupling between the RF and the mechanism causing LENR.

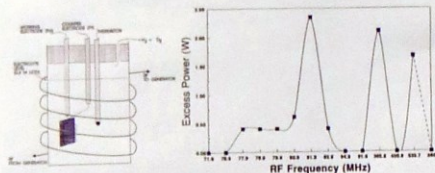
There are two reports on the generation of RF in LENR electrochemical cells:

NRL 2012 and 2015
 ENEA 2014

The primary issues in these papers is the origin of the RF, that is, whether it is due to the power supply or its interaction with the cells (an artifact), or else reflective of the basic mechanism active in LENR (and, possibly, interactive).

Can we learn something fundamental about LENR from RF-cell interactions?

Bockris et al 1993



RF stimulated excess power with D₂O, but not H₂O.
 "Heating by the RF was precluded ..."

J. G.M. Bockris, R. Sundaresan, Z. Minervál, D. Letts
 "Triggering of Heat and Sub-Surface Changes in Pd-D System"
 The Fourth International Conference on Cold Fusion (ICCF-4) Lakeland, Mani, Dec. 6-9, 1993
 Electric Power Research Institute, 3412 Hillview Avenue, Palo Alto, CA 94304 pp. 1-1 to 1-46

Cravens 1994

The imposition of RF fields in the range of 80 to 84 MHz likewise seem to trigger some anomalous heat reactions. This is done by pulsing (both sine and square wave) the magnetic field at the cell by wrapping the cell with a coil of wire and connecting it to a RF unit. The excess heat is enhanced by the application of the RF magnetic field. The apparent excess was roughly proportional the power level of the applied field. The effect was most pronounced when the RF coils are impedance matched at about 81.9 MHz.

This work was done at 200 mW of power and 5 to 10 turns on the field coils. Assuming a reasonably working cell is used (already at about 30%), the effect usually is quickly seen (within seconds or minutes). If the cell is run at above 70 or 80 C, the additional power levels are often large enough to cause rapid boiling. The increases are typically from the initial 30% to the 100-200% range and remain as long as the RF field is on. Often, cells receiving this treatment later seem to "run better" (>than the initial 30%).

D. Cravens, "Factors Affecting the Success Rate of Heat Generation in CF Cells"
 The Fourth International Conference on Cold Fusion (ICCF-4) Lakeland, Mani, Dec. 6-9, 1993
 Electric Power Research Institute, 3412 Hillview Avenue, Palo Alto, CA 94304 pp. 18-1 to 18-14

Summary of RF Input Experiments

Two early experiments indicate that application of RF EM frequencies in the 77-534 MHz range to operating LENR electrochemical cells increases the production of excess power.

The increase could be due to either of two causes:

- ▶ Coupling of the RF energy into the measurement system.
- ▶ The effect of RF on the mechanism causing LENR.

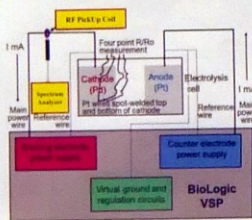
The first is ruled out by two observations:

- ▶ The increase in excess power is less than the total RF power.
- ▶ There is no increase in apparent power when the electrolyte is H₂O rather than D₂O.

The effect of incident RF on production of LENR does not require that the production of LENR necessarily produces RF within an experiment.

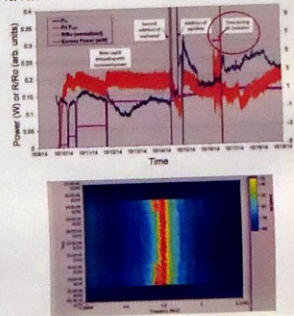
However, two experiments have found the appearance of RF within the circuit of an electrochemical experiment, sometimes during production of excess power, but sometimes without power production. Data follows.

Naval Research Laboratory 2012 and 2015

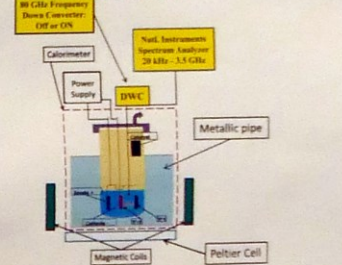


D. Dominguez, L. DeChiaro, D.A. Kidwell, A.E. Moser, V. Violante, G.K. Hubler, S.-F. Cheng, J.-H. He, D. L. Kaiss
 "Anomalous Results in Fleischmann-Paul Type Electrochemical Experiments"
 Conference Abstract, ICCF-17, August 12-17, Daegu, South Korea, 2012, Unpublished.
 D.A. Kidwell, D.D. Dominguez, K.S. Grahowski, L.F. DeChiaro Jr
 "Observation of Radio Frequency Emission from Electrochemical Loading Experiments",
 Current Science, vol. 108, pp. 1-4, 2015.

Naval Research Laboratory 2012 and 2015

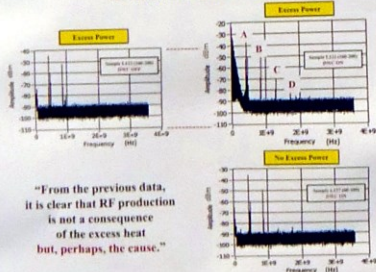


ENEA 2014



V. Violante, E. Castagna, N. Lotti, G. Pagano, M. Sammartino, E. Sarti
 "RF Detection and Anomalous Heat Production during Electrochemical Loading of Deuterium in Palladium"
 Energia, Ambiente e Innovazione, vol. 2-3, pp. 63-77, 2014.

ENEA 2014 and 2015



"From the previous data, it is clear that RF production is not a consequence of the excess heat but, perhaps, the cause."

K. Grahowski Question: Are peaks B, C and D harmonics of peak A?

Summary of RF Output Experiments

Two recent experiments show that operating LENR electrochemical cells can exhibit RF frequencies with or without the production of excess power.

Frequencies of 450-480 kHz and 4.8 to 5.8 MHz were measured at the NRL.

Frequencies of 430, 475 and 850 MHz, plus 1.28, 1.75, 2.45, 3.05 and 77-83 GHz were reported by ENEA.

There are three potential sources of the RF in the electrochemical circuits:

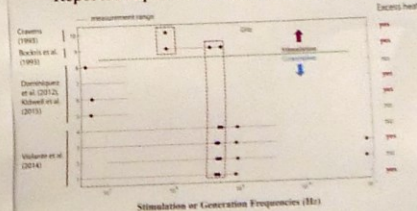
- ▶ The mechanism that causes LENR
- ▶ The power supply
- ▶ The interaction between the cell and the power supply

It is unlikely that the power supply can support frequencies in the GHz range.

GHz frequencies cannot propagate between the power supply and the cell.

Main question: How could production of LENR generate high frequencies?

Reported Input and Output Radio Frequencies



Note coincidence of peaks at about 80-84 MHz in work of Bockris et al and Cravens, and at about 300-400 MHz in the work of Bockris et al and ENEA, both shown by dotted red boxes.

Possible Mechanism: Esaki Diode or Gunn Device

These are semiconductor devices with areas of negative resistance that are used to generate RF in many systems.

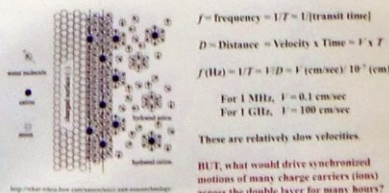
It can be asked if semiconductors might be deposited on the surface of cathodes to create such devices.

There are four requirements that make such deposition and operation unlikely.

- ▶ The doping profiles in both Esaki (tunnel) diode and Gunn device have to be very specific.
- ▶ Even if they could be deposited with the needed doping profiles, the entire cathode would have to be coated or the devices would be shorted.
- ▶ If such a complete coating was achieved, the current through the cell would be drastically affected.
- ▶ Finally, there are neither the needed voltages nor required circuits for RF oscillations due to such devices.

Possible Mechanism: Double Layer Oscillations

The double layer on the surface of a cathode is very thin, about 1 nanometer. Hence, even low velocities can span it in times compatible with RF.



$$f = \text{frequency} = 1/T \sim 1/(\text{transit time})$$

$$D = \text{Distance} = \text{Velocity} \times \text{Time} = V \times T$$

$$f(\text{Hz}) = 1/T = V/D = V \text{ (cm/sec)} \times 10^9 \text{ (cm)}$$

For 1 MHz, $V = 0.1 \text{ cm/sec}$
 For 1 GHz, $V = 100 \text{ cm/sec}$

These are relatively slow velocities.

BUT, what would drive synchronized motions of many charge carriers (ions) across the double layer for many hours?

Possible Mechanism: Deuteron Hopping

"The RF frequency is too high to originate from electrochemistry. It may be due to deuteron hopping between lattice sites in highly loaded Pd."

D.A. Kidwell et al, Current Science, vol. 108, pp. 578-581, 2015.

If the RF is associated with a phenomenon having the same spatial periodicity as the basic FCC lattice, then dividing the Pd lattice constant by the observed RF period for 5.3 MHz, we get a velocity near 0.25 cm/sec, consistent with known diffusional velocities.

The fact that there are hopping and diffusional frequencies within D loaded Pd similar to the frequencies reported from LENR experiments does not guarantee the generation of relatively monochromatic radio frequencies over long times (hours).

What can cause the frequency stability and the long times?

One possibility is a high Q resonance governed either by the physical dimensions of the cathode or perhaps by nonthermal anomalies in the occupation numbers of the acoustic branch phonons within the cathode.

Conclusion

The application of RF EM waves to LENR electrochemical cells was shown to increase excess power in two early experiments. This, by itself, makes it worth studying the intersection of electrochemical LENR cells and RF.

It is conceivable that the application of the external fields could align protons or deuterons in or very near cathodes to cause an effect on the production of excess power. But, only weak RF fields were used in the Bockris and Cravens experiments, both of which used RF stimulation.

The appearance of RF in LENR electrochemical experiments still has the basic question of whether or not the high frequencies reflect the occurrence of LENR (are fundamental), or are due to the power supply or its interaction with the cell (and, hence, are artifacts).

If RF is due to the occurrence of LENR in electrochemical experiments, does it also appear in the operation of LENR in gas loading experiments?

Needed Work

Technical details involved in the measurement of RF within the circuits of electrochemical cells need more experimental and analytical attention.

These include the method used to pick up the high frequency variations and the possible non-linearity of frequency down converters.

The potential synergism between the application of magnetic fields to cells and the effects of appearance of RF needs more experimentation.

Variations in the intensities of the peaks that appear in RF spectra with the electrochemical current should be determined.

If a cell, which is giving both excess power and RF, is poisoned to stop LENR, what would happen to the RF?

The levels of the white noise in measured RF spectra from LENR experiments should be measured precisely to see if it increases during LENR.

The 1/f noise measured in some ENEA experiments might contain information, so they should be analyzed.



Cold nuclear fusion in the earth's crust

Tarasenko Gennadiy Vladimirovich

Kazakhstan, Aktau



CONCRETIONS MODEL OF PLANET EARTH ON THE THEORY TARASENKO

The structure of the Earth: the core of the plasma-ball, rotation of 20-40 m / sec, the mantle 1-10 m / year, the lithosphere-2-16 cm / year. The rotation of the nucleus and leads to the rotation of the geosphere and their slip under each other, which leads to a dynamo effect. The accumulation of energy occurs in the mantle and lithosphere, serving as natural Electrical capacitors



VOLCANIC ERUPTIONS AND THE ORIGIN OF TORNADOES IS ALSO ASSOCIATED WITH THE EARTH'S ELECTRICITY. IN VOLCANOES OCCUR VOLCANIC BOMBS-BALL CONCRETIONS



MINI-PLANET EARTH. THERE ARE CLEARLY SEEN GEOSPHERE, WHICH ARE INSERTED INTO EACH OTHER. THEIR ORIGIN IS CONNECTED WITH THE ROTATION OF THE LINEAR AND FIREBALLS IN OIL-GAS-WATER-CONTENT RESERVOIR.

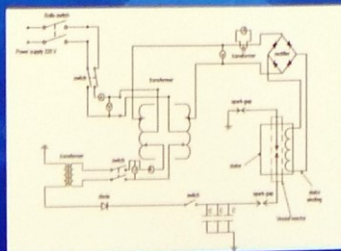
The percentage of iron oxide nodules in the center - 90%, on the surface - 6-7%. This is one of the proofs of education spherical nodules and the planet Earth from the cold plasma due to electric explosion. The plasma is in itself contain organic debris and living cells or bacteria, which leads to life on planet Earth in the solar system and probably in other Galaktikahlitosfere that serve as natural Electrical capacitors



IT CAN BE CLEARLY SEEN THE SPHERICAL STRUCTURE OF THE NODULES, AND THEY DIFFER IN CHEMICAL COMPOSITION AND CAN BE SEEN VISUALLY.

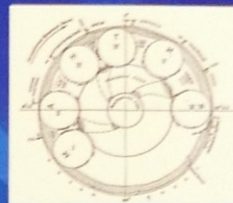


This electrical schematic diagram of the research to date, before this scheme is high-voltage laboratory was used to determine the gust of high voltage cables, where the ball air discharger.



THE DEVICE OF PLANET EARTH.

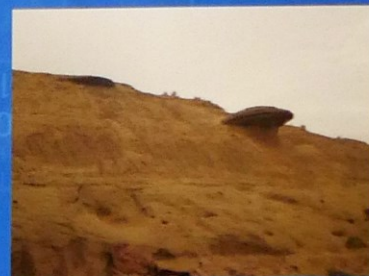
During the absorption of rock are ground into powder (flour) due to the effect of millstones, which forms due to the difference speed plates (layers) and the geosphere. Deep fluids are dissolved and carried over long distances different solubility of rocks (clay, limestone, etc.), forming, thus, the basal bundles, in which migration occurs and fluids. At the same time basal bundles and serve to lubricate the movement of Geosphere and layers (plates, slices). During the movement of beds is razmulchivanie and dissolution of rocks (clay, mudstone, limestone) and volcanic rocks remain in place, thus forming a collector.



TERRESTRIAL ELECTRICITY IN THE PHYSICAL SENSE ASSOCIATED WITH THE TESLA TRANSFORMER, LIGHTNING WHICH CAN SPREAD FOR MILES, AS UNDER THE EARTH AND THE ATMOSPHERE.



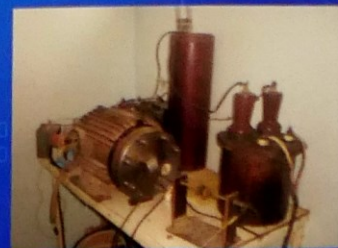
FLYING SAUCERS, ONE TYPE OF NODULE MANGYSHLAK.



Lab fireball. Shooting in the dark room. St. Petersburg Institute of Nuclear Physics. BP Konstantinova RAN, Gatchina. Research conducts Gennady Shabanov, his studies were transmitted by NTV and published in many scientific journals.



also decided to create the same ball lightning, but in accordance with the massive ground and geological conditions in certain temperature and pressure conditions.





Atomistic Simulations of Discrete Breathers in Crystals and Clusters: a Bridge to Understanding LENR

V. Dubinko^a, D. Terentyev^b, S. Dmitriev^c, F. Piazza^d

E-mail: vdubinko@hotmail.com

^aNSC Kharkov Institute of Physics and Technology, Ukraine

^bStructural Materials Modelling and Microstructure, SCK-CEN, Boeretang 200, 2400 Mol, Belgium

^cInstitute for Metals Superplasticity Problems RAS, Russia

^dUniversité d'Orléans and Centre de Biophysique Moléculaire, France

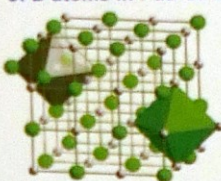
SolitonLab.com



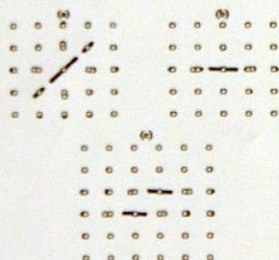
Introduction

One of the main puzzles of LENR is how effectively the electron charge transfer reaction or the adsorption/desorption reaction couple energy into modes of lattice vibration appropriate to stimulate nuclear reaction. The main argument here is that in crystals with sufficient anharmonicity, a special kind of lattice vibrations, namely, **discrete breathers (DBs)** a.k.a. intrinsic localized modes, can be excited either thermally or by external triggering, in which the amplitude of atomic oscillations greatly exceeds that of harmonic oscillations (phonons) [1]. Due to the crystal anharmonicity, the frequency of atomic oscillations increase or decrease with increasing amplitude so that the DB frequency lies outside the phonon frequency band, which explains the weak DB coupling with phonons and, consequently, their robustness at elevated temperatures. Due to the large mass difference between H/D and the metal atoms, there is a gap in phonon spectrum of metal-hydride crystals, in which so called '**gap DBs**' arise in the H/D sub-lattice resulting in time-periodic modulation of spacing between adjacent H/D atoms and between them and metal atoms. We show that at specific DB amplitudes, they may cause parametric formation of **Coherent Correlated States (CCS)**, which dramatically enhance Tunneling Coefficient for fusion of D-D or Metal-H/D atoms. We demonstrate a parity between critical DB-induced frequencies and the resonance frequencies of the Terahertz laser LENR stimulation.

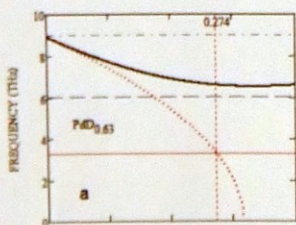
Breather-induced time-periodic action on the potential well of D atoms in PdD at various D loading ratios



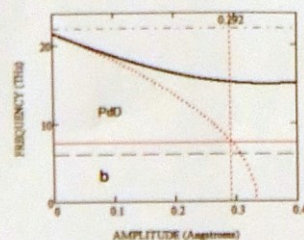
The rock-salt structure of PdD, in which each of the two atom types forms a separate face-centered cubic lattice, with the two lattices interpenetrating. Heavy (light) atoms are shown by large green (small grey) circles.



Stroboscopic pictures showing motion of atoms for the DBs of three types: (a) $[110]_1$, (b) $[100]_1$, and (c) $[100]_2$, where figures in brackets describe DB polarization and the subscript indicates the number of the atoms oscillating with large amplitude. Heavy (light) atoms are shown by open (filled) circles. In panels (a) and (b) displacements of the atoms are multiplied by factor 7, and in panel (c) by factor 5 [Khadeeva, Dmitriev (2010)].



DB frequency Ω (solid curves) and eigenfrequency ω_0 (dot) of the potential wells as functions of the DB<110> amplitudes, A_{DB} , for different force 'constants', γ_1, γ_2 assumed for $\text{PdD}_{0.63}$ (a) and PdD (b) lattices. <110> are the close-packed D-D directions; dashed blue lines show phonon gap edges [2].

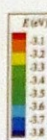


$$\Omega(A_{DB}) = \sqrt{\alpha + \frac{3}{4}\beta A_{DB}^2}; \quad \omega_0(A_{DB}) = \sqrt{\alpha}$$

$$\alpha = \frac{2\gamma_1(A_{DB})}{m}; \quad \beta = \frac{2\gamma_2(A_{DB})}{m}$$

— DB frequency
... Eigenfrequency
--- Upper acoustic phonon edge
--- Lower optic phonon edge
--- Resonance frequency

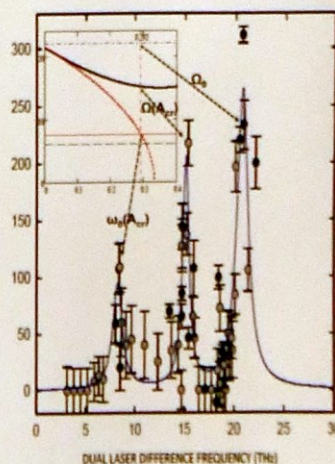
Site selectiveness of DB formation in the presence of spatial disorder.



Atomic configuration of a Ni nanoparticle of 2899 atoms at $T = 1000$ K. The atoms are colored based on the potential energy and their size is proportional to Debye-Waller factor. Both potential energy and size are time averaged over a 130 ps time window, corresponding to the time interval during which the strings show maximum length [Zhang, Douglas (2013)].

Breather-induced LENR energy production

Experiment vs. Model [2]: $D + D \rightarrow {}^4\text{He} + 23.8 \text{ MeV}_{\text{fusion}}$



Excess power, P_{D-D} (mW) under joint action of two low-power laser beams with variable beat frequency on the surface of the Pd cathode during the electrolysis in heavy water [Hagelstein et al (2010)]. The inset shows parity between critical DB-induced frequencies: $\Omega_0, \Omega(A_{DB}), \omega_0(A_{DB})$ and the resonance laser frequencies designated by dashed arrows.

$$P_{D-D} = K_{DB}^J(A_{DB}, T, J) \times 23.8 \text{ MeV}_{\text{fusion}}$$

[1] V. Dubinko, J. Condensed Matter Nucl. Sci., **14**, 87 (2014)
[2] V. Dubinko (2015) <http://arxiv.org/abs/1503.09119>

Conclusions/outlook

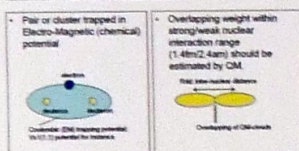
- The present model explains all the salient LENR requirements: (i) high loading of D within the Pd lattice as preconditioning needed to prepare PdD crystallites with appropriate density of states (DOS), and (ii) the triggering by D flux or electric current, which facilitates the DB creation by the input energy transformed into the lattice vibrations.
- The proposed mechanism of CCS formation near the gap DBs requires sufficiently broad phonon gap that is not observed below the critical D loading ~ 0.83 examined so far. An alternative mechanism of the DB-induced CCS formation may involve high frequency (hard type) DBs, manifested by the peak above the phonon spectrum in NaCl type crystals.
- Atomistic modeling of DBs of various types in nanoclusters of hydrides/deuterides is an important outstanding problem since it may offer new ways of engineering the nuclear active environment.

Fundamental of Rate Theory for CMNS

Akito Takahashi
Technova Inc. and Osaka University
(Presentation slides at ICCF19, Padua Italy, April 12-18, 2015)

2) Fusion rate theory for trapped D(H) particles^{4,6}

Trapped particles in EM-potential make nuclear reactions by QM superposition



Technova Inc. Technova

No good to use the rate theory of free particle collision

- Despite the importance of reaction rate estimation in modeled CMNS theories, only a few authors have treated nuclear reaction rates properly.
- Some theories have borrowed rate formulas of two body collision process which is the case of nuclear reactions for the random free particle motion as in plasma and gas phase or beam-target interactions.

Technova Inc. Technova

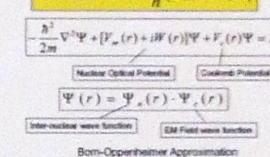
CMNR (condensed matter nuclear reactions) needs to use rate estimation for trapped state D(H)s

- Intrinsically the CMNS nuclear reactions should happen between trapped particles of proton and deuteron (H or D) in negative potential wells organized by the ordering of condensed matter with periodic lattice, mesoscopic nano-particle and surface fractal conditions.
- Such trapped D(H)-particles should have finite lifetime or existing time in the negative potential well and are keeping mutual inter-nuclear distances for finite time-intervals before fusion reactions.

Technova Inc. Technova

Fusion Rate Formula by Fermi's Golden Rule

$$\langle \text{FusionRate} \rangle = \frac{2}{\hbar} \langle \Psi_f | W(r) | \Psi_i \rangle \langle \Psi_i | W(r) | \Psi_f \rangle$$



Technova Inc. Technova

Fusion Rate Formula by Fermi's First Golden Rule with Born-Oppenheimer Approximation

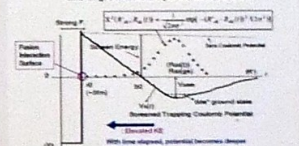
$$\langle \text{FusionRate} \rangle = \frac{2}{\hbar} \langle \Psi_f | W(r) | \Psi_i \rangle \langle \Psi_i | W(r) | \Psi_f \rangle$$

Inter-nuclear fusion rate Barrier Factor
 $\langle \Psi_f | W(r) | \Psi_i \rangle \langle \Psi_i | W(r) | \Psi_f \rangle$
 $\Psi_f = 4\pi r^2 \Psi_n$
Effective Volume of Nuclear Strong (Weak) Interaction Domain
 λ_D Complete wave length of plas (1.4 fm) (weak boson: 2.5 fm)
 R_0 Radius of interaction surface of strong (weak) force exchange

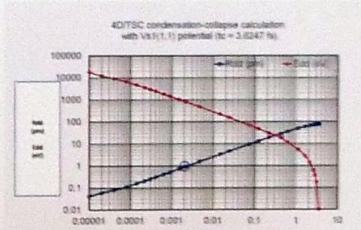
Technova Inc. Technova

Fusion rate should be estimated time-dependently, e.g. for TSC-like Condensation: No Stable State, but into sub-pm entity

Adiabatic Potential for Molecule dde* and its ground state squared wave function



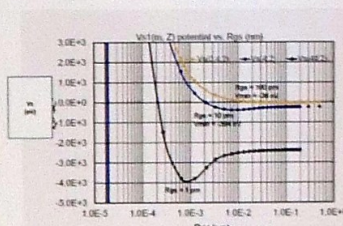
Technova Inc. Technova



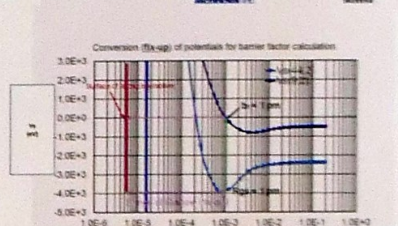
Technova Inc. Technova

Sur-Rad (pm)	Pos. 2D Barrier Factor	Pos. 4D Barrier Factor
0.020	4.46E-2	1.95E-1
0.042	1.94E-2	1.17E-4
0.107	1.43E-3	2.95E-6
0.206	1.70E-3	1.12E-9
0.432	9.46E-7	2.16E-31
0.867 (1.44)	1.01E-7	1.06E-38
2.03	6.66E-11	6.46E-52
2.66	4.95E-13	4.70E-59
4.42	9.76E-22	8.76E-64
10.3	2.04E-32	4.67E-64
22.4 (40.15, 2)	1.16E-44	1.69E-67
74.1 (102)	1.90E-61	1.69E-67

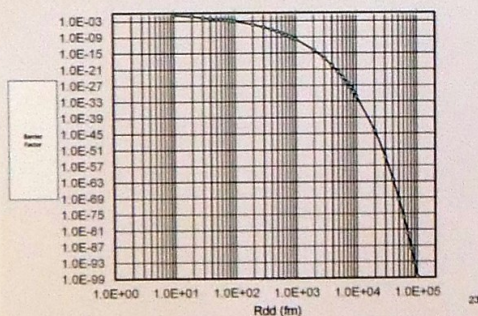
Technova Inc. Technova



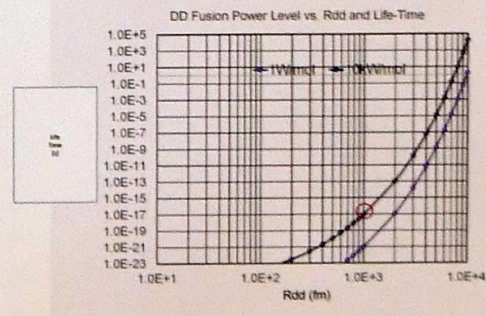
Technova Inc. Technova



Technova Inc. Technova



Technova Inc. Technova



Technova Inc. Technova

Collision Rate Formula UNDERESTIMATES fusion rate of steady molecule/cluster

Cluster	Rdd = Rgs (pm)	Barrier Factor	Steady Cluster d-d Fusion Rate (1/s)	Steady Cluster 4d Fusion Rate (1/s)	Fusion Rate for d-d collision formula (1/s)
D2	74.1	1.0E-85	2.4E-66	3.6E-86	4.0E-72*
dde*(2,2)	21.8	1.3E-46	3.2E-27	1.0E-46	(1.0E-31)*
ddp	0.805	1.0E-9	2.4E+10	1.5E-9	(1.0E+4)*
4D/TSC-minimum	0.021	1.98E-3	3.7E+20		

* Frequency of d-d pair oscillation by OM-Langevin calculation was considered.

Technova Inc. Technova

Summary

- For CMNR rate formulas, we need to take life-time of D(H)s in chemical trapping potential well into account properly.
- We cannot use formulas for two-body collision theory for CMNR, as it drastically underestimates fusion rate.
- Fermi's first golden rule should be used for rate formulas.
- Feasibly enhanced cluster fusions may happen only for collapse states of dynamic condensation: 4D/TSC, 6D/RDC, 8D/RDC for examples.
- Therefore, we need time-dependent fusion rate calculation to estimate real fusion yield per D(H)-condensing-cluster formation.
- If inter-nuclear d-d distance for condensate becomes less than 1.0 pm, we can expect reaction rates with 'observed heat-power levels'.

Technova Inc. Technova

Theoretical Study on Transmutation Reactions

T. Toimela
Vaasa University of
Applied Sciences
tuomo.toimela@vamk.fi

1

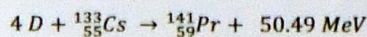
1. Aim of this study

- Explain the variation of the transmutation ability of different elements
- Increase the signal
- Restrict the class of possible explanations for the mechanism of LENR

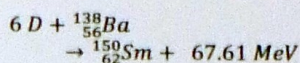
2

2. Basic question:

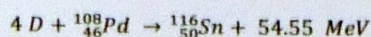
If there is a reaction:



and also:



then why not for example:



(or other Pd reactions)?

3

3. Assumptions:

- There is some kind of (unknown) mechanism that enhances the apparently small reaction rates
- Make any restrictive assumptions neither on the NAE nor on the mechanism except:
- Mechanism *itself* does not depend on the nuclear charge Z

4

4. Transition probability

The transition probability for a deuteron absorption by a nucleus (in the WKB approximation):

$$P_1 \sim e^{-\int_0^r 2\sqrt{\frac{2\alpha\mu cZ}{\hbar x}} dx} \sim e^{-4\sqrt{2\alpha\mu cZr/\hbar}}$$

α = the fine structure constant
 $\approx 1/137$

μ = the reduced mass

r = the distance between the deuteron and the nucleus

5

4. Transition probability, cont'd

The transition probability for four deuterons absorption by a nucleus (in the WKB approximation):

$$P_4 \sim e^{-16\sqrt{2\alpha\mu cZr/\hbar}}$$

Including also the charge potential of the electrons:

$$P_4 \sim e^{-8\int_0^r \sqrt{2\mu V(x)/\hbar^2} dx}$$

$$V(x) = \alpha c \hbar \times \frac{Z - \frac{4\pi x^3}{3} \rho_0 - \sum_i \int d^3x \rho_i(x)}{x}$$

6

5. How these transition rates can be increased?

The distance between the deuteron and the nucleus is important.

If an atom or a molecule (on the surface or below the surface) is either neutral or has an effective charge less than e, the distance between the deuteron and the nucleus shortens.

In that case the transition rate becomes larger than for the ionised host atoms in the lattice.

7

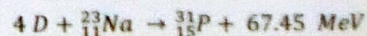
6. How this can be materialised?

- The base metal atoms on the surface will be oxidated and are then part of a neutral entity
- Especially this is true for the alkaline atoms on the surface, which consequently will have higher transmutation rates than the positively charged host metal atoms
- Also embedding neutral atoms or molecules below the surface

8

7. Predictions:

- 1) Larger rate by using Na instead of Sr or Cs. For example:



- 2) Large transmutation signal by embedding nonmetal impurity atoms in the lattice.

- 3) If the preparation of the Pd-complex will be done in a very pure N_2 atmosphere, the transmutation signal will decrease.

9

Study to Produce Strong Cube Texture Pd Foils Production



D.L. Knies, R. Cantwell, O. Dmitriyeva, G. Stanish, E. Goulet, S. Hamm and M. McConnell
Coolscence, LLC, Boulder, CO 80301
ICCF-19, Padua (Italy) 13-17 April 2015

Metal Retains Memory of the Degree of Prior Cold-Work

Motivation

After nearly three years, the production of over 300 cathodes, and 35,000+ hours of run time, Coolscence LLC has been unable to reproduce the excess heat effect. To improve our chances of seeing the effect, it was decided to take a step back and try to gain control of a number of specific material properties thought to play a crucial role^{1,2,3}:

- 1. Palladium foils with dominant <100> orientation
- 2. Approximately 100 μm mean grain size with well defined grain boundaries
- 3. Exceed D/Pd "Threshold" (deuterium concentration < 5 atom % with low current density "Easy Loading")
- 4. "Ideal" Surface (Surface structure with pronounced peaks in the Power Spectral Density Function between 10° and 10°)
- 5. High flux of deuterium across the cathode/electrolyte boundary

The primary goal was to establish a link between the metallographic treatment of pure palladium foils, so as to make it possible to predict deuterium loading behavior. In this paper, we highlight the impacts of deformation history and annealing temperature on the recovery/recrystallization of cold worked palladium foils. It is this history, that in turn controls both grain size and crystallographic texture. Subsequent chemical etching can then be used to reveal specific surface morphological features directly related to the underlying crystallographic texture. Elucidated are the minimum steps necessary to produce palladium foils with strong cube texture. While the above material properties may be crucial to excess heat production, we find no discernible relationship between a pure palladium foil's metallographic treatment and its ability to achieve the threshold deuterium concentration. Rather, it is the presence of promoter impurities on the surface that is the dominant predictor of a given foil's capability of meeting the threshold loading condition.

Rolling/Cold-Working - Annealing Foil Family Tree



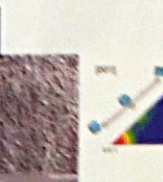
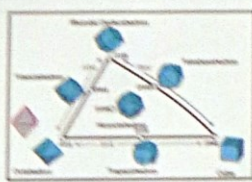
The deformation texture determines the recrystallization texture, which, in turn, determines the secondary recrystallization or growth texture.

Etching Reveals Surface Texture/Crystallography

Palladium Low-Index Single-Crystal Surfaces

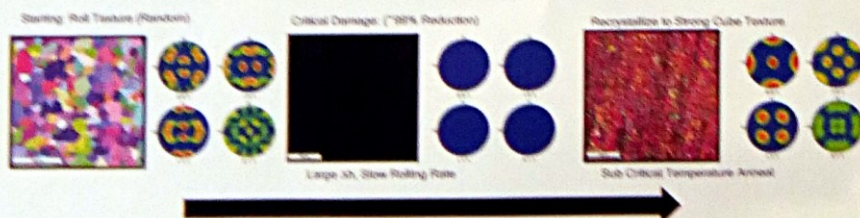
Etching Exposes Palladium Facets

EBSD Overlay

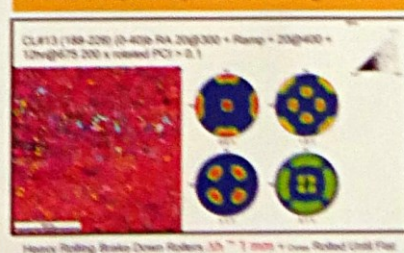


How to Make Strong Cube Textured Pd Foils

All traces of the original texture must be eliminated!



Must Develop Lot Dependent Annealing Protocol



Disconnect Between Loading and Metallurgy

Unintentional or Intentional **nanomolar (nM) promoters** are first order parameters

Summary



Select surface promoters near a monolayer in thickness are first order factors controlling the degree of loading of Pd foils; therefore, nM intentional or accidental additions must be controlled. Grain size, grain boundary grooving, annealing time and temperature, cracks formed along the (111) slip planes in the (011) slip directions, loading protocols (constant current, voltage control, and rate of change of either) are all second order effects at best. The real question at hand is whether it is even possible to load pure Pd in pure 100 mM LiOD electrolyte beyond the equilibrium pressure value of ~ 0.75 D/Pd ratio.

We have demonstrated how to control the crystallographic texture and grain size of palladium foils; however, we have not been able to identify a first order link between metallurgical treatment and loading. Subsequent analysis of more than 300 experiments has shown that surface promoters¹ are first order parameters predicting loading performance, and that as-rolled non?annealed foils perform similarly to annealed foils from a loading standpoint. See S. Hamm and O. Dmitriyeva presentations for more details on this topic. This finding does not rule out the potential importance of grain size, crystallographic texture, and grain boundary type to the production of excess heat from the deuterium-palladium system.

1. M. Knies, M. C. H. et al. New Hydrogen Energy Research at DOE in 100% Progress in New Hydrogen Energy, 1998, Lake Tahoe, Hokkaido, Japan. New Energy and Industrial Technology Development Organization, Tokyo Institute of Technology, Tokyo, Japan.

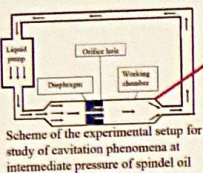
To Contact the Author: david@coolscence.com

Observation, simulation and investigation of undamped thermal waves in LENR-related problems

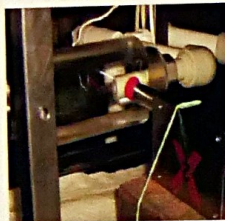
V.I.Vysotskii, A.O.Vasilenko: Kiev National Shevchenko University, Ukraine
A.A.Kornilova: Moscow State University, Russia

X-RAY GENERATION AT BUBBLE CAVITATION.

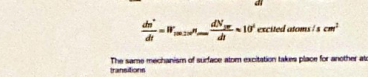
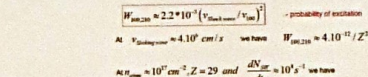
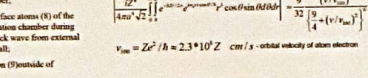
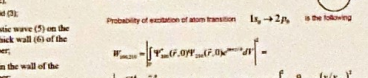
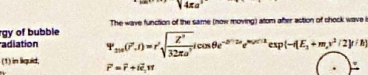
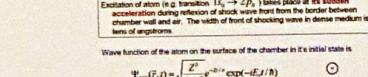
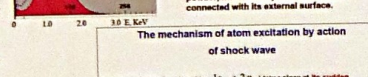
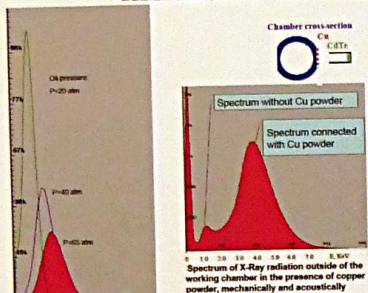
1). cavitation of machine oil.



X-Ray detector during radiation measurement in the cavitation regime



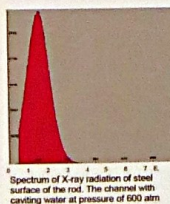
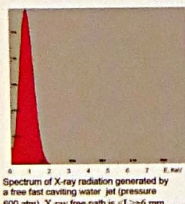
The change (shift) of spectra of X-ray radiation generated by the surface of cavitation chamber at stage-by-stage increases in oil pressure (left to right - 20, 40 and 65 atm).



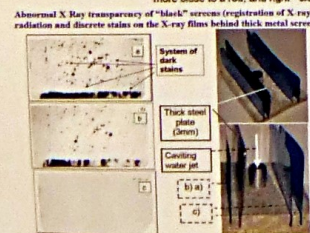
2. Generation of intensive x-ray radiation at free exit of the fast water jet from metal channel



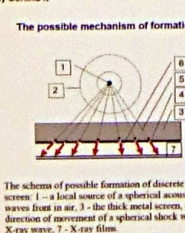
X-Ray radiation from rod with cavitating water jet



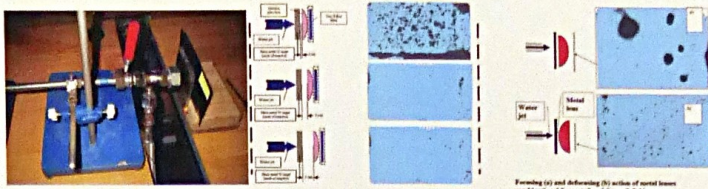
The image on two X-ray films situated without clearance in coaxial geometry around cylindrical rod with cavitating water jet on distance of 7 mm. The left film was situated more close to a rod, and right - closely behind it



Abnormal X-Ray transparency of "black" screens (registration of X-ray radiation and discrete stains on the X-ray films behind thick metal screen)



The scheme of possible formation of discrete stains on the X-ray films situated behind a thick screen: 1 - a local source of a spherical acoustic shock wave, 2 - fronts of X-ray and shock waves from air, 3 - the thick metal screen, 4 - local defect point on a screen backside, 5 - direction of movement of a spherical shock wave in screen volume, 6 - generated secondary X-ray wave, 7 - X-ray film.



3. Observation and investigation of undamped thermal waves

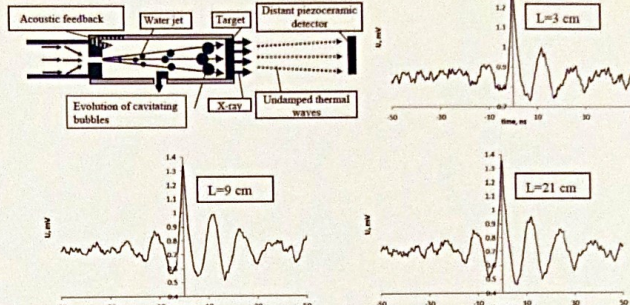


Fig.6. Experimental setup for study of X-ray and undamped thermal waves at cavitation of fast water jet and high-frequency signals registered in air at different distances L.

During water cavitation experiments simultaneously with the registration of X-rays [1-3] we have registered previously unknown undamped thermal waves in air. Fig. shows the experimental setup and the view of signals registered in air by broadband acoustic piezoelectric detector at different distances L from the outer surface of the target made of tungsten [4]. Elastic waves in the air beyond the metallic target were recorded by the wide-band acoustic receiver - a TsTS-19 (VA-500) piezoelectric 20 mm in diameter with a resonance frequency of 1 MHz. The receiver traveled along the facility axis in the distance range from 5 mm to 21 cm from the outer surface of the metallic target. Measurements were conducted with a step of 1 cm. The receiver during measurement was turned relative to the facility axis at angles of 0°, 20°, 90°, and 180°. The experiments were carried out with the use of a tungsten or molybdenum target.

Registration of the acoustic signal with a frequency of $\omega \approx 80...85 \text{ MHz}$ at distances $L = 3...20 \text{ cm}$ from the back side of the target is the paradox that can not be explained by of "standard" acoustics. The "standard" formula for absorption ($\delta \sim \omega^2$) of ultrasound has shown that at such frequency the coefficient of absorption in the air $\delta \approx 10^4 \text{ cm}^{-1}$ is very large, and the mean free path $\bar{L} \approx 1...2$ microns is very small! This result becomes still more surprising if the relative low resonance frequency of the used broadband acoustic detector (1 MHz, which is by 85 times less than the frequency of the recorded signal) is taken into account. This condition is evidence of a much lower recording efficiency, which is proportional to the Q factor of acoustic resonance in the detector. From this it is evident that the real amplitude of the signal in the distant place of the acoustic detector was very great. This paradox can be resolved if we assume that it is not "usual" acoustic wave but undamped thermal wave [5,6].

Existence of undamped thermal waves that can propagate without dissipation in environments with small time τ of local temperature relaxation was theoretically predicted in [5,6]. Such waves have a minimal characteristic eigen frequency $\omega_{\text{min}} \approx \pi / 2\tau$ and can be excited in environment under the influence of short heat pulses with duration $\Delta t < \tau$. In the case of finite time τ of local thermodynamic relaxation the heat transfer equation with delay has the following view

$$\frac{\partial T(x,t)}{\partial t} = G \frac{\partial^2 T(x,t)}{\partial x^2} \quad (1)$$

The solution of this equation is superposition of colliding thermal waves [5,6]

$$T(x,t) = A_{\text{ex}} \exp \left(-\kappa \frac{\cos \omega t}{\sqrt{1 + \sin \omega t}} x \right) \left[\exp \left(-\kappa \frac{\cos \omega t}{\sqrt{1 + \sin \omega t}} x \right) + B_{\text{ex}} \exp \left(-\kappa \frac{\cos \omega t}{\sqrt{1 + \sin \omega t}} x \right) \right] \cos \omega t \geq 0 \quad (2)$$

fundamentally different from the solution of "standard" heat equation without this delay

$$T(x,t) = A_{\text{ex}} \exp \left(-\kappa x \right) \exp \left\{ \left(\omega t - \kappa x \right) \right\} + B_{\text{ex}} \exp \left(\kappa x \right) \exp \left\{ \left(\omega t + \kappa x \right) \right\} \quad (3)$$

which determines the thermal waves with very strong damping $\delta = \kappa = \sqrt{\omega / 2G}$. For a system with relaxation the damping coefficient and phase velocities of colliding waves

$$\delta = \kappa \cos \omega t / \sqrt{1 + \sin \omega t}, \quad v_{\text{ph}} = \pm \sqrt{2G\omega / (1 + \sin \omega t)} \quad (4)$$

depend on the thermal diffusivity G , time delay τ and frequency ω of the wave [5,6]. The initial source of such wave is very short acoustic shock wave excited by cavitation on the inner surface of the target. Reflection of the wave from the outer surface forms: a) short acoustic pulse; b) short thermal pulse; c) short X-ray pulse with energy about 1.5-2 keV (see above) with duration $\Delta t < \tau \approx 10 \text{ ns}$ in the air. Soft X-rays, high-frequency components of "usual" acoustic waves and non-optimal components of thermal waves with $\omega \neq \omega_{\text{ex}}$ are absorbed quickly in the air. Under these conditions, signal transmission over long distances L is associated with the formation and propagation of undamped thermal wave with $\omega = \omega_{\text{ex}}$.

The theoretical results related to reasons and mechanism of undamped thermal wave formation have been investigated in detail in our papers [4-7]. They are in a good correlation with experimental results [4].

Conclusions

The experimental and theoretical results show that intense acoustic shock waves associated with cavitation processes are a source of intense X-ray emission outside the cavitation area. These experiments were repeated several times with different cavitation chambers. Every time we have observed identical effects - generation of controlled directed X-ray radiation. The process of X-ray generating is not connected with a specific temperature of the compressed microbubbles and is not the result of LENR but is the result of interaction of shock waves with surface atoms of the working chamber. The frequency (energy) of this X-ray radiation is dependent on the type of atoms on the surface and increase from $h\nu \approx 0.7...1.0 \text{ keV}$ for light (e.g., C, N, O) atoms to

$h\nu \approx 4...5 \text{ keV}$ for heavy (Pb) atoms.

Experiments with metal acoustic X-ray lenses confirm the possibility of focusing and spatial control of pulse soft X-rays radiation. The focal length of these lenses may be a few millimeters, which is fundamentally impossible in conventional X-ray optics. These lenses can be used to focusing a pulse X-ray radiation generated by particle beams (for example, at channeling).

Another result is connected with the detection and investigation of undamped high frequency thermal waves. The obtained results show that undamped temperature waves with a frequency determined by the specific parameters of the medium (composition, pressure, and temperature gases) may exist in media with temperature relaxation.

Each type of media is revealed to exhibit one or several frequencies (for very short thermal pulse) corresponding to the given waves. These frequencies are determined by the local thermal relaxation time τ . In metals, semiconductors and hot dense plasma, the values of τ are very small, and can be excited only by ultrashort thermal pulses with $\tau \leq 10^{-10}...10^{-11} \text{ s}$. In air under the normal conditions ($P \approx 1 \text{ atm}$, $T \approx 300 \text{ K}$) the relaxation time is about $\tau \approx 10 \text{ ns}$ and $\tau \approx 1/P\sqrt{T}$. To excite undamped wave it is necessary that there is a pulse heat disturbance of air media with a duration of $\Delta t \leq 10 \text{ ns}$, which is in good agreement with the known characteristics of duration of shock wave front at cavitation in water. Such undamped temperature waves may play the important role in the problems of heat exchange for the case of pulse thermal processes.

References

1. Kornilova, A.A., Vysotskii, V.I. et al., Generation of intense directional radiation during the fast motion of a liquid jet through a narrow dielectric channel. *Journal of Surface Investigation X-ray, Synchrotron and Neutron Techniques*, 2007, v. 1, 167-171.
2. Kornilova, A.A., Vysotskii, V.I. et al., Generation of X-rays at bubble cavitation in a fast liquid jet in dielectric channels. *Journal of Surface Investigation X-ray, Synchrotron and Neutron Techniques*, 2009, v. 3, 275-283.
3. Kornilova, A.A., Vysotskii, V.I. et al., Generation of intense X-rays during ejection of a fast water jet from a metal channel to atmosphere. *Journal of Surface Investigation X-ray, Synchrotron and Neutron Techniques*, 2010, v. 4, 1008-1017.
4. Vysotskii, V.I., Kornilova, A.A., Vasilenko, A.O., Tomak, V.I., Detection and investigation of undamped temperature waves excited under water-jet cavitation. *Journal of Surface Investigation X-ray, Synchrotron and Neutron Techniques*, 2014, v. 8, 1186-1192.
5. Vysotskii, V.I., Vasilenko, A.O., Vassilenko, V.B., Propagation of temperature waves in medium with internal thermal relaxation. *Bulletin of Taras Shevchenko National Univ. of Kyiv: Series Radiophysics*, 2013, № 1, 11-14.
6. Vysotskii, V.I., Vasilenko, A.O., Vassilenko, V.B., Generation and propagation of undamped temperature waves under pulse action on a target surface. *Journal of Surface Investigation X-ray, Synchrotron and Neutron Techniques*, 2014, v. 8, 367-373.
7. V.I.Vysotskii, A.A.Kornilova, A.O.Vasilenko. Observation and investigation of X-ray and thermal effects at cavitation. *Current Science*, 2015, v. 108, No. 8, p. 114-119

Unknown matter in Cold Fusion

Uwe P. Wettin

LCD-Solution s.a.r.l., France, wettin@lcd-solution.com

In science some rules exist for experiments. They should give everywhere, always and from everyone performed the same results. This is not the case in cold fusion experiments. This could be a hint, that the experiments are not closed. They are open und undefined in this way that a matter is flating through the experiment (or not), which has influence on the result.

On the one hand we have Ockham's razor, speaking against the idea of adding an additional parameter. On the other hand the astronomy is searching for matter, 19 times more than visible today. This could be a good opportunity to consider this matter.

The idea is first to prove by experiment, that this matter exists. And we need it not Far in the stars, but here on earth in our environment. This matter is mostly unknown and we have no conception of its behavior. One thing is sure: It should interact by balance weight, as it represents a matter with mass.

DEVICE spec

We need a device which detects changes of mass :

- Easy to use.
- Easy to replicate with standard electronic components.
- Low cost.
- Open source programming.
- Data logger writes datasets on SD card.
- Datasets to be handled with EXCEL or other spreadsheet applications.

Experiment setting

4 pressure sensors are placed under the 4 legs of a bed. In the bed a person stays for a sleep. This person activates the device and datasets of weight are logged every minute or every second for the next hours. After the person wakes up, he stops the data recording. The data is written on a SD-card and can be evaluated with PC softwaretools. Alternatively the person is sitting on a chair with the 4 pressure sensors under the legs of the chair. The person makes relaxation exercise or autogenic training.

Device realization

This example of a realization is based on an Arduino Microprocessor unit. There on top is a so called "Shield" that adapts a TFT display with integrated TouchScreen. This is the front end for handling the device funktions (start, stop, config, data display, calibration, ect.). 4 pressure sensors are dismounted from an bathroom scales. The only customized component is an additional shield with two integrated differential amplifiers. The amplifiers adapt the sensor signals from the 4 pressure sensors to the microprocessor inputs.

Components



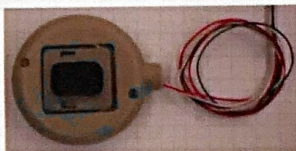
Arduino Mega 2560



Adapter Shield for Display, SC-Card (and later Diff.Amps)



TFT Display with TouchScreen and SC-Card connector



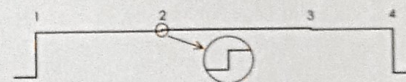
Pressure sensors



Altogether under chair

Measurement

Here are shown 3 important results for the device.



This is (1) start of measurement, (2) adding a weight of 30 gr, (3) taking away this weight, (4) end of measurement. This result prove that the device works precise.

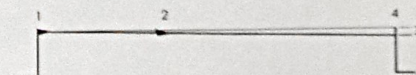
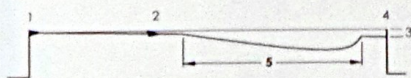


Diagram No.2: This diagram shows the result for a person in a bed: (1) start, (2) movement in bed results in waves in records, (3) shows loss of weight by transpiration and respiration over the time, as a delta between (1) and (4), (4) end of measurement. This diagram can be expected and explained by todays knowledge.

Diagramm No. 3



This diagram is similar to No.2. The difference is the shown in (5). Here is an anomaly which is not to be explained with normal knowledge.

As diagram No. 3 is claimed by K. Volkamer, this result should be investigated more precisely.

As the development of the device is not finished, it is desirable to get input from you to integrate your ideas into the device.

Uwe P. Wettin

wettin@lcd-solution.com

Padova, 13th avril 2015

(1) K. Volkamer Feinstofflichkeit erklärt Anomalien der Gravitationskonstanten und mehr, NEJ-Jahres 17 (2015), 26-32, 2015

The concept of propulsion with a LENR heat source for aircraft and ground application

Dmitry Baranov, and *Viktor Zatelepin
Private Laboratory "INLEAS", Russia,
Moscow, zvn707@yandex.ru

- Up to date, accumulated a large amount of data on the possibility of conversion: the internal energy of the working media in the heat in the so-called low-energy nuclear reactions (LENR). This method is characterized by a certain range of parameters of thermal energy and the design of the fuel units. There is a question of an optimal use of technology features LENR in existing concepts conversion of thermal energy into other forms of energy.
- Paper presents a concept of converting thermal energy generated by E-cat like fuel unit into mechanical energy in air jet propulsion engine. The concept is scalable over a wide range of power and thrust. Engine can be used in aviation and land application.

A bit speculation on theory. How LENR works in E-cat?

- All atoms consist of a nucleus with protons and neutrons and a cloud of electrons. The nucleus is positively charged and the electrons are negatively charged. The force of attraction between them is very strong.
- The high-speed motion of electrons in the nucleus is accompanied by the emission of gamma rays.
- $E = mc^2$ (1905) - E is energy, m is mass, c is speed of light.
- Small amount of mass can be converted into a large amount of energy. The mass of the nucleus is slightly greater than the sum of the masses of its constituent nucleons. This difference is called the mass defect.
- A gamma ray is a high-energy photon. It is emitted when a nucleus transitions from a higher energy state to a lower energy state.
- During the LENR process, a small amount of mass is converted into a large amount of energy. This energy is used to heat the working medium.
- The heat is used to drive a turbine, which is connected to a generator. The generator produces electricity, which is used to power the engine.
- The engine is a jet engine. It uses the heat to drive a compressor, which compresses the air. The compressed air is then heated by the LENR reactor. The hot air is then expanded through a turbine, which drives the compressor and the generator.
- The engine is a jet engine. It uses the heat to drive a compressor, which compresses the air. The compressed air is then heated by the LENR reactor. The hot air is then expanded through a turbine, which drives the compressor and the generator.

Schematic view of speed reactor



In accordance with the theory of Dr. Caplanovich

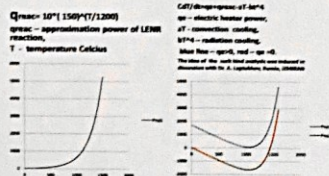
Positive and negative features of LENR in E-cat for energy conversion

- | | |
|---|---|
| Positive | Negative |
| <ul style="list-style-type: none"> High surface temperature of FU (1600-1700K) Low fuel consumption Easy to arrange convective heat transfer from FU to working media Air could be used as the working media of engine No chemical contamination | <ul style="list-style-type: none"> It is possible that sometimes high energy (~MeV) heavy particles are generated in accordance with the reaction [Dr. Leptukhov A.] $(e^-) + (H) \rightarrow (e^-) + (H) + \dots$ It depends on the contents of deuterium in the hydrogen. |

Important assumption on LENR in Ni + H₂ media

- It is supposed that generated heat depends on contents and thermodynamic parameters of fuel (may be depends on heat fluxes).
- It doesn't depend on external electric and magnet fields

Why continuous heating?



Single fuel unit parameters

Parameter	Value	Unit
Power	1.5	kW
Weight	1.5	kg
Volume	1.5	L
Dimensions	1.5	cm
Thrust	1.5	N
Useful thrust	1.5	N
Specific weight	1.5	N/kg
Specific volume	1.5	L/kg
Specific thrust	1.5	N/kg
Specific power	1.5	W/kg

Recuperation and control

$$Q_{rec} = (Q_{max} - Q_{min}) \cdot \eta_{rec}$$

Q_{max} - heat capacity of fuel unit;
Q_{min} - heat capacity of fuel unit;
η_{rec} - coefficient of recuperation

Q_{max} - heat capacity of fuel unit;
Q_{min} - heat capacity of fuel unit;
η_{rec} - coefficient of recuperation

Q_{max} - heat capacity of fuel unit;
Q_{min} - heat capacity of fuel unit;
η_{rec} - coefficient of recuperation

Q_{max} - heat capacity of fuel unit;
Q_{min} - heat capacity of fuel unit;
η_{rec} - coefficient of recuperation

Q_{max} - heat capacity of fuel unit;
Q_{min} - heat capacity of fuel unit;
η_{rec} - coefficient of recuperation

Q_{max} - heat capacity of fuel unit;
Q_{min} - heat capacity of fuel unit;
η_{rec} - coefficient of recuperation

Q_{max} - heat capacity of fuel unit;
Q_{min} - heat capacity of fuel unit;
η_{rec} - coefficient of recuperation

Q_{max} - heat capacity of fuel unit;
Q_{min} - heat capacity of fuel unit;
η_{rec} - coefficient of recuperation

Q_{max} - heat capacity of fuel unit;
Q_{min} - heat capacity of fuel unit;
η_{rec} - coefficient of recuperation

Q_{max} - heat capacity of fuel unit;
Q_{min} - heat capacity of fuel unit;
η_{rec} - coefficient of recuperation

Q_{max} - heat capacity of fuel unit;
Q_{min} - heat capacity of fuel unit;
η_{rec} - coefficient of recuperation

Q_{max} - heat capacity of fuel unit;
Q_{min} - heat capacity of fuel unit;
η_{rec} - coefficient of recuperation

Q_{max} - heat capacity of fuel unit;
Q_{min} - heat capacity of fuel unit;
η_{rec} - coefficient of recuperation

Q_{max} - heat capacity of fuel unit;
Q_{min} - heat capacity of fuel unit;
η_{rec} - coefficient of recuperation

Q_{max} - heat capacity of fuel unit;
Q_{min} - heat capacity of fuel unit;
η_{rec} - coefficient of recuperation

Q_{max} - heat capacity of fuel unit;
Q_{min} - heat capacity of fuel unit;
η_{rec} - coefficient of recuperation

Q_{max} - heat capacity of fuel unit;
Q_{min} - heat capacity of fuel unit;
η_{rec} - coefficient of recuperation

Q_{max} - heat capacity of fuel unit;
Q_{min} - heat capacity of fuel unit;
η_{rec} - coefficient of recuperation

Q_{max} - heat capacity of fuel unit;
Q_{min} - heat capacity of fuel unit;
η_{rec} - coefficient of recuperation

Q_{max} - heat capacity of fuel unit;
Q_{min} - heat capacity of fuel unit;
η_{rec} - coefficient of recuperation

Q_{max} - heat capacity of fuel unit;
Q_{min} - heat capacity of fuel unit;
η_{rec} - coefficient of recuperation

Q_{max} - heat capacity of fuel unit;
Q_{min} - heat capacity of fuel unit;
η_{rec} - coefficient of recuperation

Q_{max} - heat capacity of fuel unit;
Q_{min} - heat capacity of fuel unit;
η_{rec} - coefficient of recuperation

Q_{max} - heat capacity of fuel unit;
Q_{min} - heat capacity of fuel unit;
η_{rec} - coefficient of recuperation

Q_{max} - heat capacity of fuel unit;
Q_{min} - heat capacity of fuel unit;
η_{rec} - coefficient of recuperation

Q_{max} - heat capacity of fuel unit;
Q_{min} - heat capacity of fuel unit;
η_{rec} - coefficient of recuperation

Q_{max} - heat capacity of fuel unit;
Q_{min} - heat capacity of fuel unit;
η_{rec} - coefficient of recuperation

Q_{max} - heat capacity of fuel unit;
Q_{min} - heat capacity of fuel unit;
η_{rec} - coefficient of recuperation

Q_{max} - heat capacity of fuel unit;
Q_{min} - heat capacity of fuel unit;
η_{rec} - coefficient of recuperation

Q_{max} - heat capacity of fuel unit;
Q_{min} - heat capacity of fuel unit;
η_{rec} - coefficient of recuperation

Q_{max} - heat capacity of fuel unit;
Q_{min} - heat capacity of fuel unit;
η_{rec} - coefficient of recuperation

Q_{max} - heat capacity of fuel unit;
Q_{min} - heat capacity of fuel unit;
η_{rec} - coefficient of recuperation

Q_{max} - heat capacity of fuel unit;
Q_{min} - heat capacity of fuel unit;
η_{rec} - coefficient of recuperation

Q_{max} - heat capacity of fuel unit;
Q_{min} - heat capacity of fuel unit;
η_{rec} - coefficient of recuperation

Q_{max} - heat capacity of fuel unit;
Q_{min} - heat capacity of fuel unit;
η_{rec} - coefficient of recuperation

Q_{max} - heat capacity of fuel unit;
Q_{min} - heat capacity of fuel unit;
η_{rec} - coefficient of recuperation

Q_{max} - heat capacity of fuel unit;
Q_{min} - heat capacity of fuel unit;
η_{rec} - coefficient of recuperation

Q_{max} - heat capacity of fuel unit;
Q_{min} - heat capacity of fuel unit;
η_{rec} - coefficient of recuperation

Q_{max} - heat capacity of fuel unit;
Q_{min} - heat capacity of fuel unit;
η_{rec} - coefficient of recuperation

Q_{max} - heat capacity of fuel unit;
Q_{min} - heat capacity of fuel unit;
η_{rec} - coefficient of recuperation

Q_{max} - heat capacity of fuel unit;
Q_{min} - heat capacity of fuel unit;
η_{rec} - coefficient of recuperation

Q_{max} - heat capacity of fuel unit;
Q_{min} - heat capacity of fuel unit;
η_{rec} - coefficient of recuperation

Q_{max} - heat capacity of fuel unit;
Q_{min} - heat capacity of fuel unit;
η_{rec} - coefficient of recuperation

Q_{max} - heat capacity of fuel unit;
Q_{min} - heat capacity of fuel unit;
η_{rec} - coefficient of recuperation

Q_{max} - heat capacity of fuel unit;
Q_{min} - heat capacity of fuel unit;
η_{rec} - coefficient of recuperation

Q_{max} - heat capacity of fuel unit;
Q_{min} - heat capacity of fuel unit;
η_{rec} - coefficient of recuperation

Q_{max} - heat capacity of fuel unit;
Q_{min} - heat capacity of fuel unit;
η_{rec} - coefficient of recuperation

Q_{max} - heat capacity of fuel unit;
Q_{min} - heat capacity of fuel unit;
η_{rec} - coefficient of recuperation

Q_{max} - heat capacity of fuel unit;
Q_{min} - heat capacity of fuel unit;
η_{rec} - coefficient of recuperation

Q_{max} - heat capacity of fuel unit;
Q_{min} - heat capacity of fuel unit;
η_{rec} - coefficient of recuperation

Q_{max} - heat capacity of fuel unit;
Q_{min} - heat capacity of fuel unit;
η_{rec} - coefficient of recuperation

Q_{max} - heat capacity of fuel unit;
Q_{min} - heat capacity of fuel unit;
η_{rec} - coefficient of recuperation

Q_{max} - heat capacity of fuel unit;
Q_{min} - heat capacity of fuel unit;
η_{rec} - coefficient of recuperation

Q_{max} - heat capacity of fuel unit;
Q_{min} - heat capacity of fuel unit;
η_{rec} - coefficient of recuperation

Q_{max} - heat capacity of fuel unit;
Q_{min} - heat capacity of fuel unit;
η_{rec} - coefficient of recuperation

Q_{max} - heat capacity of fuel unit;
Q_{min} - heat capacity of fuel unit;
η_{rec} - coefficient of recuperation

Q_{max} - heat capacity of fuel unit;
Q_{min} - heat capacity of fuel unit;
η_{rec} - coefficient of recuperation

Q_{max} - heat capacity of fuel unit;
Q_{min} - heat capacity of fuel unit;
η_{rec} - coefficient of recuperation

Q_{max} - heat capacity of fuel unit;
Q_{min} - heat capacity of fuel unit;
η_{rec} - coefficient of recuperation

Q_{max} - heat capacity of fuel unit;
Q_{min} - heat capacity of fuel unit;
η_{rec} - coefficient of recuperation

Q_{max} - heat capacity of fuel unit;
Q_{min} - heat capacity of fuel unit;
η_{rec} - coefficient of recuperation

Q_{max} - heat capacity of fuel unit;
Q_{min} - heat capacity of fuel unit;
η_{rec} - coefficient of recuperation

Q_{max} - heat capacity of fuel unit;
Q_{min} - heat capacity of fuel unit;
η_{rec} - coefficient of recuperation

Q_{max} - heat capacity of fuel unit;
Q_{min} - heat capacity of fuel unit;
η_{rec} - coefficient of recuperation

Q_{max} - heat capacity of fuel unit;
Q_{min} - heat capacity of fuel unit;
η_{rec} - coefficient of recuperation

Q_{max} - heat capacity of fuel unit;
Q_{min} - heat capacity of fuel unit;
η_{rec} - coefficient of recuperation

Q_{max} - heat capacity of fuel unit;
Q_{min} - heat capacity of fuel unit;
η_{rec} - coefficient of recuperation

Q_{max} - heat capacity of fuel unit;
Q_{min} - heat capacity of fuel unit;
η_{rec} - coefficient of recuperation

Q_{max} - heat capacity of fuel unit;
Q_{min} - heat capacity of fuel unit;
η_{rec} - coefficient of recuperation

Q_{max} - heat capacity of fuel unit;
Q_{min} - heat capacity of fuel unit;
η_{rec} - coefficient of recuperation

Q_{max} - heat capacity of fuel unit;
Q_{min} - heat capacity of fuel unit;
η_{rec} - coefficient of recuperation

Q_{max} - heat capacity of fuel unit;
Q_{min} - heat capacity of fuel unit;
η_{rec} - coefficient of recuperation

Q_{max} - heat capacity of fuel unit;
Q_{min} - heat capacity of fuel unit;
η_{rec} - coefficient of recuperation

Q_{max} - heat capacity of fuel unit;
Q_{min} - heat capacity of fuel unit;
η_{rec} - coefficient of recuperation

Q_{max} - heat capacity of fuel unit;
Q_{min} - heat capacity of fuel unit;
η_{rec} - coefficient of recuperation

Q_{max} - heat capacity of fuel unit;
Q_{min} - heat capacity of fuel unit;
η_{rec} - coefficient of recuperation

Q_{max} - heat capacity of fuel unit;
Q_{min} - heat capacity of fuel unit;
η_{rec} - coefficient of recuperation

Q_{max} - heat capacity of fuel unit;
Q_{min} - heat capacity of fuel unit;
η_{rec} - coefficient of recuperation

Q_{max} - heat capacity of fuel unit;
Q_{min} - heat capacity of fuel unit;
η_{rec} - coefficient of recuperation

Q_{max} - heat capacity of fuel unit;
Q_{min} - heat capacity of fuel unit;
η_{rec} - coefficient of recuperation

Q_{max} - heat capacity of fuel unit;
Q_{min} - heat capacity of fuel unit;
η_{rec} - coefficient of recuperation

Q_{max} - heat capacity of fuel unit;
Q_{min} - heat capacity of fuel unit;
η_{rec} - coefficient of recuperation

Q_{max} - heat capacity of fuel unit;
Q_{min} - heat capacity of fuel unit;
η_{rec} - coefficient of recuperation

Q_{max} - heat capacity of fuel unit;
Q_{min} - heat capacity of fuel unit;
η_{rec} - coefficient of recuperation

Q_{max} - heat capacity of fuel unit;
Q_{min} - heat capacity of fuel unit;
η_{rec} - coefficient of recuperation

Q_{max} - heat capacity of fuel unit;
Q_{min} - heat capacity of fuel unit;
η_{rec} - coefficient of recuperation

Q_{max} - heat capacity of fuel unit;
Q_{min} - heat capacity of fuel unit;
η_{rec} - coefficient of recuperation

Q_{max} - heat capacity of fuel unit;
Q_{min} - heat capacity of fuel unit;
η_{rec} - coefficient of recuperation

Q_{max} - heat capacity of fuel unit;
Q_{min} - heat capacity of fuel unit;
η_{rec} - coefficient of recuperation

Q_{max} - heat capacity of fuel unit;
Q_{min} - heat capacity of fuel unit;
η_{rec} - coefficient of recuperation

Q_{max} - heat capacity of fuel unit;
Q_{min} - heat capacity of fuel unit;
η_{rec} - coefficient of recuperation

Q_{max} - heat capacity of fuel unit;
Q_{min} - heat capacity of fuel unit;
η_{rec} - coefficient of recuperation

Q_{max} - heat capacity of fuel unit;
Q_{min} - heat capacity of fuel unit;
η_{rec} - coefficient of recuperation

Q_{max} - heat capacity of fuel unit;
Q_{min} - heat capacity of fuel unit;
η_{rec} - coefficient of recuperation

Q_{max} - heat capacity of fuel unit;
Q_{min} - heat capacity of fuel unit;
η_{rec} - coefficient of recuperation

Q_{max} - heat capacity of fuel unit;
Q_{min} - heat capacity of fuel unit;
η_{rec} - coefficient of recuperation

Q_{max} - heat capacity of fuel unit;
Q_{min} - heat capacity of fuel unit;
η_{rec} - coefficient of recuperation

Q_{max} - heat capacity of fuel unit;
Q_{min} - heat capacity of fuel unit;
η_{rec} - coefficient of recuperation

Q_{max} - heat capacity of fuel unit;
Q_{min} - heat capacity of fuel unit;
η_{rec} - coefficient of recuperation

Q_{max} - heat capacity of fuel unit;
Q_{min} - heat capacity of fuel unit;
η_{rec} - coefficient of recuperation

Q_{max} - heat capacity of fuel unit;
Q_{min} - heat capacity of fuel unit;
η_{rec} - coefficient of recuperation

Q_{max} - heat capacity of fuel unit;
Q_{min} - heat capacity of fuel unit;
η_{rec} - coefficient of recuperation

Q_{max} - heat capacity of fuel unit;
Q_{min} - heat capacity of fuel unit;
η_{rec} - coefficient of recuperation

Q_{max} - heat capacity of fuel unit;
Q_{min} - heat capacity of fuel unit;
η_{rec} - coefficient of recuperation

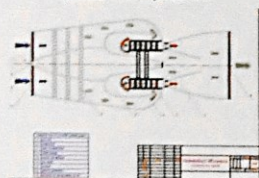
Q_{max} - heat capacity of fuel unit;
Q_{min} - heat capacity of fuel unit;
η_{rec} - coefficient of recuperation

Q_{max} - heat capacity of fuel unit;
Q_{min} - heat capacity of fuel unit;
η_{rec} - coefficient of recuperation

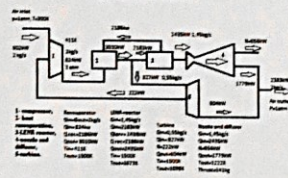
Q_{max} - heat capacity of fuel unit;
Q_{min} - heat capacity of fuel unit;
η_{rec} - coefficient of recuperation

Q_{max} - heat capacity of fuel unit;
Q_{min} - heat capacity of fuel unit;
η_{rec} - coefficient of recuperation

Schematic view of air turbojet engine powered by LENR



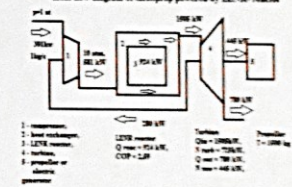
Heat flow diagram of turbojet engine powered by LENR-reactor



AIR-LENR TURBOJET ENGINE PARAMETERS

Power, kW	656
Compression ratio	3
Flow rate, kg/s	2
Weight, kg	69
Volume, L	127
Dimensions, cm	50
Thrust, kg	141
Useful thrust, kg	72
Specific weight	0.5
Specific volume, L/kg	0.3

Heat flow diagram of turbojet powered by LENR-reactor



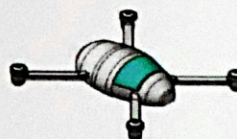
Turboprop powered by LENR-reactor

Power, kW	443
Compression ratio	10
Flow rate, kg/s	0.32
Weight, kg	49
Volume, L	135
Dimensions, cm	50
Thrust, kg	500
Useful thrust, kg	541
Specific weight	0.2
Specific volume, L/kg	0.3
Cabin weight, kg	100
Passenger weight, kg	351

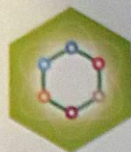
Quattrojet parameters

Total power, kW	2624
Cabin weight, kg	100
Engine weight, kg	276
Passengers weight, kg	187
Continuous flight, day	30

Quattrojet



SPECIAL ANNOUNCEMENT: CREATION OF THE FRENCH COLD FUSION SOCIETY



French Society for Condensed Matter Nuclear Science FSCMNS *

CATALYZING INTEREST IN
COLD FUSION IN FRANCE
AND FRENCH SPEAKING
COUNTRIES

The FSCMNS, created in 2014, is the French society dedicated to Cold Fusion and made by French LENR scientists.

Affiliated to the ISCMNS, our society intends to unite all the French speaking people interested in the field of Cold Fusion.

The GOAL is to provide a French channel for conferences, publications, discussions and collaborations on the field of CMNS.

It meets the Japanese, the Russian, the Italian and many other local groups that want to network, share and promote to governments and public institutions the crucial research we are pursuing altogether.

ICCF 19 – Padua (It.)

13 – 17 April 2015

Come and meet us at ICCF 19

Mathieu Valat
Jean-Paul Biberian
Joris van der Schot
Nicolas Armanet
Pierre Clauzon
David Fojt
Jean-Luc Paillet
Jacques Ruer

Henri de Lussigny
www.sfsnmc.org

CONTACT

SFSNMC
Mathieu Valat - President
7, rue de l'Eglise
30 190 St. Genès de Malgoirès FRANCE
Phone : +33 777 265 135
e-mail : info@sfsnmc.org

Want to be a member ?

The FSCMNS is looking for members, please contact us, flash the QR code, or visit our website:

www.sfsnmc.org



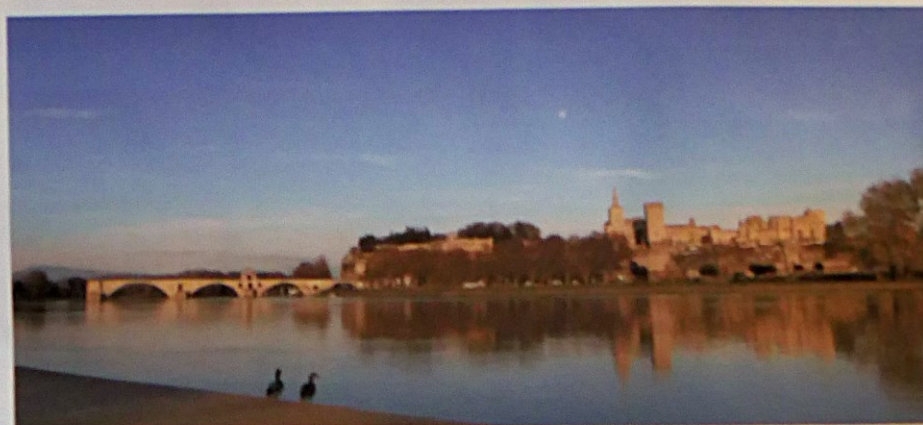
Want to participate to the first meeting ?

The FSCMNS is looking for contributions, please contact us:

info@sfsnmc.org

The first annual meeting will take place in September 2015 in Avignon

Please contact us for more informations



www.aweekinprovence.eu/location/



[illegible]

Early education

The present work is 13 years continuation of our previous works [7] on research of Anodic Plasma Electrolysis by Fukai's installation with Ervin model interpretation [12-17]. Experiment statement is defined by several important parameters: Δ remote cathodically and anodic diagnostics of

Apparently from Fig. 5A, an asquarium with an electrolytic cell are placed in a blue block for an extract of steams of alkali NaOH and additional coating of powerful installation (1-2). All diagnostics was spent in a case in immediate proximity to external glass of an asquarium. Viewing glass of a case has been executed from thick plexiglass in the thickness in 1 cm.

The main our analysis & calorimetric results are presented here.



Fig.4. The common view-2 of new experimental installation Facet.3 (N1 to E, 2013).

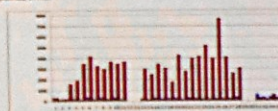


Fig. 5. The *Aspilota* account per minute (dark blue for the worker with the converter, blue for a control *Aspilota*).

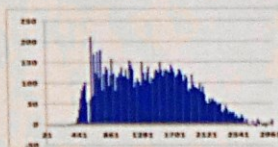


Fig. 10. Energy spectrum in PSD (GeV) with Teflon (CF₂)_n in front of scintillator in 10 cm from Anode Plasma center. Spectrum equal to β spectrum from F20 decay produced inside of Teflon from stable F19 isotope due to $F19(n, p)$, $301F19$ reaction.

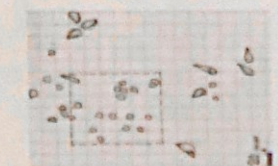


Fig. 11. Plots of \log viscosities in PMSO (C'W39) after 8 exposures to a series of plasma electrolysis in 1000 Torr at center. One from 20 each viscosities in PMSO (1.546 cP at 25°C).

process. An illustrative prototype of Faket-1 installation [10] is similar to our previous variant Faket-1 installation [8,9] with more distinctive

By new techniques are cooperation & digital fluorescence calorimeter and using of nuclear diagnostic presented by 2. Analyses control and control with Erden computer, 3. Radiometers, plastic & NaI scintillators, Photo couplers & PWT tracks diagnostic, 10 cosmic diagnostic is conducted outside of the glass equipment playing a role of an external source of thermally not cooling, the design and which materials are used without chemical (the 1. and 2.).



Fig. 1. The volume of environmental certification, Finland, 1990-2007.

- 1 - radius of the anode (mm)
- 2 - gold or tungsten anode (5 - 1 cm²)
- 3 - cathode - nickel or tin (5-10 cm²)
- 4 - glass separator with cooled water (7 l)
- 5 - glass case of an electrolyte bath (500 ml)
- 6 - external lead shield from standard modules
- 7 - internal (optional) lead protection of the gamma-ray detector
- 8 - the detector of gamma-radiation (standard black "Jensen" with crystal NaI (70x50x3 mm))

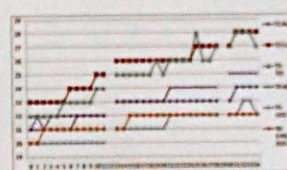


Fig. 6. Temperature dependence from working time (minutes) of plasma electrodeless (1–2 A, 0–600 V) for different samples in 5-corrat.

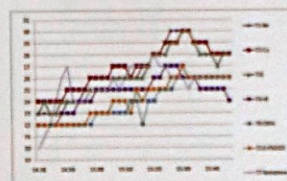


Fig. 7. Temperature dependence from working time (minutes) of glucose electrodes (1-2A, 3-400N) for different samples in 12-series (7, 12, 10).

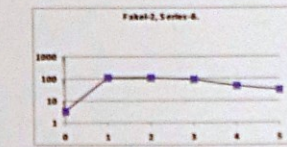


Fig. 12. The density dependence in PMSD (1/min) versus depth (mm) for C-240 blue ink after conversion to PMSD standard (1977) units. $n = 10$.

Table 1. The main and interactive effects, reported in Table 2, of age

No. lesions	Vascular composition	Microvessel size	Blood flow		M	A/M	Microvessel permeability (P _{av} × 10 ⁻³ a.u./mmHg)				
			Pre-ET	Post-ET			CG	CG	SE	SE	SE
FAH-0.2	FAH000000	51	52	126	100	0.0	0.0	0.0	0.0	0.0	0.0
FAH-0.2	FAH000000	51	124	100	100	0.0	0.0	0.0	0.0	0.0	0.0
FAH-1.1	FAH000000	14	15	100	100	0.0	0.0	0.0	0.0	0.0	0.0
FAH-1.2	FAH000000	15	124	100	100	0.0	0.0	0.0	0.0	0.0	0.0
FAH-1.2	FAH000000	10	12	100	100	0.0	0.0	0.0	0.0	0.0	0.0
FAH-1.5	FAH000000	56	124	100	100	0.0	0.0	0.0	0.0	0.0	0.0
FAH-1.5	FAH000000	10	12	100	100	0.0	0.0	0.0	0.0	0.0	0.0
FAH-1.5	FAH000000	16	124	100	100	0.0	0.0	0.0	0.0	0.0	0.0

In Faked-DBSTs, results are based on results from other studies. It is important to note that the results of the studies are not presented in Table 2.1, but are presented in Table 2.2, 2.3, and 2.4. The Faked-DBSTs are presented in the next section.



Fig. 5. The common view of experimental investigation. From [1, p.103].



Fig. 3 The resonance type (I) of new experimental certification. From [10] (1998, 2002).

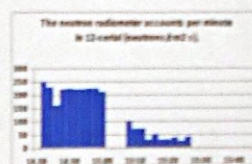


Fig. 8. The spectral reflectance around per albedo in (a) world (b) vegetation (c).

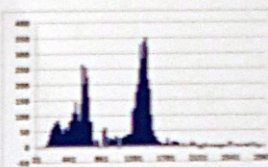


Fig. 8. Energy spectrum in ^{232}Th with lead in front of crystalline Si 3 cm from Lead-Pb source. Spectrum peak equal to 50% Thoms leads ^{232}Th .

1999, 2000, 2001, 2002, 2003, 2004, 2005, 2006, 2007, 2008, 2009, 2010, 2011, 2012, 2013, 2014, 2015, 2016, 2017, 2018, 2019, 2020, 2021, 2022, 2023, 2024, 2025, 2026, 2027, 2028, 2029, 2030, 2031, 2032, 2033, 2034, 2035, 2036, 2037, 2038, 2039, 2040, 2041, 2042, 2043, 2044, 2045, 2046, 2047, 2048, 2049, 2050, 2051, 2052, 2053, 2054, 2055, 2056, 2057, 2058, 2059, 2060, 2061, 2062, 2063, 2064, 2065, 2066, 2067, 2068, 2069, 2070, 2071, 2072, 2073, 2074, 2075, 2076, 2077, 2078, 2079, 2080, 2081, 2082, 2083, 2084, 2085, 2086, 2087, 2088, 2089, 2090, 2091, 2092, 2093, 2094, 2095, 2096, 2097, 2098, 2099, 2100, 2101, 2102, 2103, 2104, 2105, 2106, 2107, 2108, 2109, 2110, 2111, 2112, 2113, 2114, 2115, 2116, 2117, 2118, 2119, 2120, 2121, 2122, 2123, 2124, 2125, 2126, 2127, 2128, 2129, 2130, 2131, 2132, 2133, 2134, 2135, 2136, 2137, 2138, 2139, 2140, 2141, 2142, 2143, 2144, 2145, 2146, 2147, 2148, 2149, 2150, 2151, 2152, 2153, 2154, 2155, 2156, 2157, 2158, 2159, 2160, 2161, 2162, 2163, 2164, 2165, 2166, 2167, 2168, 2169, 2170, 2171, 2172, 2173, 2174, 2175, 2176, 2177, 2178, 2179, 2180, 2181, 2182, 2183, 2184, 2185, 2186, 2187, 2188, 2189, 2190, 2191, 2192, 2193, 2194, 2195, 2196, 2197, 2198, 2199, 2200, 2201, 2202, 2203, 2204, 2205, 2206, 2207, 2208, 2209, 2210, 2211, 2212, 2213, 2214, 2215, 2216, 2217, 2218, 2219, 2220, 2221, 2222, 2223, 2224, 2225, 2226, 2227, 2228, 2229, 2230, 2231, 2232, 2233, 2234, 2235, 2236, 2237, 2238, 2239, 2240, 2241, 2242, 2243, 2244, 2245, 2246, 2247, 2248, 2249, 2250, 2251, 2252, 2253, 2254, 2255, 2256, 2257, 2258, 2259, 2260, 2261, 2262, 2263, 2264, 2265, 2266, 2267, 2268, 2269, 2270, 2271, 2272, 2273, 2274, 2275, 2276, 2277, 2278, 2279, 2280, 2281, 2282, 2283, 2284, 2285, 2286, 2287, 2288, 2289, 2290, 2291, 2292, 2293, 2294, 2295, 2296, 2297, 2298, 2299, 2300, 2301, 2302, 2303, 2304, 2305, 2306, 2307, 2308, 2309, 2310, 2311, 2312, 2313, 2314, 2315, 2316, 2317, 2318, 2319, 2320, 2321, 2322, 2323, 2324, 2325, 2326, 2327, 2328, 2329, 2330, 2331, 2332, 2333, 2334, 2335, 2336, 2337, 2338, 2339, 2340, 2341, 2342, 2343, 2344, 2345, 2346, 2347, 2348, 2349, 2350, 2351, 2352, 2353, 2354, 2355, 2356, 2357, 2358, 2359, 2360, 2361, 2362, 2363, 2364, 2365, 2366, 2367, 2368, 2369, 2370, 2371, 2372, 2373, 2374, 2375, 2376, 2377, 2378, 2379, 2380, 2381, 2382, 2383, 2384, 2385, 2386, 2387, 2388, 2389, 2390, 2391, 2392, 2393, 2394, 2395, 2396, 2397, 2398, 2399, 2400, 2401, 2402, 2403, 2404, 2405, 2406, 2407, 2408, 2409, 2410, 2411, 2412, 2413, 2414, 2415, 2416, 2417, 2418, 2419, 2420, 2421, 2422, 2423, 2424, 2425, 2426, 2427, 2428, 2429, 2430, 2431, 2432, 2433, 2434, 2435, 2436, 2437, 2438, 2439, 2440, 2441, 2442, 2443, 2444, 2445, 2446, 2447, 2448, 2449, 2450, 2451, 2452, 2453, 2454, 2455, 2456, 2457, 2458, 2459, 2460, 2461, 2462, 2463, 2464, 2465, 2466, 2467, 2468, 2469, 2470, 2471, 2472, 2473, 2474, 2475, 2476, 2477, 2478, 2479, 2480, 2481, 2482, 2483, 2484, 2485, 2486, 2487, 2488, 2489, 2490, 2491, 2492, 2493, 2494, 2495, 2496, 2497, 2498, 2499, 2500, 2501, 2502, 2503, 2504, 2505, 2506, 2507, 2508, 2509, 2510, 2511, 2512, 2513, 2514, 2515, 2516, 2517, 2518, 2519, 2520, 2521, 2522, 2523, 2524, 2525, 2526, 2527, 2528, 2529, 2530, 2531, 2532, 2533, 2534, 2535, 2536, 2537, 2538, 2539, 2540, 2541, 2542, 2543, 2544, 2545, 2546, 2547, 2548, 2549, 2550, 2551, 2552, 2553, 2554, 2555, 2556, 2557, 2558, 2559, 2560, 2561, 2562, 2563, 2564, 2565, 2566, 2567, 2568, 2569, 2570, 2571, 2572, 2573, 2574, 2575, 2576, 2577, 2578, 2579, 2580, 2581, 2582, 2583, 2584, 2585, 2586, 2587, 2588, 2589, 2590, 2591, 2592, 2593, 2594, 2595, 2596, 2597, 2598, 2599, 2600, 2601, 2602, 2603, 2604, 2605, 2606, 2607, 2608, 2609, 2610, 2611, 2612, 2613, 2614, 2615, 2616, 2617, 2618, 2619, 2620, 2621, 2622, 2623, 2624, 2625, 2626, 2627, 2628, 2629, 2630, 2631, 2632, 2633, 2634, 2635, 2636, 2637, 2638, 2639, 2640, 2641, 2642, 2643, 2644, 2645, 2646, 2647, 2648, 2649, 2650, 2651, 2652, 2653, 2654, 2655, 2656, 2657, 2658, 2659, 2660, 2661, 2662, 2663, 2664, 2665, 2666, 2667, 2668, 2669, 2670, 2671, 2672, 2673, 2674, 2675, 2676, 2677, 2678, 2679, 2680, 26

[illegible]

100

- [3] A. Fagard and A. Roux, "A new energy source from nuclear fusion", *Journal of Nuclear Physics*, March 2012.
- [4] A. Fagard, "New Generation of Fusion and Fission and the Development of Fusion", *Scientific Research*, vol. 10, no. 3, pp. 49-55, 2012.
- [5] Y. A. Izrael, V. A. Kozlov, V. M. Kuznetsov, A. P. Pavlov, et al., "Research of Thermodynamic and Radiation Effects in Cooling of Air", *Scientific Research*, vol. 10, no. 3, pp. 56-60, 2012.
- [6] Y. A. Izrael, V. A. Kozlov, V. M. Kuznetsov, A. P. Pavlov, et al., "Investigation of Radiation Effects in Cooling of Air", *Scientific Research*, vol. 10, no. 3, pp. 61-65, 2012.
- [7] Y. A. Izrael, "Experimental Study of Heat Transfer in Cooling of Air", *Scientific Research*, vol. 10, no. 3, pp. 66-70, 2012.

- [illegible]

Presurized Plasma Electrolysis

J. P. Biberian¹, M. Valat², P. P. Clauzon³

¹ Aix-Marseille Université, 13288 Marseille cedex 9, France, jpbiberian@yahoo.fr

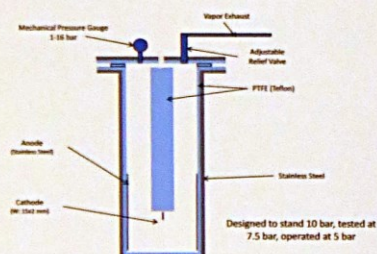
² MFMP, 7, rue de l'Église 30190 St Geniès de Malgoirès, France

³ CNAM Electrochimie, 2 rue Conté, 75003 Paris, France

Objective:

Check the influence of a magnetic fields in the production of Excess Heat in a high pressure plasma electrolysis

- All Teflon covered cell
- Operation at 5 bars
- Power input measured with a Wattmeter (70kHz sampling rate)
- Power output measured by water vapor loss
- Heat loss by through the walls of the cell: 93 Watts at 5 bars
- DC Power supply: 600 Volts – 3.3 A, or 300 Volts – 6.6 A.



Cell on the balance



10 pairs of magnets are positionned around the stainless steel anode



Dry water vapor coming out from the exhaust pipe

- Excess heat depends on electrolyte: KOH or Li_2SO_4
- Tungsten and nickel anodes have been tested.
- Different types of magnetic fields have been tested: Permanent magnets on the anode, 250 turns coil around the cell in series with the current
- Excess heat of up to 12% has been measured with both the permanent magnets and the coil.

Experimental Evidence of Excess Heat by Mass Flow Calorimetry with Ni-LiAlH₄ Powder

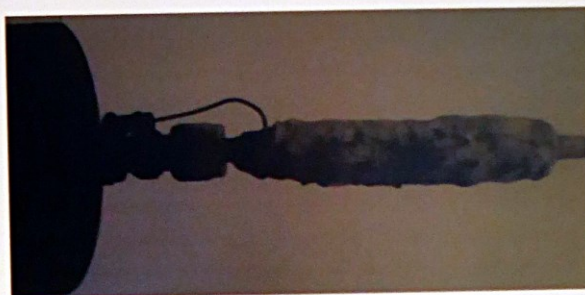
Jean-Paul Biberian

Aix-Marseilles University, France

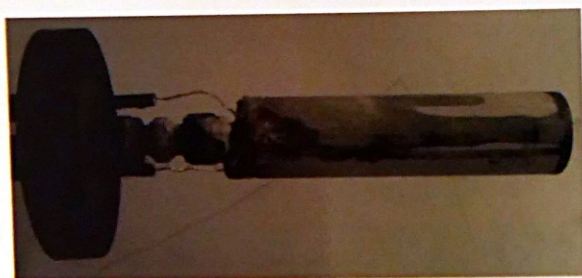
jpbiberian@yahoo.fr



Alumina tube :
10cm long, 6mm OD, 4mm ID
1g Ni+ 0.1g LiAlH₄



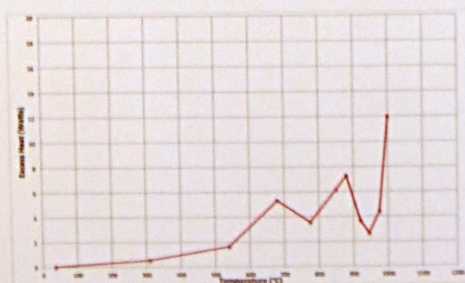
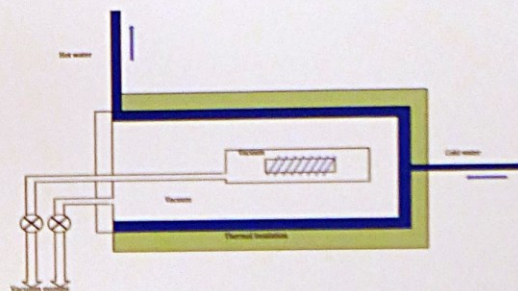
Alumina tube with platinum wire
heater covered with alumina
cement



Tube inside a 35mm stainless
steel under vacuum with 3
stainless steel screens



Powder after experiment,
showing sintering



Excess Heat Observed with a Capacitor having one Palladium Electrode

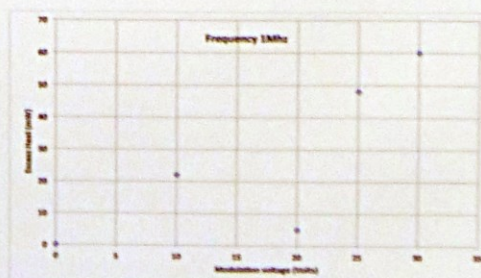
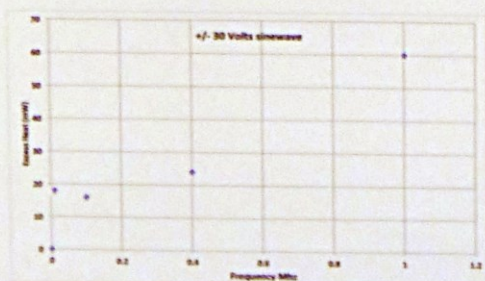
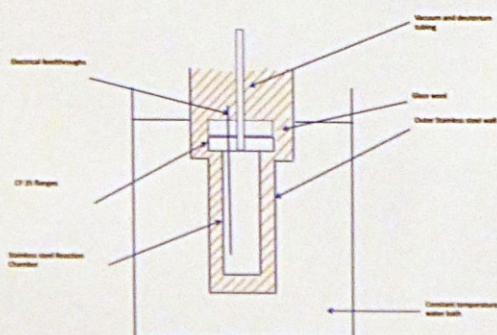
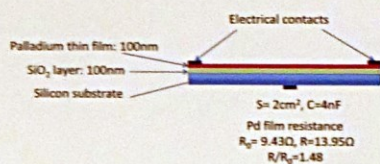
Jean-Paul Biberian

Aix-Marseilles University, France

jpbiberian@yahoo.fr

Objective:

Check the influence of the voltage and the frequency in a capacitor with one electrode being a thin palladium film.



Yet Another LERN Theory: Electron Mediated Nuclear Reactions (EMNR)

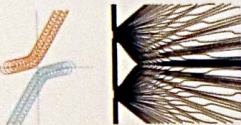
Andrea Calaon
Independent Researcher, a.calaon@libero.it
ICCF 19, Padua 2015-04

Background

LENR has been discussed for 26 years and no widely accepted explanation has emerged.
Therefore the phenomenon must be based on some not commonly accepted fact of physics.

Uncommon Assumptions Chosen for Building this Theory:

1. Nuclei are kept together by the **electromagnetic interaction** through the Magnetic Attraction Mechanism proposed by Dallacasa and Cook (ref. [1]). The approach assumes that the magnetic moment of nucleons comes from the rotation of charges, and not from gluons or intrinsic properties of the quarks.
2. The electron **Zitterbewegung** (ZB) (ref. [2]) is not different from the internal charge rotation of the nucleons. So electrons can be attracted to nucleons by the same magnetic force that keeps nucleons together.



Magnetic Attraction Mechanism

If a particle has a magnetic moment it must generate an oscillating magnetic field.

Assumption: the magnetic moment comes from the rotation of a **single charge** (simplification for nucleons) along a circular orbit of fixed radius at the **speed of light**:

$$r = 2 \frac{m_{\text{mag}}}{gqc} \quad \omega = \frac{c}{2\pi r}$$

Where m_{mag} is the magnetic moment and g the gyromagnetic ratio.

The magnetic field around a particle, without relativistic corrections, is described by the very well known formula:

$$B_1 = \frac{\mu_0}{4\pi} \frac{q_1 v_1 \wedge R_{12}}{R_{12}^2}$$

1 stands for the emitting charge, 2 for the place where the magnetic field is evaluated, μ_0 is the vacuum permeability, v_1 is the particle speed (in modulus equal to c), R_{12} is the radius at which the magnetic field has to be evaluated, and $|R_{12}|$ is the unit vector in the direction of R_{12} .

When another massive particle with a magnetic moment is immersed into this oscillating magnetic field, the magnetic part of the Lorentz force ($F_2 = q_2 v_2 \wedge B_1$) generates a "strong" (oscillating) attractive force on the rotating charge that can overcome the electrostatic repulsion. The formula is:

$$F_2 = \frac{\mu_0}{\pi} \frac{m_{\text{mag}2} m_{\text{mag}1}}{g_2 r_2 g_1 r_1} \frac{|v_1| |v_2| |R_{12}|}{R_{12}^2}$$

Necessary Conditions for Max. Attractive Force

- **Alignment** of magnetic moments: parallel or anti-parallel.
- Frequency: **Synchronous** rotation.
- **Phase**: 0 for parallel spins and π for anti-parallel spins.

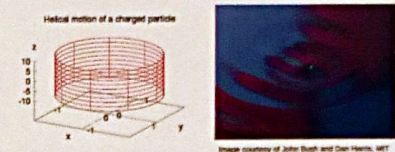
Proton:

- $r_p = 0.105$ [fm] (much smaller than its charge radius, 0.87 [fm])
- $\omega_p = 4.54 \cdot 10^{23}$ [Hz].

At 2 [fm], the bounding potential between nucleons reaches a few [MeV], as the nuclear force.

Electron Zitterbewegung

The electron manifests as a point charge with an intrinsic and very rapid rotation at $2.47 \cdot 10^{20}$ [Hz], the so called Zitterbewegung (ZB). The electron "speed" combines with the ZB giving a "variable pitch-constant radius" helical motion. The radius is about 193 [fm], much larger than the nucleons.



Coupling Between Electron and Hydrogen Nucleus

$$\omega_p/\omega_e = 1,836.152 = m_{\text{proton}}/m_{\text{electron}}$$

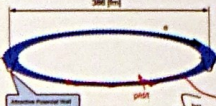
So for an attraction between the electron and a hydrogen nucleus the electron must somehow rotate around the proton at very low and unusual frequency (about 2 [kHz]).

The speed of electrons is always higher than that of hydrogen nuclei. In the hydrogen atom for example the electron "speed" is about 2.200 [km/s], while nuclei vibrate at a few [km/s]. So normally electron and hydrogen do not attract each other.

The NAE should therefore host a mechanism that somehow "slows down" the rotation of the electron to extremely low frequencies.

Hydronions (Hyd) Formation

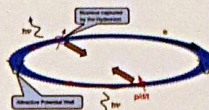
When the hydrogen nucleus crosses the ZB radius the attractive magnetic force becomes repulsive, so that the hydrogen nucleus is captured inside the ZB trajectory, as schematically shown here:



The absence of electrostatic repulsion allows a larger range if compared with the nuclear force.

The LENR Take Place in Two Stages

Hydronions behave similarly to a neutral particle; no charge, short charge separation and high displacement frequency. Hydronions therefore can penetrate any electronic orbital and attract other nuclei towards the ZB trajectory through the magnetic attraction. Once two nuclei are both moving along the ZB, they will attract each other because now their magnetic moments are aligned.



The nuclear fusion between the two nuclei takes place in very special conditions. These special conditions are the reason why LENR do not generate the same products of hot fusion.

So the LENR (or EMNR) happen in two stages:

- **First Stage**: Generation of Hyd (it needs a NAE).
- **Second Stage**: The Hyd are captured by other nuclei and host nuclear reactions at very low excess kinetic energy.

The flow of Hyd is the "strange radiation" detected in many LENR experiments.

The second stage should be responsible for the metachronous thermal effects and the double optimal operating power measured by Mitchell Swartz (see ref. [4]).

Second Stage Reactions with Hydrogen Nuclei

When Hyd react with hydrogen nuclei:

1e : p+ep	-> d + neutron + (max)	1.442 [MeV] - Gp
2e : p+ep	-> e + neutron + (max)	5.475 [MeV] - Gd
3e : d+ep	-> e + neutron + (max)	5.475 [MeV] - Gp
3e : d+ep	-> He3 + e +	4.472 [MeV] - Gp
4e : d+d+0.141 [MeV]	-> He4 + neutron +	0.00 [MeV]
	He4 -> e + n +	3.391 [MeV]
4.1 : d+d	-> He4 + e +	22.825 [MeV] - Gd
4.2 : d+d	-> e + ep +	4.033 [MeV] - Gd +
5e : t+ep+4.174 [MeV]	-> He4 + neutron +	0.00 [MeV]
	He4 -> e + n +	3.391 [MeV]
5 : t+ep	-> He4 + e +	18.792 [MeV] - Gp
6e : t+d+5.318 [MeV]	-> He4 + neutron +	0.00 [MeV]
	He4 -> e + n +	2.311 [MeV]
6.1 : t+d	-> He4 + e +	15.832 [MeV] - Gd
	He4 -> He4 + n +	0.735 [MeV]
6.2 : t+d+5.616 [MeV]	-> He4 + ep +	3.391 [MeV]
	He4 -> e + n +	3.391 [MeV]
7 : t(beta decay)	-> He3 + e + antineutrino + (aver)	5.7 [MeV]
8e : He3+ep	-> He4 + neutron + (max)	19.80 [MeV]
9 : He3+d	-> He4 + ep + (max)	20.58 [MeV]

Remarks:

- The reactions producing neutrons are endothermic.
- If $Gp > 1.442$ [MeV] reaction 1e, which produces deuterium, is endothermic.
- When He4 is produced there is a large energy release.
- The minimum energy contribution for producing neutrons is 0.141 [MeV] + Gd (reaction 4e).
- Tritium is generated without the production of free neutrons: this explains the so called "branching ratio anomaly".
- When tritium is destroyed in presence of Deuterium (reaction 6.1), neutrons are produced.
- If Hydronius (ep) produced by reaction 4.2 decomposes, this becomes the source of protons/molecular hydrogen in cases of deuterium loading.
- When tritium is destroyed, a large quantity of energy is released.

Some General Remarks

Susceptibility to a Magnetic Field

The proposed LENR mechanism is essentially magnetic and should be susceptible to the presence of a magnetic field.

Some Nuclei Do Not React

The magnetic coupling in fact has a chance to take place only if a nucleus has a magnetic moment, not only of first order. Ni62 seems to be an example.

Preference for Stable Nuclei

The very low excess kinetic energy of the fusion reactions inside the ZB could be the reason for the preference of stable nuclei. Plus the mediation of the electron offers a completely different setting for the fusion reactions.

No Tritium Accumulation

Magnetic moment ratios: $m_d/m_p = 0.31$, and $m_n/m_p = 1.07$.

So the reactions with deuterium should be kinetically slower than those with protium and tritium.

Sources of tritium:

2e : p+d	-> t + neutron + (max)	5.475 [MeV] - Gd
3e : d+ep	-> t + neutron + (max)	5.475 [MeV] - Gp
4.2 : d+d	-> t + ep +	4.033 [MeV] - Gd + Gp

Tritium sink:

5 : t+ep	-> He4 + e +	18.792 [MeV] - Gp
----------	--------------	-------------------

All reactions producing tritium involve deuterium (slower reaction), while the elimination of tritium involves protium (faster reaction). Tritium should not accumulate.

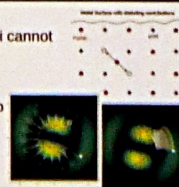
This should be the reason for the lack of accumulation of tritium and for its reported elimination.

The Nuclear Active Environment (NAE)

What is necessary for the formation of a Hydronion?

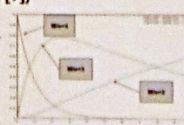
- Electron and proton have to rotate one around the other at a very low speed (almost rest), and
- At short distances (normally the electron has "higher speeds" near to the nucleus).

- Electrons are too fast.
- Inside a solid hydrogen nuclei cannot be accelerated.
- There should be a mechanism that "moves around" an orbital at low radio frequencies: A phonon-vacancy hopping coupling with an orbital that sustains an epitrochoid-like trajectory.



Interpretation of Measured Gas Evolution by Yoshino, Igari and Mizuno (ref. [7])

- Mass 4 decreases because of D_2 absorption; $4He$ can not contribute.
- Mass 3 increase is due to reaction 4.2, 3 (and 3e).
- Reaction 3 uses ep (Hydronius) from reaction 4.2.
- Part of the gas with mass 3 is $3He$.
- Reaction 4.2 is the main source of mass 2 increase (molecular hydrogen), because either reaction 4.2 produces $e + p$ or $ep + Gd$ decomposes into e and p ($p+ep+H_2$).
- Reaction 6.1 is the source of the detected neutrons. This energetic reaction requires tritium inside the metal matrix.



Summary of Relevant Features of the EMNR Theory

- The Coulomb barrier is not overcome kinetically.
- The LENR take place in two stages:
 - **First Stage**: Formation of the Hydronions.
 - **Second Stage**: the "neutral" Hyd penetrate electron shells, capture other nuclei, which then fuse "inside the electron".
- Thanks to the mediation of the electron, the LENR can release most of the energy as photons during the acceleration of the particles.
- The NAE is a place where the electron orbital is forced to oscillate at a very low frequency in the RF range. It is suggested that a coupling between optical phonons and vacancy hopping in presence of an orbital with epitrochoid-like trajectories is involved.
- The products of the suggested reactions agree qualitatively with experimental results.

References

- [1] Dallacasa V., Cook N. D., Models of the Atomic Nucleus, ISBN-10: 3540265685.
- [2] Cook Norman D., Dallacasa V., LENR and Nuclear Structure Theory for ICCF-17.
- [3] Hestenes D., "Zitterbewegung in Quantum Mechanics - a research program", on arXiv.org.
- [4] Swartz Mitchell, "Amplification and Restoration of Energy Gain Using Fractionated Magnetic Fields on ZnO-Au Nanoparticles", ICCF 18, 2013.
- [5] Viorito V., Castagna E., Leoni S., Pagano G., Samonini M., Sarto F., "RF detection and anomalous heat production during electrochemical loading of deuterium in palladium", DOI 10.12910/EA2014-6, 2014.
- [6] Giuseppe Levi, Evelyn Fucini, Bo Hildead, Roland Pettersson, Lars Tognoli, Hanno Enslin, Observation of abundant heat production from a reactor device and of isotope changes in the fuel.
- [7] Tadahiko Mizuno et Hideo Yoshino Clean Planet, Inc., Replicable Model for Controlled LENR Reaction using Metal Nanoparticles, presentation given at 2014/03 CFI/ANR Colloquium at MIT.

This Work has been prepared Independently from scientific institutions and without industrial support.



The Significance of a Properly Conceived and Instrumented Calorimetry

E. Castagna, S. Lecci, M. Sansovini, F. Sarto, V. Violante RdA

ENEA, Technical Unit of Fusion, Lab. of Fusion Nuclear Technologies - Via Enrico Fermi, 45 - 00044 Frascati (Rome) ITALY

ABSTRACT

Mass flow calorimetry has been used to study the excess power production during electrochemical loading of palladium with deuterium.

The experimental chain was conceived to monitor not only the electrochemical conditions but also the deuterium concentration into the palladium sample, the gas pressure in the cell and the coolant flow rate.

The loading measure allowed to relate the onset (and disappearance) of the effect on a loading threshold.

The pressure measure was conceived in order to identify thermal signals to be ascribed to a chemical reaction between deuterium and oxygen in the cell.

The measure and control of coolant mass flow rate was performed to have a properly accuracy of the output power measurement.

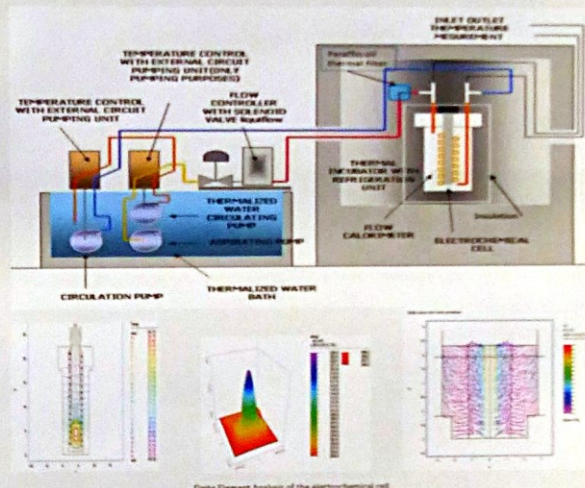
Experimental Set Up



Electrochemical cell for mass flow calorimetry

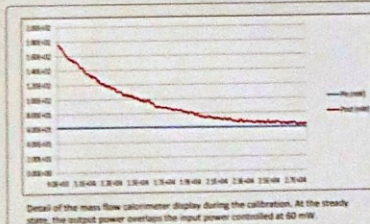


Pd cathode, showing the five Pt wires used as electrical contacts. The sample dimensions are 20mm X 10mm X 50 microns

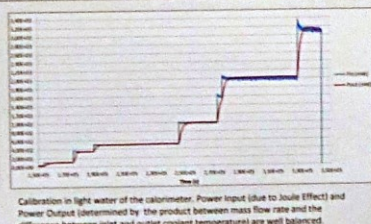


Finite Element Analysis of the electrochemical cell

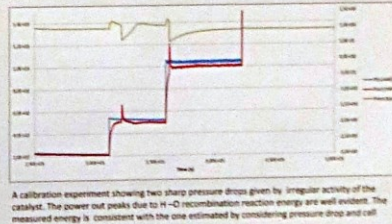
Calibration Experiments: No Excess Heat



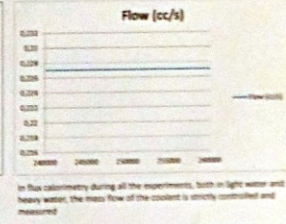
Detail of the mass flow calorimeter display during the calibration. At the steady state, the output power overlaps the input power controlled at 60 mW.



Calibration in light water of the calorimeter. Power input (due to Joule Effect) and Power Output (determined by the product between mass flow rate and the difference between inlet and outlet coolant temperature) are well balanced.



A calibration experiment showing two sharp pressure drops given by irregular activity of the catalyst. The power out peaks due to H-O recombination reaction energy are well evident. The measured energy is consistent with the one estimated by considering pressure drop and cell free volume.



In flux calorimetry during all the experiments, both in light water and heavy water, the mass flow of the coolant is strictly controlled and measured.

Anomalous Heat Production Experiments

Sample L17

Sample L17 gave two anomalous heat burst, with a ratio P_{out}/P_{in} around 300% (Fig.1). After the first, quite short in time, the second one lasted for several hours.

Deloading bursts are well visible and related to disappearance of the anomalous heating (Fig.2). Pin depletion is due to decreasing of cell voltage and current caused by the behaviour of the implemented instrument (Fig.3). The measurement has been improved in experiment L30.

Cell Temperature (T_{cell}) increased before the coolant outlet temperature (T_{out}), showing that heat was produced inside the cell itself (Fig.4). Coolant flux is strictly controlled during the anomalous effect rising (Fig.5)



Fig.1 - Anomalous Power Bursts

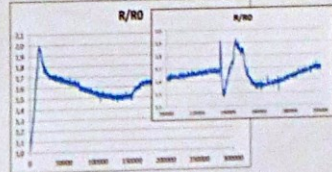


Fig.2 - Loading evolution given by R/Ro measurement



Fig.3 - Cell current and voltage depletion during anomalous effect

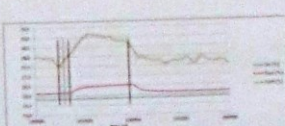


Fig.4 - Time correlation between coolant and cell temperature

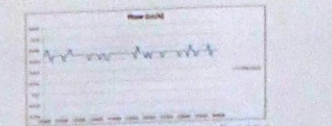


Fig.5 - Coolant flux during anomalous effect rising

CONCLUSIONS

A properly conceived measurement chain allows to perform checks that are of remarkable importance to remove doubts on the observed onset of the effect. The approach described paves the way to conceive updated experiments that could require specifically designed and realized instruments.

Sample L30

Sample L30 showed anomalous heat production with a ratio P_{out}/P_{in} greater than 500% (Fig.6). The deuterium deloading seems to be well related to the disappearance of the effect (Fig.7 and Fig.8).

The energy produced by D-O recombination revealed by the pressure drop is much lower than the total energy gain (Fig.9).

Pin depletion is absent, unlike experiment L17, as current measurement method was different. Cell voltage decreased as T_{cell} increased because of electrolyte electrical resistance variation (Fig.10).

Cell current (I_{cell}) was noisy during the anomalous effect, hinting to an undersampled RF signal event (Fig.11).

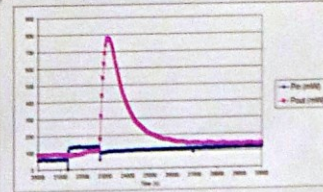


Fig.6 - Anomalous Power Burst



Fig.7 - Deuterium deloading during anomalous effect. The two peaks are ascribed to electric noise.

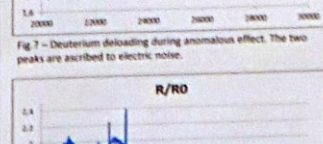


Fig.8 - Loading behaviour during all the experiment

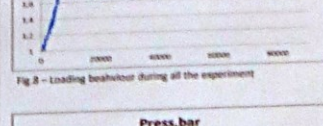


Fig.9 - Pressure drop is not consistent with total energy production

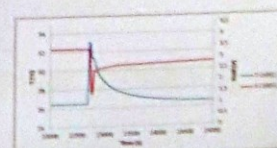


Fig.10 - Cell voltage evolution related to Tcell variation

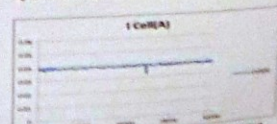


Fig.11 - Current ripple assumed to be an undersampled RF signal

Observation of macroscopic current and thermal anomalies, at HT, by hetero-structures on thin and long Constantan wires under H₂ gas

Francesco Celani^{1,2}, G. Vassallo^{1,3}, E. Purchi¹, F. Santandrea¹, A. Nuvoletti¹, M. Nakamura¹, P. Cirilli¹, A. Spallone^{1,2}, B. Ortenzi¹, S. Pella¹, P. Bocconera¹

1) INFN-LNF, Via E. Fermi 40, 00044 Frascati-Italy, 2) ISMNS, Latium#1 Group, Via Cavour 26, 03013 Ferentino-Italy
3) DICGIM, Univ. Palermo, Viale delle Scienze Ed. 6, 90128 Palermo-Italy

Introduction

Since the end of 2011 we introduced, in the LENR research field, a new (low cost) material, Copper-Nickel alloy, named "Constantan" (ISOTAN 44, Isabellshutte-Germany, composition: Cu₅₅Ni₄₅), wire shaped (φ=100μm; L=0.1-0.2mm).

We demonstrated experimentally that such alloy, at nanometric dimension and at high enough temperatures (>120°C), catalyzes the dissociation of H₂ to 2H and adsorbed protons in the lattice.

[S. Romanowski et al., Langmuir 1999, 15, 5773-5780].

The results, by computer simulations, of capability of H₂ dissociation, according to Romanowski, were:

Ni ₁₂₅ -Cu ₁₂₅	+3.16eV
Ni ₁₂₅ -Cu ₁₂₅	+2.86eV
Ni ₁₂₅ -Cu ₁₂₅	+2.10eV
Ni	+1.74eV
Ni ₁₂₅ -Cu ₁₂₅	+1.57eV
Ag ₁₂₅ -Pd ₁₂₅	+0.57eV
Ag ₁₂₅ -Pd ₁₂₅	+0.51eV
Ag ₁₂₅ -Pd ₁₂₅	+0.51eV
Pd	+0.42eV
Cu	-1.11eV
Ag	-1.42eV

In order to increase the overall catalytic properties, i.e. the surface area, the wires were subjected to specific thermoelectric treatments: made sub-micrometric and multilayered nanostructures, vaguely similar to hetero-structures. The threshold temperature, in free air, to produce sub-micrometric structures, just by oxidation, is 600°C.

Our specific thermal treatments were aimed to produce sub-micrometric geometries (chaotic like mixtures of Ni, NiO, Cu, CuO, Ni₂Cu₃O₄), avoiding, at same time, self-sintering processes due to the high temperatures: irregularly shaped/mixed materials.

The electric high peak power pulses (20kV/μs of material; 1-1μs; J=50kA/cm² even neglecting skin effect) induce extremely fast thermal treatments and shock waves. Obtained glassy materials at surface.

We were inspired by the "Melt Spinning and Quenching" metallurgical process, largely used by Yoshiaki Arata and Collaborators (Osaka, Tohoku Universities), to produce nanomaterials (Pd, or PdNi, both dispersed into a matrix of ZrO₂, at 65% concentration) for his "SSF" (Solid State Fusion) devices under interaction with pressurized (up to 60 Atm.) D₂, H₂ at 150-300°C.

The key principles/procedures of Y. Arata, specific nano materials, were reproduced/modified, among others, by A. Takahashi-A. Kitamura (Osaka-Kobe Universities, also at Technova-Japan), B. Ahern (DARPA-USA), our group in Italy (by wires).

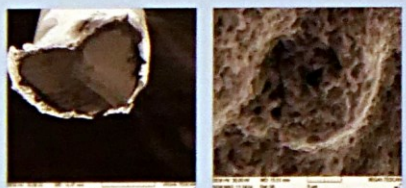


Fig. 1 - SEM - Cross section of virgin wire, as provided by Isabellshutte, with "plastic" cover at the surface (lighter area at the micro-photography).

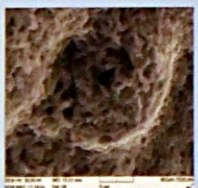


Fig. 2 - SEM - Wire's surface after heat treatments: DC current >2500 mA, time 3 minutes.

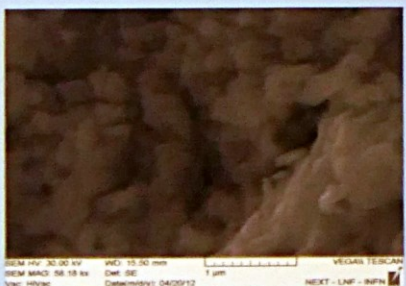
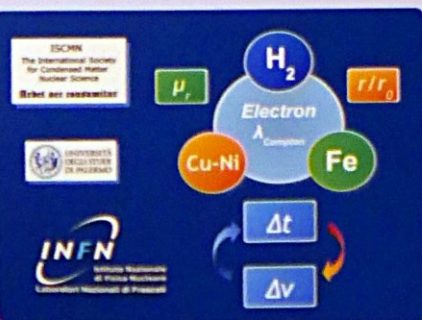


Fig. 3 - Typical SEM of wire surface after repeated pulse treatments by high power pulse.



First Generation Experiment

Some of the results obtained, using a simple dissipation reactor made of a thick-wall Borosilicate Glass (BSG) tube, were quite reproducible and the Anomalous Heat Effect (AHE) detected (at Constantan wire surface temperatures of 160-400°C) was about 5-10W with 50W of electric input power [CCF17, August 2012, Daejeon-South Korea].

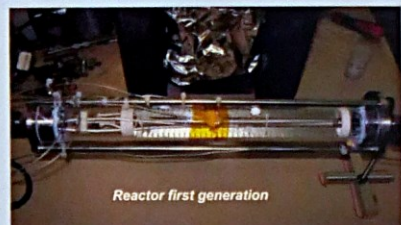


Fig. 4 - Photo of the small, dissipation type, transparent reactor operating at INFN-LNF. The volume is about 250cc. The 2 wires, reference and active, are rounded on a mica support. The thermocouples are Type K, SS screened (diameter 1.5 millimeter).

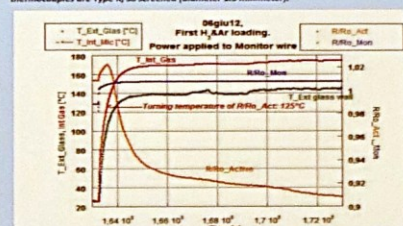


Fig. 5 - Details of first loading by H₂-Ar mixture. The "trigger" temperature, to get the large resistance decrease of sub-micrometric Constantan wire, was about 125°C. Temperature measured by a type K thermocouple (SS sealed) inside the gas cell.

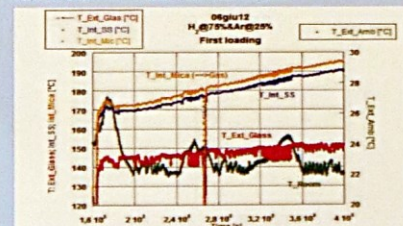


Fig. 6 - Behaviour of the temperatures of the reactor, at CONSTANT input power (48W at Max. wire). Flowing the time, BOTH the external glass temperature (140-150°C) and the 2 internal (gas, 170-195°C; Stainless Steel, 160-190°C), increased. The effect was not directly related to room temperature variations, although such temperature variation helped to get not-stationary conditions.

Later on, we realized that the overall reproducibility was not satisfactory as observed in the first series of experiments. Using SEM/EDS (and ICPMS) analysis we found, among others, that the first batches of raw material used (produced before 1970) had a composition different from more recent ones. The main difference was Fe contamination, in the order of 1000-5000 (and up to 10000 locally) PPM.

Effect of fiber Glass on H storage

We found that even the BSG fiber sheaths (BSGFS, SIGI-Italy), largely used in our experiments as electric insulator, could have some role in AHE generation. In short, hydrogen eventually dissociated by the Constantan wire, is largely adsorbed into the surface of the micrometric (φ=5μm) braided fibers. Such BSG property was observed by Nobel Laureate Irving Langmuir since 1920. The amount of adsorbed H₂ at low temperatures, was in the order of 10⁻¹⁵ atoms/cm². In our experiment the effective surface of such sheath is >1m². The total amount of fiber used may have a total surface >50m². We realized that such BSG property may enhance the absorption of Hydrogen in Constantan lattice and related AHE. [F. Celani et al. "MIT-2014 Colloquium on Cold Fusion Effects", March 21-23, 2014, Cambridge-USA].

Fig. 7 - Photo of braided wires.

Single Wire Spontaneous Voltage Generation

In a typical setup we have a Platinum wire (φ=100μm) used mainly for calibration purposes ("reference") and two Constantan wires (the "active") with different diameters (100, 200μm) and/or surface treatments. Each wire is inserted inside a BSGFS. The 3 sheaths are closely braided each other and put inside twin BSGFS for thermal homogeneity. We can control only two wires at same time. For this reason one of Constantan wires is not acquired by the DAQ (Pico, NI) and is left unconnected (floating), but periodically his resistance value is measured by a general-purpose multimeter to evaluate the presence of adsorbed Hydrogen. We observed that the wire resistance decreases (up to values as low as 70% of initial one, the so-called R/R₀ ratio), when the Constantan wire is heated in presence of Hydrogen. On June 25, 2014, we noted, almost by chance, that Constantan wire generates by itself a macroscopic voltage (>100mV), that is function of many parameters (temperature, gas type, pressure, value of R/R₀). Maximum values (not stable over time, only few hours) were of the order of 1400mV and current of 120μA. Stable values were about half. The effect is not the usual Seebeck effect because we use only one wire, NOT a junction of 2 different materials, like in thermocouples.

Iron Addition

Finally, taking into considerations our old results (2012) we developed a new procedure to add Iron, at nanometric dimensions, over the surface (and even inside the bulk, some microns) of Constantan wires during the several preparation steps. The Fe is one of the few elements characterized by a solubility of H inside lattice that increases, largely, increasing the temperature (from 5.37eV/100g at 400°C to over 7eV at about 1000°C). Because such reason, we added another sheath, over the usual BSGFS, based on Al₂O₃ material (T_{max}=1200°C). In order to increase the local wire temperature keeping constant the input power we used also a mixture of Hydrogen with gas of low thermal conductivity (Ar/Xe). Comparing results, about AHE, we observed that low thermal conductivity gas mixture is more efficient to increase it. We remember that all the sheaths, since February 2013, were embedded by SiO₂ material at low working function for electrons emission, similar to CaO used by Yashuro Iwamura at Mitsubishi Japan.

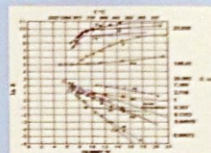


Fig. 8 - Solubility of H in various metal (100 g) vs. temperature at 1 Atm.

Thanks to a new procedure developed at INFN, 20-40 Fe thin layers can be made at wire surface, like multiple heterostructures. Moreover, we introduced, local, geometric variation of the current paths injected inside the wire by making several (up to 20), low diameter hole (0.3-2mm) knots: even magnetic effects are expected. Obviously the knots are places of large thermal not homogeneity when the large current is flowing. Recent experiments with/without Fe and knots, and their combinations, show that such new setup could have measurable advantages from the point of view of Hydrogen absorption and AHE values, especially at High Temperatures (>400°C). The last value of AHE, very conservative (i.e. the wire without local Fe added is supposed to be the blank with DW of AHE), gives values larger than 15W at a local wire temperature around 800°C (estimation using Pt wire) and input Power of 100W.

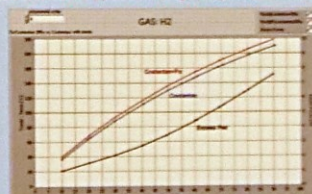


Fig. 9 - Gas H₂ - Excess Power vs. applied Power for wires without and with Fe.

Very recently, with wires having several knots (hole diameter<1mm) filled with Fe at nanometric size (mostly inside knots), we observed that it generated currents up to 150μA and voltages up to 1900mV stable over long times. Comparing the values of spontaneous voltages, both wires with the same number of knots, we measured values about 2.2 times larger using the Fe addition.

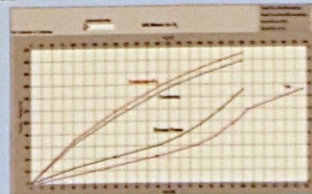


Fig. 10 - Gas mixture: 3x 1.4 bar, H₂ 1.7 bar. Excess Power and temperature of stain steel T10 internal support.

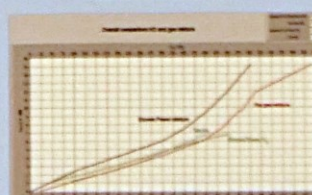


Fig. 11 - Overall comparison among H₂ and Gas mixtures. Higher wire temperatures, correlated with higher values of T₁₀, give larger values of AHE.

Conclusions

According to our observations we can infer that the AHE, and low spontaneous voltage, are related to some of the following parameters and conditions:

- Absolute value of temperature, as large as possible, obviously avoiding material sintering.
- Enough amount Hydrogen adsorbed/adsorbed by the catalytic material, i.e. nanomaterials.
- Flux (as large-fast as possible) of Hydrogen from region of high concentration to lower one.
- The addition of elements that have Hydrogen concentration increasing with temperature (like Fe).
- The wires that have good performances from the point of view of AHE values show values of spontaneous voltages quite non-stable.
- The non-equilibrium conditions, as large as possible, look the most important condition to get any type of thermal or electrical anomalies.
- More work is necessary to better understand the complex phenomenology and to increase further useful "anomalies".

Norman D. Cook (Informatics, Kansai University, Japan) and Andrea Rossi (Leonardo Corporation, USA)

The "independent-particle model" (IPM) has been the dominant paradigm in nuclear physics since the early 1950s. In the IPM, a wave-equation, similar to that used to describe electron states in atoms, defines all possible quantum states of nucleons:

$$\Psi_{\text{normal}} = R_{\text{normal}}(r) Y_{\text{normal}}(\theta, \varphi)$$

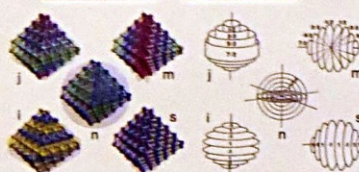
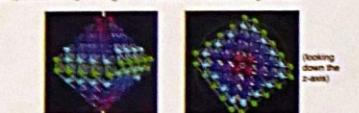
These states can be tabulated in terms of the occupancy of "n" shells, "j" subshells, and "m" sub-subshells with spin-up and spin-down protons and neutrons. The sequence and occupancy of these states have been experimentally confirmed for ~2000 ground- and several hundred thousand excited states. This is the essence of well-established, conventional nuclear theory.

Quantum Number	1	2	3	4
Number of States	2	6	10	14
Energy, eV	0	10.4	20.9	31.4

The "new" idea that we bring to the IPM is Eugene Wigner's argument from 1937 that all of the shells and subshells of the IPM are reproduced in a cubic close-packed lattice built from a central tetrahedron (2 protons and 2 neutrons). The *n*-shells in the lattice are consecutive spherical shells that close closures with filling at 4, 16, 40, 80, 140, etc. particles.



In the lattice IPM, the j -subshells within each spherical n -shell show cylindrical symmetry - again in complete agreement with the build-up procedure of the conventional IPM. Below, the cylindrical j -subshells of nucleons [1=1/2 (red), 3/2 (purple), 5/2 (blue), 7/2 (turquoise), 9/2 (green)] can be seen by viewing the 140-nucleon Yt structure along its z -axis.



Indeed, all of the nucleus quantum numbers have rather simple geometrical definitions, as seen in the figure above and in the formula below:

Principal:	$n = (x + y + z - 3)/2 = 0, 1, 2, \dots$
Angular momentum:	$j = (x + y - 1)/2 = 1/2, 3/2, 5/2, \dots$
Azimuthal moment:	$m = (x - 1)(-1)^{j-1/2}/2 = 1/2, 3/2, \dots$
Spin:	$s = (-1)^{j-1/2}/2 = \pm 1/2$
Isospin:	$i = (-1)^{j-1/2} = \pm 1$
Parity:	$\pi = \text{sign}(x^*y^*z) = \pm 1$

Note that ALL of the variables in the equations above are simply nucleon coordinates!! These are geometrical definitions of quantal symmetries... nothing more and nothing less.

The correspondence between the well-established pattern of quantum numbers and one particular lattice structure should be evident from the equations and figures above. But what do these abstract "symmetries" imply for real nuclei? Below, a few concrete examples illustrate what is meant by building nuclei in accordance with the Wigner lattice. First of all, we know from the many successes of the conventional IPM that nuclei can often be accurately described as the simple summation of the properties of their "independent" nucleons. Four classic examples are the deuterons, the triton, Helium-3 and Helium-4. Note that the spin/parity values and magnetic moments of these nuclei are well predicted.



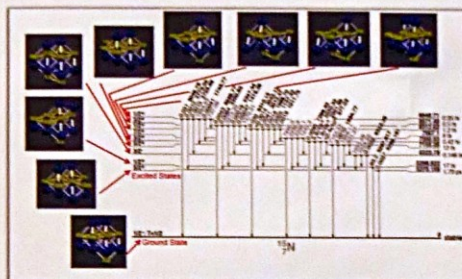
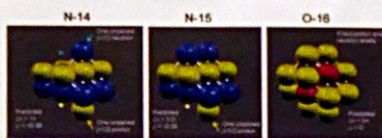
The prolate, triangular and tetrahedral shapes of these nuclei have already been discussed in contexts unrelated to the lattice depiction of the IFM, but the implications of the lattice are unique when larger nuclei are considered. There are no stable nuclei with five nucleons, but Lithium-6 and Lithium-7 are interesting examples of the predictive power of the lattice IFM

Let us start with Lithium-6. If considered to be a Helium-4 core with one proton and one neutron from the second *n*-shell, its spin-parity and magnetic moment are accurately predicted. Lithium-7 is equally well explained as a Helium-4 core with two neutrons and one proton added. From the perspective of the lattice IPM, the important question concerns which 2 or 3 lattice sites from the second *n*-shell are occupied to form Li-6 and Li-7? The answers are unambiguous. Of the 12 lattice sites in the second shell (yellow, below left), only 2 combine to give the correct spin-parity and magnetic moment for Li-6, and only 3 give those of Li-7 (or a different three to give an isomer).



Isotope	Binding Energy	Spin/Parity	Magnetic Moment	RMS Radius
Li-6	31.994 MeV	0+	+0.822	2.589 fm
He-4	28.295 MeV	0+	0.000	1.676 fm
p		1/2+	+2.983	0.865 fm
n		1/2+	-1.914	0.873 fm
Theory		1+	+0.879	2.545 fm
Li-7	39.244 MeV	3/2-	+3.256	2.444 fm
He-4	28.295 MeV	0+	0.000	1.676 fm
p		1/2+	+3.793 (Schmidt)	0.865 fm
n		1/2+	-1.914	0.873 fm
Theory		3/2-	+1.914	0.873 fm
		1/2-	-3.793	2.550 fm

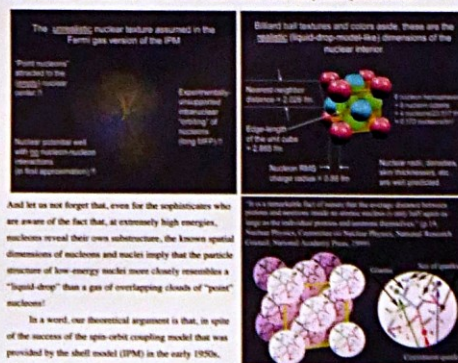
While it is not often the case that a unique lattice structure can be deduced for a given isotope or excited state, the unique structures of N-14, N-15 and O-16 and the low-lying excited-states of Nitrogen-15 are shown are shown below. Note that, in every case, the spin/parity of the lattice



structure has been chosen to produce the values known from experiment. For larger nuclei, the number of permutations of possible lattice sites for unpaired protons and/or neutrons increases rapidly, making unique identification more difficult. In this regard, the "stereochemistry" of the nucleus is as complex as the stereochemistry of molecular structures. In both fields, however, a list of constituent particles (e.g., C_6H_6 for benzene in chemistry, and 7Li for the ground state of Lithium-7 in nuclear physics) is only the first step in a genuine understanding. Although it can be said that the field of nuclear structure physics has successfully classified nuclear states in terms of the properties of their constituent particles (as in the level-diagram shown above), the structural issues of nuclear-level "stereochemistry" have not yet been addressed. Particularly for nuclear reactions involving low-lying excited-states, the detailed fine-structure of nuclei will undoubtedly need to be considered.

Just as mid-19th century chemists were at first reluctant to face the challenge of molecular geometry but eventually came to understand that the chemical formula had spatial implications, nuclear physicists today simply do not want to address the fine-grained structural issues implied by the "nuclear stereochemistry" of the lattice IPM. Despite that reluctance, the empirical phenomena of LENR suggest that theorists will need to consider the low-energy (several MeV) geometry of nucleons before delving into the (interesting, but largely irrelevant) high-energy (>300 MeV) problems of nucleon structure (i.e., QCD).

Ever since the emergence of the shell model in the early 1950s, the "Fermi gas" interpretation of the IPM has been the mainstream understanding of nuclear structure, but in fact the origins of the IPM itself lie in Wigner's theoretical work from 1937 - where he explicitly stated that the "symmetries of the nuclear Hamiltonian are those of a cubic close-packed lattice". He shared the 1963 Nobel Prize with the inventors of the shell model because of that work. We suggest that the starkly contrasting views of the nucleus - a highly unrealistic gas of point nucleons (below, left) and a realistic liquid-droplike nuclear interior (below, right) - are easily and naturally unified in the lattice version of the independent-particle model.



And let us not forget that, even for the sophisticates who are aware of the fact that, at extremely high energies, nucleons reveal their own substructure, the known spatial dimensions of nucleons and nuclei imply that the particle structure of low-energy nuclei more closely resembles a "liquid-drop" than a gas of overlapping clouds of "point" nucleons!

In a word, our theoretical argument is that, in spite of the success of the spin-orbit coupling model that was provided by the shell model (IPM) in the early 1950s, the assumptions of "point nucleons", intranuclear nucleon

"orbiting" and the ghost-like "nuclear potential well" (that, unlike all other known forces in the material world, is unattached to a material object!)) have led nuclear theorists into a cul-de-sac. Sixty years down the road, they still cannot provide any coherent statements on the nature of the nuclear force!

We suggest that the overwhelming current popularity of the gaseous-phase IPM is little more than a consequence of (1) unfamiliarity with Wigner's early work (i.e., the identity between the lattice and shell model symmetries), and (2) the extreme inapplicability of the gaseous model that allows reasonably-accurate, but inherently inconclusive, fitting of the model to experimental data.

The motivation behind the lattice IPM is **not** a fascination with crystals or classical physics or computer graphics, but more fundamentally the mathematical identity between the established quantum mechanical regularities of the atomic nucleus and the geometrical symmetries of one specific type of lattice. That lattice (an antiferromagnetic face-centred cube of nucleons with alternating isospin layers) is known from neutron scattering research to be the lowest-energy configuration of nuclear matter ($N/Z=1$) and is an obvious first-candidate as a realistic, high-density model of normal nuclei. Although the relationship between this lattice and nuclear QM has been known since the 1930s, it has gone largely unexamined in "mainstream" theory. Meanwhile, theories have come to embrace more-and-more abstract notions about a nuclear force that is no longer anchored to material objects and where - without an iota of empirical evidence - partial charges (quarks) are said to play an important role in determining nuclear structure.

By ignoring the theoretical foundations of a realistic liquid-drop-like model that is fully consistent with the symmetries of the IPM (the lattice IPM), nuclear theory since the early 1950s has wandered off into abstract realms with only tenuous connections to the material world. From the unprecedented standpoint of 'theory above all else', experimental indications of LENR have been glibly dismissed as inconsistent with 'known physics'.

$$\text{Li-7} + p \rightarrow \text{Be-8} \rightarrow 2 \text{ Alphas}$$

We hypothesize that a major source of excess heat in the E-Cat is a reaction involving Li-7, specifically, its accretion of a proton (mechanism unknown) to produce Be-8, which immediately breaks down into two alpha particles that are released with significant kinetic energy. Can the lattice IPM explain that reaction?

The ground-state for the Li-7 isotope (below, A) has four surface positions at which a fourth proton can bind (with 3 or 4 bonds) to the Li-7 core (below, B). Unfortunately, none of the candidate Be-8 structures contains two independent alpha particles (two distinct subclusters containing four nucleons each). As a consequence, if Be-8 were to form by the simple accretion of a proton to the ground-state of Li-7, two alpha particles could not be produced inside the Be-8 structure itself unless very configurational changes — with the inevitable release of gamma radiation.

Because significant gamma radiation was not observed in either the Lugano test or the Parkhomenko replication, we conclude that the direct secretion of a proton by the ground-state of $Li-7$ did not occur.



Interestingly, the lattice IPM clearly indicates that the *first excited-state* of $Li-7$ does not have this problem (above, C). Adding a $p+2/2$ proton to this structure (above, D) results in a $2+2n$ excited-state of Be-8 (below, E) that contains two independent alpha tetrahedrons (below, F). That structure implies that the break-up of Be-8 (below, G) can occur without structural reorganization and *without gamma-ray radiation*. In other words, unlike conventional nuclear theory, which does not consider the structural issues of "nuclear stereochemistry", the lattice IPM predicts that Be-8 decays from a $2+2n$ excited-state to two alphas, with the release of significant kinetic energy.



The general significance of this lattice IPM mechanism is that it indicates the importance of low-lying excited-states of stable odd-*N* and/or odd-*Z* nuclei in the initiation of LENR phenomena provided that the detailed geometry of nucleon positions is taken into account.

Dark Gravity theories are extensions of General Relativity with a stable anti-gravitational sector

J.P. Petit, Twin Universe cosmology, *Astrophys. Space Sci.* Vol. 226, pp 273, 1995, and many other articles
 F. Henry-Couannier, Discrete symmetries and General Relativity, the Dark Side of Gravity, *Int.J.Mod.Phys.* vol. A20, no. NN, pp. 2341-2346, 2004.
 F. Henry-Couannier, Dark Gravity, *GJNFR A*, Vol 13, Issue 3, pp 1-53, 2013
 S. Hossenfelder, *Phys. Rev. D* 78, 044015, 2008.
 M. Milgrom, Matter and twin matter in bimetric MOND, *MNRAS* 405 (2), pp 1129-1139, 2010.
 F. Henry-Couannier, Do dark gravity theories predict ... LENR, *Rossi's Journal of Nuclear Physics*, 2014.

Henry-Couannier
 Frederic

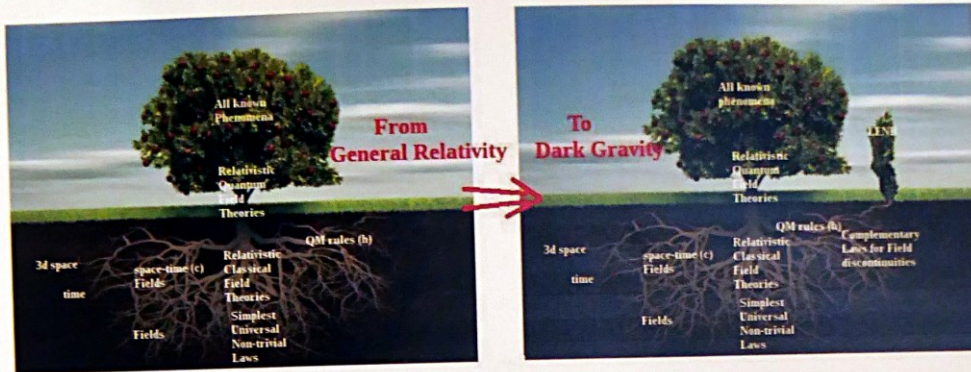
Aix-Marseille University

From Dark Gravity to
 LENR

- gr-qc/0610079 gr-qc/0410055
 - Rossi JoNP Feb 2014

In DG, Time reversal is really treated as a discrete symmetry

- Coherent with a unitary choice for time reversal in QFT \Rightarrow Negative energy fields
- Two sided (Janus) gravitational field : Negative energy fields are on the other side of the universe repelling our side matter \Rightarrow very rich new phenomenology, alternative to Dark Matter and Dark Energy...

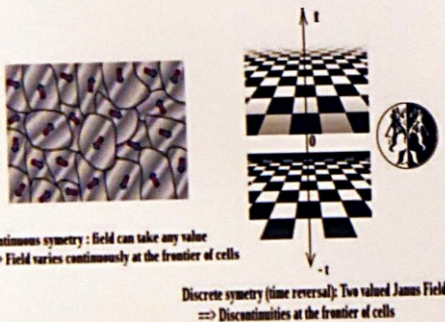


Notice: Fields assumed to vary continuously

Problems: QM and GR are not compatible

- Weird non trivial choice for Time reversal (Anti-Unitary)
- QM principles appear completely arbitrary and weird

- \Rightarrow GR is modified to be invariant under time reversal \Rightarrow discontinuities are natural
- \Rightarrow Modified GR in the bulk + laws for Field discontinuities at domain frontiers
- \Rightarrow Hopefully the new GR will be more compatible with QM
- \Rightarrow QM rules can be derived from more fundamental non local laws for discontinuities
- \Rightarrow A new tree: LENR phenomena directly following from field discontinuities



Field discontinuities ideal to explain LENR

3 correlated miracles :

- Excess Energy
- Transmutations and fusion
- Strange "particles" !
- Variable size
- Charged and magnetic yet propagate through matter
- Luminous
- Temperature discontinuity at surface
- Anomalous inertia
- Triggering transmutations ..

Step 1 : Universal trigger is an electrical discharge \Rightarrow local transient concentration of charges

Step 3 : Recovering neutrality the mlb implodes and crushes its content

Step 2 : above a potential threshold : a discontinuity trap \Rightarrow "strange" object stable in vacuum is a micro lightning ball

Fast collapse:
 Temp increases
 mlb "evaporates"

Slow collapse:
 mlb radiates and remains $< 10000^\circ\text{K}$
 up to huge densities:
 multibody nuclear reactions can start

ICCF-19
 International Conference on
 Condensed Matter Nuclear Science

TSEM

tipografia toffanin
 soluzioni per comunicare

Temperature Discontinuity

Shallow ground breaking conclusion: a melting icebergs left for mib. (c) The hole is fairly close for a process that is at dissolving a material with a melting of 2000 degrees centigrade and projects at velocity. In fact, when a speed is set up to determine the thermal gradient at the edge of the hole, one cannot be surrounding conclusion: either a gradient of 2000 degrees centigrade per meter exists here, or this is a non thermal event

mlb fast collapse

Fast input of electrons
 \Rightarrow Fast collapse
 \Rightarrow Radiative cooling not effective enough
 \Rightarrow Temperature rises
 \Rightarrow Particles gain enough kinetic energies to escape
 \Rightarrow Fast "evaporation" or "explosion" of the mlb
 \Rightarrow Origin of Plasma events is not nuclear but compression work of discontinuity turned into radiations

mlb slow collapse

Slow input of electrons (exponential)
 \Rightarrow slow collapse
 \Rightarrow small mlb, less efficient radiative and slow
 \Rightarrow Temperature does not become too much
 \Rightarrow Kinetic energies do not allow particles to escape
 \Rightarrow Huge densities and pressure (up to the microsphere, white dwarf T)
 \Rightarrow All mlb but fastest ones, stay as even because nuclear multibody nuclear reactions, due to the screening effect of the electron cloud
 \Rightarrow Eventually, small particles leave free path inside mlb
 \Rightarrow Very low rates of high energy alpha, beta, gamma, neutrinos

The Atom's Temperature

Daniel S Szumski Independent Scholar Davis, CA, USA DanSzumski@gmail.com

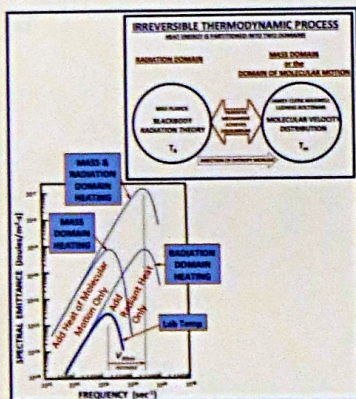
Temperature is a Derivative

By convention(1) it is the rate of radiation emittance from any material body expressed as T , or more practically, $T_m - T_e$.

Max Planck's Theory - It is uniquely defined by a temperature-specific, equilibrium blackbody spectrum, which is identical in the interior of all material bodies at the same temperature, regardless of their composition, and as we will see, regardless of their size. Max Planck(1) described the blackbody's equilibrium spectra, and in so doing introduced the quantum into physics.

Maxwell-Boltzman Theory - Temperature also has foundations in molecular motion. It was Helmholtz's great contribution to physics that heat reduces to motion. Planck places this understanding on an equal footing with James Clerk Maxwell's treatment of light as electromagnetic waves. The Maxwell-Boltzman equation (2,3) for an ideal gas's molecular velocity distribution expresses this theory's fundamentals.

Scientific Status - There has been no theoretical framework that unites these two theories. Szumski(4) has proposed a *Theory of Heat* having two temperatures, one for the radiation domain, and another for the domain of molecular motion, or what is called the mass domain. It is a non-equilibrium theory that recognizes heat transfer between the mass and radiation domains, and is elegant in the way that the two temperatures can be separated in a far-from-equilibrium manner.



Mathematical Foundations - The description of temperature as a measure of heat content lie in the probabilistic domain of statistical mechanics.

Planck's radiation form - The heat energy is contained entirely in the photonic(radiation) domain. The equilibrium state's statistics are derived from the energy distribution of harmonic oscillators.

Maxwell-Boltzman form - Heat energy is entirely in the mass domain. The statistical distribution of molecular velocity in an ideal gas is distributed according to the Maxwell distribution.

Scientific Question - Because these laws are statistical, there should be limits to their validity as the number of participating energy units decreases. Here we will consider the limiting case where the statistical foundations of the Second Law transition from probabilistic to wholly deterministic. It is in this limit, that we will enter the domain of the thermodynamically reversible process.

Photon Absorption is a Two Step Process

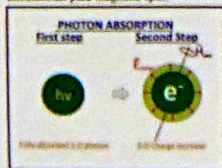
Our model of photon absorption needs to be broadened to include photon transition from its reversible state to its irreversible state.

Theory

Photon is a one-dimensional quantity, traveling in space with no loss of energy or change in its entropy. In its 1-D state, the photon is a reversible thermodynamic process, and remains so until the first instant that it encounters an electron.

First step - the photon is wholly absorbed into the electron but retains its identity as a reversible process.

Second Step - the photon evolves into the electron's three dimensions. The electrical and magnetic components decouple, and the electrical vector evolves to three-dimensional charge (with its dielectric loss), and as a consequence, enters the domain of irreversible thermodynamics. The magnetic vector on the other hand has no three-dimensional equivalent, remains one-dimensional, and contributes to the electrons one-dimensional para-magnetic spin.

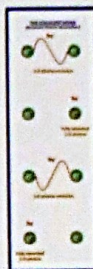


References

- [1] Planck, M., "Verhandlungen der Deutschen Physikalischen Gesellschaft", vol. 2, 237, 1900, or in English translation: *Planck's Original Papers in Quantum Physics*, Volume 1 of *Classic Papers in Physics*, H. Kragens ed., Wiley, New York, 1972.
- [2] Maxwell, J.C., (1892) *A Treatise on Electricity and Magnetism*, Clarendon Press, Oxford.
- [3] Boltzman, L., (1964) *Lectures on Gas Theory*, Translated by Stephen G Brush, University of California Press, Berkeley.
- [4] Szumski, D.S., "Consequences of partitioning the photon into its electrical and magnetic vectors upon absorption by an electron, *Proc. SPIE 8832*, The Nature of Light: What are Photons? V. 88320E (October 1, 2013).
- [5] Feynman, R.P., *QED, The Strange Theory of Light and Matter*, Princeton, New Jersey: Princeton University Press, 1988.

Nothing requires that the electron Evolve to 3-D

Consider the possibility that it is immediately re-emitted in precisely the state that had undergone that first step of photon absorption.



Emitted Photon can be emitted, still 1-D, and still in its reversible thermodynamic state. But let's go one step further and allow this emitted photon to undergo first step absorption by a second electron...and then be re-emitted still as 1-D, and re-absorbed by the first electron, and so on. We have just arrived at the quantum electrodynamic(QED) description of a covalent bond(5). Its photon energy is locked between two electrons, and remains unchanged indefinitely. It too, is a wholly reversible thermodynamic quantity, existing without any losses, and with no change in its entropy condition.

X-ray and Gamma Photons can exist in a similar way between nuclei in Mossbauer resonant bonds.

Temperature of the Reversible Thermodynamic Process

The kinetic energy goes to zero, leaving only radiation domain energy.

Irreversible process - Heat energy storage is divided between the mass and radiation domains, and the process is of a statistical nature.

Reversible process - There is no kinetic energy, and therefore, no mass domain energy storage. The motion of material particles, and the statistical uncertainty that it introduces, is foreign to reversible thermodynamics.

Covalent Bonds and Mossbauer Resonant Bonds - are thermodynamic quantities, and are temperature specific in their evolution. Our observation that we are dealing with reversible thermodynamics does not change our definition of temperature. It is still the derivative expressing the total radiant emittance from a mass particle per unit time.

Temperature of the Covalent Bond - Temperature is proportional to its emittance, $K(\nu)$, measured as the photon energy, $h\nu$, times the frequency, ν , of the individual emissions, but with the emittance of either electron occupying only one half of the process time.

$$(1) \quad T \propto \frac{1}{2} K(\nu) \cdot \nu = \frac{1}{2} h \nu^2$$

And, for nuclei in Mossbauer resonance:

$$(2) \quad T \propto \frac{1}{2} K(\nu) \cdot \nu = \frac{1}{2} h \nu^2$$

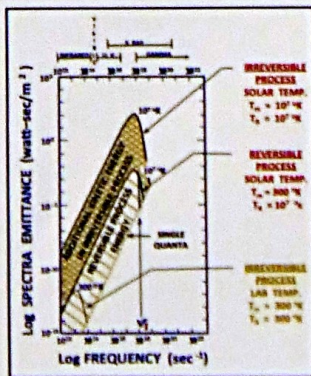
We can compare these result to Planck's irreversible thermodynamic process temperature:

$$(3) \quad T \propto \int K(\nu) d\nu = \int h \nu \frac{1}{e^{\frac{h\nu}{kT}} - 1} d\nu$$

where: $K(\nu)$ is the blackbody spectral emittance; the factor $\frac{1}{e^{\frac{h\nu}{kT}} - 1}$ is the conversion factor: per m^2 , and the statistical representation in (3) includes both radiation domain energy, and molecular motion. Equations (1) and (2) are infinitesimal subsets of Equation (3).

Observations

- Equations (2) and (3) are precise definitions, that can be misleading. The energy quanta involved in these temperature definitions cannot exist without the very structured antecedent (lower frequency) spectral distribution that has to be filled before these quanta can exist. The figure illustrates this. In this Theory of Heat the distribution of reversible process energy accumulates sequentially as T_e increases, while T_m remains constant. In this illustration, T_m equals 300 °K as T_e increases in quantum increments from 300 °K to 10³ °K.



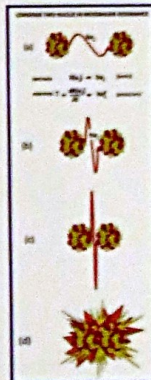
- Secondly, the energy difference required to affect equivalent temperatures in a reversible and irreversible process is almost unbelievable. Consider the solar core temperatures conditions shown in the Figure. The irreversible thermodynamic process requires five orders of magnitude more energy than the reversible process. This is the observed difference in energy requirements for fusion in the Tokamak, and in our cold fusion reactors.
- The efficiency in the reversible process arises only because it by-passes the enormous kinetic energy requirements of the irreversible process. Cold fusion exploits this advantage.

Consequence of Solar Core Temperatures

This theory of nuclear temperature provides plausible explanations for overcoming the coulomb barrier, and for the surface cracking observed in cold fusion electrodes.

Assumption - Covalent electrons and Mossbauer resonant nuclei share a single photon.

Consequence - As photon energy increases through X-ray, Soft Gamma, and Gamma energies the operative distance between electrons and nuclei pairs decreases. Do you see how this electro-magnetic force could become operative in overcoming the coulomb barrier in a cold fusion device.



QED calculations - show that the shared, intra-nuclear, radiation domain energy is sufficient to sponsor fusion, not only between two deuterons, but between much heavier nuclei.

Frequency	Wave Length	Irreversible Process Temp.	Energy Range	Energy	Comments
(1/λ)	(m)	(°K)		(MeV)	
10¹⁵	10⁻⁹ m	10⁴	0.01		
10¹⁷	10⁻¹¹ m	10⁶	Soft X-ray	1.25keV	
10¹⁸	10⁻¹² m	10⁷	Gamma (outer nucleus)		
10¹⁹	10⁻¹³ m	10⁸	Gamma (inner core)	1.2MeV	deuterium fusion
10²¹	10⁻¹⁵ m	10¹⁰	Gamma (superheavy nucleus)	100MeV	γ-process
10²³	10⁻¹⁷ m	10¹²	Gamma (nuclear)	1000MeV	γ-process

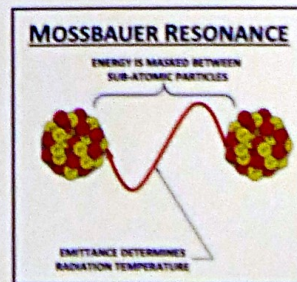
Nickel covalent radius: 1.24x10⁻¹⁰m
Hydrogen covalent radius: 0.71x10⁻¹⁰m

In Summary

Recall how the initial ignition energy was accumulated. It is the waste heat of random deuterium motion that is harvested by the metal hydride lattice, and stored there as resonant bond energy. This flux of chemical free energy into the lattice creates resonant photons having ever increasing energy storage. This is the LANP model's forcing function.

Irreversible Process - The Atom's Temperature is a statistical measure consisting of both random molecular motion, and radiant energy emittance.

Reversible Process - The Atom's temperature is determined precisely by the frequency of a single photon shared between two nuclei. The radiant emittance of each atom specifies that atom's temperature. The motion of material particles, and the statistical uncertainty that it introduces, is foreign to reversible thermodynamics. The atom's true temperature is masked from our observation.



Surface cracking in electrodes could be explained by this model. For instance, it could be the result of competition between dramatically increased surface tension due to decreasing lattice distances in the electrode's near surface layers, and the unaffected bulk of the electrode. It might also be possible that the volume of the electrode is decreased.

Theoretical prerequisites for creating cold fusion reactor

David Davidyan, Igor Danilov, Rafael Tumanyan, Vanush Davtyan
Armenian Technological Academy, Yerevan, Armenia

Introduction

The paper proposes a theoretical model which explains the energy output in cold fusion reactions, while using nickel and copper. The technique, presented by the authors, allows to determine what other isotopes of chemical elements can be used to optimize the energy output. The results can be used to create a source of energy for industrial purposes. Cold fusion is considered by the example of metal Ni and Cu.

$\text{Ni} + \text{p}$ (proton) + E_a = unstable isotope Cu, which decays with energy release.

Where there is E_a - the activation energy is necessary to penetrate proton into the nucleus of nickel.

The reactions Ni with proton

Natural Nickel contains 5 stable isotopes:

^{58}Ni (68.27 %), ^{60}Ni (26.10 %), ^{61}Ni (1.13 %), ^{62}Ni (3.59 %), ^{64}Ni (0.91 %).

All information about Isotopes are by [1], [2].

^{58}Ni (68.27 %) + p = ^{59}Cu half-life of 81,5 s
with the isotope mass (Atomic mass unit) 58,9394980

^{60}Ni (26.10 %) + p = ^{61}Cu half-life of 3,333 h.
with the isotope mass (Atomic mass unit) 60,9334578

^{61}Ni (1.13 %) + p = ^{62}Cu half-life of 9,673 m.

with the isotope mass (Atomic mass unit) 61,932584

^{62}Ni (3.59 %) + p = ^{63}Cu stable

^{64}Ni (0.91 %) + p = ^{65}Cu stable

^{59}Ni (half-life of 100,000 years) + p = ^{60}Cu

Half-life of 23,7 m. isotope mass (Atomic mass unit) 59,9373650

The reactions Cu with deuterium nucleus

Natural copper consists of two stable isotopes –

^{63}Cu (69 %), ^{65}Cu (31 %),

We are interested in the reaction with the formation of an unstable isotope of Zn, which decays with the release of energy:

^{63}Cu (69 %) + pn (proton with neutron - deuterium nucleus) =

^{65}mZn The excitation energy 53,928 KeV, Half-life of 1,6 μs , Spin and parity of the nucleus 1/2-

Results

Effect of cold fusion was observed in two experiment. At one the energy release was observed in the interaction of deuterium with a copper wall (as a side effect in the study of ion-molecule reactions [3]). In the second - nickel with hydrogen (like Mr. A. Rossi [4]). According to the assumption of Igor Danilov (St. Petersburg) has reverse tunnel effect. Thus formed isotopes with short lifetimes, which was bought by release energy. Currently, work is underway to create an industrial power station.

References

- [1] G. Audi, A.H. Wapstra, and C. Thibault (2003). «The AME2003 atomic mass evaluation (II). Tables, graphs, and references.». Nuclear Physics A 729: 337–676. DOI:10.1016/j.nuclphysa.2003.11.003.
- [2] G. Audi, O. Bersillon, J. Blachot and A. H. Wapstra (2003). «The NUBASE evaluation of nuclear and decay properties». Nuclear Physics A 729: 3–128. DOI:10.1016/j.nuclphysa.2003.11.001.
- [3] R.T. Malkhasyan, G.N. Sargsyan, E.S. Zurkin, V.G. Davtyan. Secondary ion-molecule reactions of ions D_3^+ with noble gases. Abstracts on 2-nd All-Union Conference on the gas-phase kinetics of 1978. Chernogolovka-Yerevan, pp 43–46.
- [4] Rossi Andrea, Patent 20110005506 - METHOD AND APPARATUS FOR CARRYING OUT NICKEL AND HYDROGEN EXOTHERMAL REACTION, 13.01.2011, <http://patentscope.wipo.int>

Role of dopants in achieving high deuterium loading in palladium during electrochemical experiments



O. Dmitriyeva, D. Knies, S. Hamm, R. Cantwell, M. McConnell
Coolscience LLC, Boulder, CO 80301 U.S.A
ICCF-19, April 13-17, Padua, Italy

Low Energy Nuclear Reaction - Necessary Conditions

- High D-Pd loading >90% [1,2]
- Presence of promoting impurities [1,2,3,]
- Flux [2]
- Surface morphology [1,3]

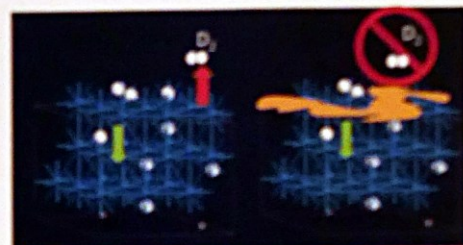
This discussion focuses on D/Pd loading and impurities. for Flux and Morphology see S.Hamm and D.Knies presentations

- [1] E. Storms, The science of low energy nuclear reaction, Singapore: World Scientific Publishing Co. Pte. Ltd., 2007
[2] M. McKubre, S. Crouch-Baker, R.C. Rocha-Filho, S.I. Smolensky, and F.L. Tarasick, "Isothermal flow calorimetric investigations of the D/Pd and H/Pd systems," Journal of Electroanalytical Chemistry, vol. 368, p. 35, 1994.
[3] V. Vukobratovic, "Material Science on Pd-D System to Study the Occurrence of Excess Power", ICCF-14, Washington DC, 2008

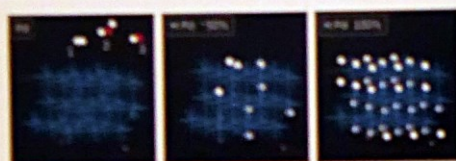
Electrolytic Loading (continue)

How can we fill the "leaky bucket" above 75%?

Block the escape path by coating the surface, while leaving Pd islands to absorb deuterium



Deuterium Loading in Palladium



Possible sources of deuterium:
1) D₂ gas
2) Heavy water D₂O
3) OD ions

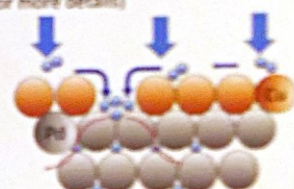
100% deuterium loading in bulk palladium is possible when deuterium surface coverage is maintained at 100% - not the case under standard conditions



Baranowski curve (change of resistance as a function of loading)
← equilibrium limit

Getting to the loading levels above 75% requires special conditions

Presence of impurities focuses more current through exposed Pd area which will deliver more deuterium to the surface where it gets absorbed, while D₂ desorption is suppressed over the covered areas.
(See S. Hamm and D. Knies presentations for more details)



Partially blocking the deuterium escape path will increase the deuterium surface coverage on exposed Pd → results in an increase of bulk loading.

Electrolytic Loading

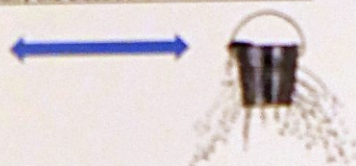
Deuterium provided to the surface through Volmer reaction:



Deuterium is leaving the surface through Tafel reaction:



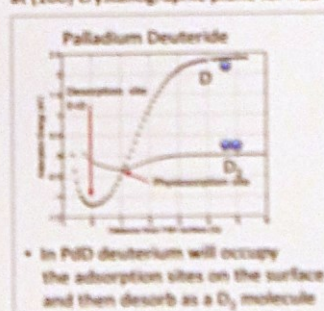
We can fill up only 75% of a "leaky bucket", which is consistent with equilibrium deuterium pressure at max R/R0 of the Baranowski curve, unless we modify the electrochemical environment!



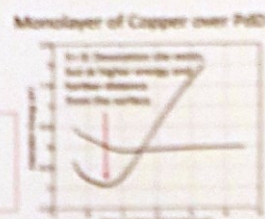
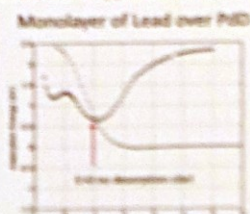
Density Functional Theory (DFT) modeling

Why the desorption is suppressed?

Calculations on the Lennard-Jones Potential for deuterium adsorption/desorption at (100) crystallographic plane for PdD and PdD covered with copper and lead films.



- In PdD deuterium will occupy the adsorption sites on the surface and then desorb as a D₂ molecule



- E(PdD) < E(Cu on PdD) < E(Pb on PdD)
- Cu or Pb film has weak or no deuterium desorption.

Conclusions

- Non-uniform coating of Pd surface
 - Modifies the desorption path → disables Tafel reaction
 - Increases current density through Pd islands → increases H/D coverage and promotes high levels of bulk loading
- Density Functional Theory simulations
 - Explains the energetics of adsorption/desorption process on modified surfaces
 - Provides the framework for screening additional materials: Fe, Ag, Zn, Bi, Ti, V, In, Mn, Sn, Si and Al (including oxides)
- Future work
 - Photolithographic patterning of the surface which will control the size of the exposed palladium islands

Introduction

In many crystals with sufficient anharmonicity, a special kind of lattice vibrations, namely, **discrete breathers (DBs)** can be excited either thermally or by external triggering, in which the amplitude of atomic oscillations greatly exceeds that of harmonic oscillations (phonons). Coherency and persistence of large atomic oscillations in DBs may have drastic effect on quantum tunneling due to **correlation effects** discovered by Schrödinger and Robertson in 1930. We argue that DBs present the most natural and efficient way to produce correlation effects due to time-periodic modulation of the potential well width (or the Coulomb barrier width) and hence to act as breather 'nano-colliders' (BNC) triggering low energy nuclear reactions (LENR) in solids. Tunneling probability for deuterium (D-D) fusion in 'gap DBs' formed in metal deuterides is shown to increase with increasing number of oscillations by **~190 orders of magnitude** resulting in the observed LENR rate at extremely low concentrations of DBs.

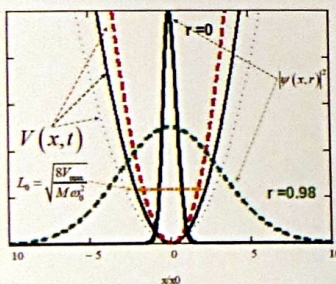
Schrödinger-Robertson uncertainty relation (1930):

$$\sigma_x \sigma_p \geq \hbar_{ef}^2 / 4 \quad \hbar_{ef} = \frac{\hbar}{\sqrt{1-r^2}} \quad r = \frac{\sigma_{xp}}{\sqrt{\sigma_x \sigma_p}} \quad \text{- correlation coefficient}$$

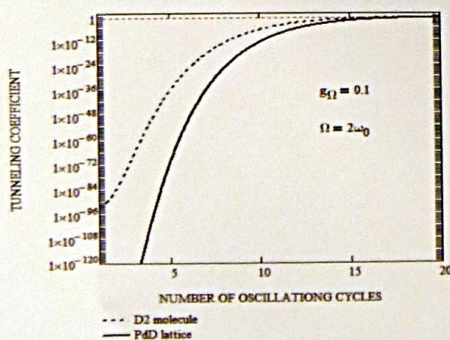
Increase of Tunneling coefficient with increasing **correlation coefficient** [Vysotskii et al (2010)]:

$$G_{r \neq 0} \approx \exp \left\{ -\frac{2}{\hbar_{ef}} \int_{r_1}^{r_2} dr \sqrt{2\mu(V(r) - E)} \right\} = (G_{r=0})^{\sqrt{1-r^2}} \xrightarrow{|r| \rightarrow 1} 1 \text{ even if } E \ll V_{\max},$$

Breather-induced time-periodic action on the potential well and the tunneling coefficient



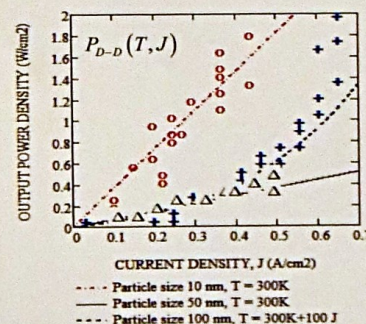
Time-periodic parabolic potential $V(x,t)$ at different moments of time corresponding to the initial (solid black), minimal (dash red) and maximal (dot blue) well width. Probability density for the particle localization in the well and in the sub-barrier region is shown schematically for uncorrelated state $r=0$ (solid black) and for strongly correlated state $r=0.98$ at the times of the maximal coordinate dispersion (dash green). [Vysotskii et al (2010)]



Tunneling coefficient increase with increasing number of the breather modulation cycles evaluated for two D-D equilibrium spacings: in a D₂ molecule ($L_0 = 0.74 \text{ Å}$) and in the PdD crystal ($L_0 = 2.9 \text{ Å}$) [1].

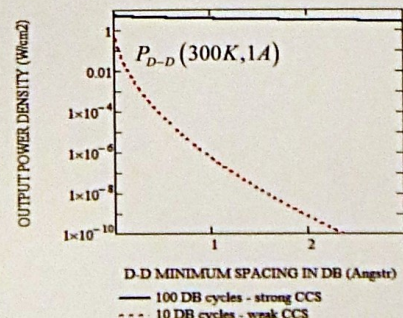
Breather-induced LENR energy production

Experiment vs. Model [1]: $D + D \rightarrow {}^4\text{He} + 23.8 \text{ MeV}_{\text{lattice}}$



LENR output power density according to the model [1] as a function of electric current density at constant T and $T=300\text{K}+100\text{J}$. Experimental data [Storms, 2007] are shown for comparison. \circ - Bush (constant T), Δ - Storms (constant T), $+$ Aoki et al (T grows with J).

$$P_{D-D}(T, J) = K_{DB}^J (E_{DB}^*, T, J) \times 23.8 \text{ MeV}_{\text{lattice}}$$



LENR output power density as a function of the tunneling D-D spacing at strong and weak Coherent Correlated States (CCS) formed after ~10 and ~100 DB cycles, respectively [1].

[1] Dubinko (2015) <http://arxiv.org/abs/1503.09119>

Conclusions/outlook

- The present model explains all the salient LENR requirements: (i) high loading of D within the Pd lattice as preconditioning needed to prepare PdD crystallites with appropriate *density of states* (DOS), and (ii) the triggering by D flux or electric current, which facilitates the DB creation by the input energy transformed into the lattice vibrations.
- The proposed mechanism of CCS formation near the gap DBs requires sufficiently broad phonon gap that is not observed below the critical D loading ~0.83 examined so far. Further investigations of DOS and DBs in the extreme conditions of LENR are required.
- Atomistic modeling of DBs of various types in metal hydrides/deuterides is an important outstanding problem since it may offer the ways of engineering the nuclear active environment.

Search for low-energy x-ray and particle emissions from an electrochemical cell

Dennis Pease¹, Orchideh Azizi¹, Jinghao He¹, Arik El-Boher¹, Sango Bok², Cherian Mathai², Shubhanga Gangopadhyay², Katesh Katti³, Kavita Katti³, Stefano Lecci⁴, Vittorio Violante⁴ and Graham Hubler⁴
¹The Sydney Kimmel Institute for Nuclear Renaissance (SKINR), Department of Physics and Astronomy, University of Missouri, Columbia, MO, USA
²Department of Electrical Engineering, University of Missouri, Columbia, MO, USA
³Department of Radiology, University of Missouri, Columbia, MO, USA
⁴ENEA Research Center, via E. Fermi 45, 00044 Frascati (Rome), Italy

Abstract

Several theories explaining anomalous heat production predict the emission of low energy x-rays and/or MeV alpha particles from Pd cathodes in electrochemical cells. Such radiation, however, is not detectable from outside of a standard electrochemical cell due to absorption in the electrolyte and/or cell walls. A custom cell was therefore assembled which permits x-rays of energy ≥ 1 keV to pass through a thin cathodic membrane and enter into an Amptek XR-100CR Si-Pin diode detector. This same test cell also potentially allows any emitted MeV alpha particles to be detected via impact induced fluorescence of Pd-K α (21.2 keV) and Pd-K β (23.8 keV) x-rays. The detection of x-ray emissions from electrochemical cells permits the mechanism(s) for anomalous heat production to be investigated with great sensitivity. As an example, the above x-ray detector allows 1 keV x-rays to be readily detected at emission rates of less than one per second that corresponds to a heat sensitivity of < 0.2 Femtowatts.

A series of experiments have been performed using custom electrolytic cells with two types of thin membrane cathodes having 0.1M LiOD electrolyte on one side and air on the other. One type of cathodic membrane used 1 μ m silicon nitride coated with 200 nm of platinum (Pt) and palladium (Pd). Three different electrolysis co-deposition methods were used:

- 1) D / Pd from Pd anode;
- 2) D / Pd from Pd salt solution;
- 3) D / Pd from Pd nanoparticle suspension.

The other type of cathodic membrane used a 30 μ m palladium foil.

X-ray spectral data from 1 to 35 Kev was collected for over a year using the above two test cells. During this time no x-rays above background levels were detected from the cells.

Motivation = Data Deficit

- Low energy emissions in electrochemical anomalous heat (AHE) experiments have never previously been thoroughly investigated in *REAL TIME* by using time-resolved detectors.
- While many theories predict low energy x-ray or MeV alpha particle emissions, there has been a fundamental *PROBLEM* in detecting them: such emissions are expected to be attenuated to undetectable levels due to absorption within the electrolyte and calorimeter structure of a standard electrochemical cell

A Summary of AHE theories and the Emissions Predicted by them

Author	Theoretical Basis for Emissions	Predicted Emissions
Hagelstein	2D fusion	1-4 keV x-rays
Takahashi	4D fusion	4 keV x-rays, MeV alphas
Kucherov	Photon stimulation of nucleus	Alpha decay, fission
Mayer	Tight molecular binding of light particles	4.7 keV x-rays
Meuhlenberg, Mills, others	Collapsed electron states	~4 keV x-rays

Problem Solution = Thin Cathode

- Construct a modified electrolytic cell that permits emissions of low energy x-rays to be detected with very little attenuation by using a thin membrane cathode. (Note: Si₃N₄ membranes are from Silson LTD)
- Deposit a thin Pd cathode on the surface of a 1 μ m thick Si₃N₄ membrane. (Known Issue: Pd film tends to delaminate due to its large volume change as it is loaded with Hydrogen or Deuterium.)
- Leverage unpublished data*.
- Reduce risk of delamination by using co-deposition of 200 nm of Pd and Pt on a 1 μ m Si₃N₄ membrane.

*In 2005, Energetics detected 10% excess heat in four cells with a Pd anode and Pt cathode in which Pd was gradually deposited on the Pt cathode during electrolysis.

Advantages of the Above Technique

- Potential sensitivity to detect nuclear emissions corresponding to ~1 Femtowatt of anomalous heat.
- Ability to directly detect 1 to 30 keV x-rays.
- Possible detection of MeV alphas via x-ray induced fluorescence generated from particle impacts on Pd, Pt, and Si cathode structures.
- Enables direct testing for energetic emissions predicted by many different AHE theories including non-nuclear proposals.

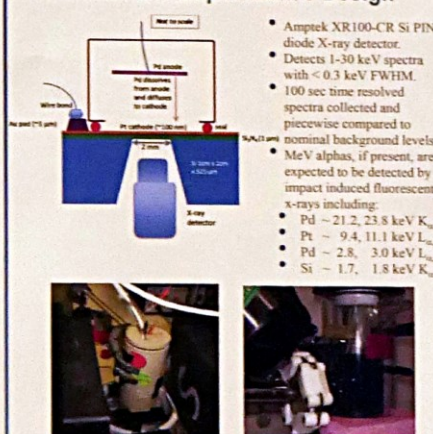
Problem Solution (cont.)

Disadvantage of the above Technique

- The novel thin film anode/cathode/electrolyte combinations that were used have not previously been demonstrated to reliably produce excess heat*

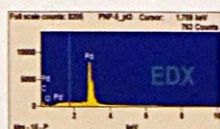
*However, the Pd anode/Pt cathode did produce 10% excess at Energetics in 2005 (unpublished) and Pd NP in electrolyte produced excess heat at SKINR in 2014-5 (see poster at ICCF19). Lastly, Pd foil loaded from just one side is not known to yield AHE but it certainly does when charged from both sides.

The Membrane Experiment's Design



The Membrane Experiment's Approach

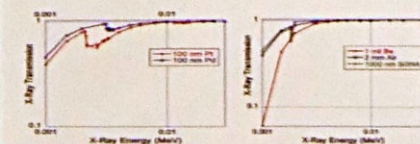
In situ Pd deposition using PdNp suspension



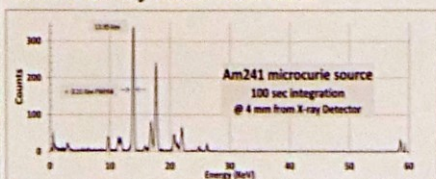
The Membrane Experiment's Sensitivity

- Most calorimeters have a sensitivity of about 1 to 10 mW.
- If AHE is active much of the time, but only at Micro, Nano, or Picowatt levels, then a standard calorimeter would be completely unable to detect such low levels of power output.
- However, if 2 keV x-rays are emitted at ~1 Hz into a background <0.2 counts per second, then the corresponding heat sensitivity by detecting x-rays is <100 Attowatts*.
- The above implies an excess power sensitivity improvement of 10¹³ relative to conventional calorimetry!

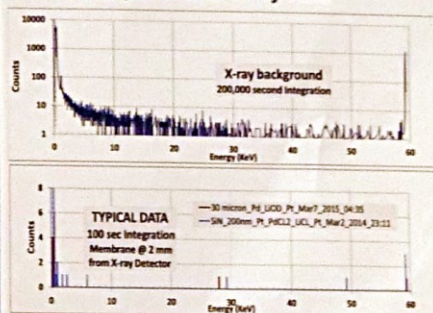
*The above sensitivity calculation included x-ray attenuation (see graphs below) caused by passing through 100 nm Pt, 100 nm Pd, 1 μ m Si₃N₄, and 2 mm Air. It also included the loss of sensitivity due to background x-ray counts.



SKINR's x-ray Calibration Data



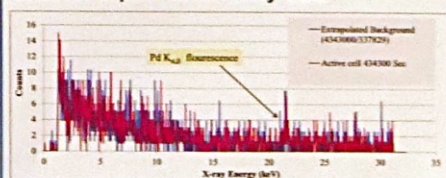
SKINR's Experimental x-ray Data



SKINR's Data Summary

Cathode	Anode	Electrolyte	C current density (mA/cm²)	X-ray detector model (off)	Duration Days
Si ₃ N ₄ 100 nm Pt	Pt	0.1M LiOD	0.01-0.1	XR100Glass cell	10
Si ₃ N ₄ 100 nm Pd	Pd	0.1M LiOD	0.1-1	XR100Glass cell	5
Si ₃ N ₄ 100 nm Au	Pd	0.1M LiOD	0.5-2.5	XR100Glass cell	11
Si ₃ N ₄ 100 nm Pt	Pd	0.1M LiOD	0.25-2	XR100Glass cell	8
Si ₃ N ₄ 100 nm Pd	Pd	0.1M LiOD	0.25-4	XR100Glass cell	40
Si ₃ N ₄ 100 nm Pt	Pd	0.1M LiOD	0.1-4	XR100Glass cell	7
Si ₃ N ₄ 100 nm Pd	Pd	0.1M LiOD	0.1-4	XR100Glass cell	12
Si ₃ N ₄ 100 nm Pd	Pd	0.1M LiOD	0.1-4	XR100Glass cell	1
Si ₃ N ₄ 100 nm Pt	Pd	0.1M LiOD	0.1-4	XR100Glass cell	28
Si ₃ N ₄ 100 nm Pd	Pd	0.1M LiOD	0.1-4	XR100Glass cell	90
Pd 30 μ m	Pd	0.1M LiOD	0.25-4	XR100 Peak cell	10
200nm Au Bulk	Pt	0.1M LiOD	0.5-10	XR100 Peak cell	20

ENEA's Experimental x-ray Data



- X-ray spectrum (1-32 keV) for Au-coated 25 μ m thick Pd foil after 5.8 days.
- The source of the Pd K α x-rays at 21.1 and 23.8 keV is known to be fluorescence caused by 100 keV gamma rays from Bi radioactive isotope in shielding materials.

ENEA's Data Summary

Cathode	Anode	Electrolyte	C current density (mA/cm²)	X-ray detector Model (off)	Duration Days
100 nm Pt	Pd	0.1M LiOD		X123Peak Cell	0.71
100 nm Au	Pd	0.1M LiOD		X123Peak Cell	0.82
200 nm Au on 25 μ m Pd	Pd	0.1M LiOD		X123Peak Cell	3.8

Conclusions

- ✓ It was hoped that this experiment would help discriminate between the many different theories trying to explain anomalous heat effect (AHE)
- ✓ No x-rays above background levels were detected at SKINR or ENEA
 - But... It is not known if AHE was present for any of the cathodes
- ✓ If the signature of AHE is low energy x-rays or MeV alpha particles, then either AHE is not active at power levels between 1 Femtowatt and ~1 mW, and was in an OFF state, and needs to be triggered, or, the cathode was in an ON state, producing low level heat with no observable low energy radiation. In the latter case, our conclusion is that *NONE* of the theories in the table are viable.
- ✓ ENEA data shows Pd K α x-ray peaks due to fluorescence induced by 100 keV Bi gamma rays emitted within shielding materials.
- ✓ The fragile Si₃N₄ membranes survived from 1 day to 3 months.
- ✓ Continuation and improvement of membrane experiments is warranted:
 - Place the membrane system in a calorimeter
 - Run 30 μ m thick Pd cathodes for longer periods
 - Add an RF antenna and RF detector in addition to the x-ray detector
 - Stimulate the cathode on the air side with RF and/or lasers

Acknowledgement:

This work was fully funded by Mr. Sidney Kimmel

Final report on calorimetry-based excess heat trials using Celani treated NiCuMn (Constantan) wires

Arik El-Boher¹, William Isaacson¹, Orchideh Azizi¹, Jingao He¹, Dennis Pease¹, and Graham Hubler¹
The Sydney Kimmel Institute for Nuclear Renaissance (SKINR), Department of Physics and Astronomy, University of Missouri, Columbia, MO, USA

Abstract

Sensitive mass flow calorimetry has been used in a series of tests to evaluate eight treated NiCuMn (Constantan) wires in a gas loading cell. The goal of this testing was to reproduce and confirm the production of excess heat when using an experimental setup similar to that demonstrated in 2013 by Dr. Francesco Celani at National Instrument's NI week and ICCF 17. Six of the eight Constantan wires used in the SKINR tests were provided by Dr. Celani and the remaining two were obtained from Mathieu Valat. Initial tests in the series closely followed the set-up, operation, and heating protocols used by Dr. Celani with a significantly modified stainless steel cell to enable the use of mass flow calorimetry. Later tests used the same modified test cell but added additional heating protocols using pulsed or highly modulated electric currents (Superwaves) to enhance loading and create additional thermal gradients within the Constantan wires. No excess heat was observed in running either the initial or later test protocols during ~200 days of testing with a calorimetric sensitivity of < 10 mW.

Methods & Materials



The wire holder

- Six Legs to support wire off form
- Grooved with two nested spirals to separate active and heater wire
- Cooled by inner core for calorimetry
- Constructed of high alumina bisque (LAVA) and fired hard.
- Mica coated glass tape used for a further thermal barrier

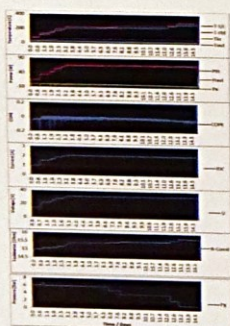


The wire holder wound with the treated Isotan 44 wire and a 32 AWG Nickel Chrome heater wire. The Pt100 RTD is in the middle of the wires.



The core assembly with leads attached just prior to insertion.

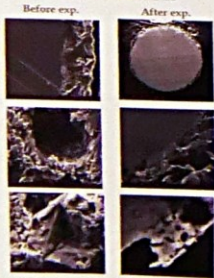
Results



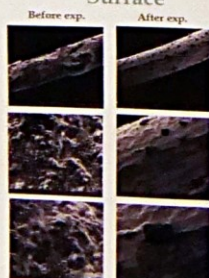
Wire number 270912B: 2 layer Wire

- 25% Hydrogen / 75% Argon Atmosphere
- DC current stepped to 2.1A
- Gas pressure lowered in steps from 6 Bara to 1.1 Bara
- Initial wire resistance 15.01 Ohm
- No excess heat observed

Cross-section



Surface



The Sulphur Question

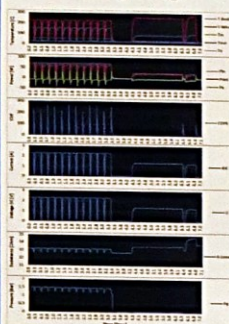


Wire number 280912A: 480 Layer Wire

Initial loading

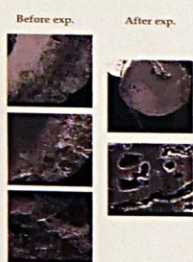
- 100% Hydrogen Atmosphere
- Initial wire resistance 13.37 Ohm
- DC current stepped up to 2.1A and then to 2.3A
- Gas pressure lowered in steps from 6 Bara to 1.1 Bara
- No excess heat observed

Power cycling

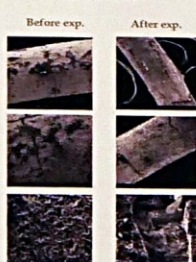


- 100% Hydrogen Atmosphere
- Hot cell pressure raised to 1.5 Bara; cold pressure about 1.2 Bara
- DC current stepped up to 2.3A for six hours and then down to 0.1A for one hour
- An error in programming power led to an approximately 10 minute disconnect between the two data files.
- De-loaded twice prior to post run
- No excess heat observed

Cross-section

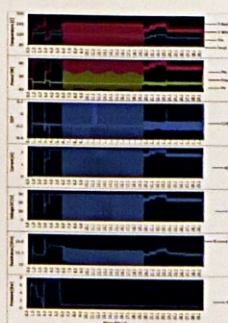


Surface

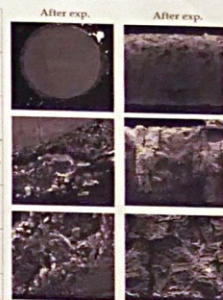


650 Layer Wire: Wire number 270912C

- 100% Hydrogen Atmosphere
- DC current stepped to 2.1A
- Gas pressure lowered in steps from 6 Bara to 1.1 Bara
- Current pulses started. 6 hours at 2.3 A followed by 1 hour at 0.1 A
- Duration of ~327 hours
- Switched to Superwave, trial and error choice of parameters for first few waves
- Final wave: 30 minute period, 1.8 A Offset, 2.1 A Average Current, 5 wave components
- Duration of ~243 hours
- Initial wire resistance 13.67 Ohm
- No excess heat found

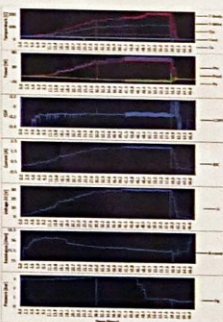


Cross-section



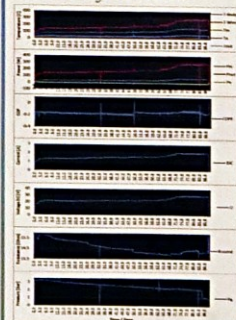
Wire number 020813: 10 Layer Wire

- This wire is from a second lot. Provided through Dr. Matthew Valat
- 100% Hydrogen Atmosphere
- DC current stepped to 2.1A
- Followed by 2.1A average current Superwave
- Gas pressure lowered in steps from 3 Bara to 1.1 Bara
- Initial wire resistance 15.01 Ohms
- No excess heat observed



Wire number 050813: 200 Layer Wire

- This wire is from a second lot. Provided through Dr. Matthew Valat
- 100% Hydrogen Atmosphere
- DC current stepped to 2.1A
- Followed by 2.1A average current Superwave
- Gas pressure lowered in steps from 3 Bara to 1.1 Bara
- Initial wire resistance 16.10 Ohms
- No excess heat observed



Conclusion

Wire Test No.	Treated Wire	Max R/R (Ohm)	Signals Used	Test Duration (Days)	Excess Heat?	Notes
1	2 layers #270912B	99.44	DC	15	No	
2	700 layers #021012A	N/A	DC	8	No	Wire burned through at defect
3	700 layers #021012A	99.77	DC	17	No	
4	480 layers #280912A	N/A	DC	7	No	
5	480 layers #280912A	95.32	DC & Pulsed DC	7	No	
6	650 layers #270912C	97.69	DC, Pulsed DC & SW	20	No	Performed with Dr. Celani in attendance
7	10 layers #020813	99.70	DC & SW	49	No	Lot 2 wire Received from Dr. Matthew Valat
8	200 layers #050813	84.08	DC & SW	90	No	Received from Dr. Matthew Valat

- ✓ Dr. Celani's wire preparation process appears to be a selective oxidation/reduction of the Nickel/Copper/Manganese wire.
- ✓ The number of layers equates to the number of oxidation cycles that the wire has been put through and correlates to a thicker layer of the surface morphology.
- ✓ Obtaining an accurate temperature reading of such a small wire is problematical.
- ✓ Resistance ratio may not be an accurate indication of loading; there have been no loading studies done for the alloy Constantan. Further, when the wire reaches temperature, there is a reduction of the Nickel oxides which affects resistance.
- ✓ Loading as indicated by pressure reduction was much better for the second lot of wires.
- ✓ No excess heat was observed in any of the trials.

Acknowledgements:

This work was fully funded by Mr. Sidney Kimmel

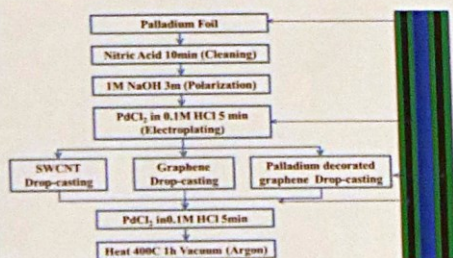
Search for excess heat in electrolysis using single-walled carbon nanotubes (SWCNT) and graphene-coated palladium cathodes

Orchideh Azizi¹, Sango Bok², Cherian Mathai², Jinghao He¹, Arik El-Boher¹, Shubhra Gangopadhyay, Dennis Pease¹ and Graham Hubler¹
¹ The Sydney Kimmel Institute for Nuclear Renaissance (SKINR), Department of Physics and Astronomy, University of Missouri, Columbia, MO, USA
² Department of Electrical Engineering, University of Missouri, Columbia, MO, USA

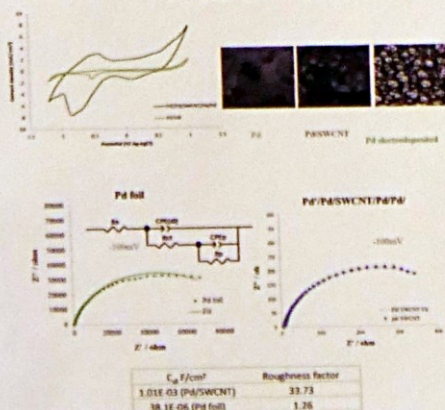
Abstract

Single-walled carbon nanotubes (SWCNTs) have emerged as a promising material for a variety of applications due to their unique electrical and physical properties. SWCNT-coated palladium (Pd) foils on both sides, provided by Andre Lipson, gave robust levels of excess heat with promising reproducibility at Energetics, ENEA and SRI in 2006-2008. SKINR has continued this effort by reproducing these cathodes via drop casting at a relatively low density of 0.1 mg/cm² using an aqueous dispersion of SWCNT onto pre-treated Pd foils. In addition, graphene coated Pd foils were fabricated and decorated with Pd nanoparticles. Over a period of two years, 20 cathodes were tested to search for excess heat in electrolysis. Only one of these cathodes showed strong excess heat production and that heat appeared in two separate bursts. The first burst lasted for about three hours and released 75 kJ of excess heat with a peak coefficient of performance (COP) of 5500% and an average COP of 3500%. The second heat burst lasted for about one and a half hours and released 13 kJ of excess heat with a peak COP of 2700% and an average COP of 1660%. Additional experimental results will be presented along with details about cathode fabrication and electrochemical characterization using cyclic voltammetry and electrochemical impedance spectroscopy. Finally, SEM and AFM images will be presented to show the surface morphology of the SWCNT-coated Pd foils before and after the testing.

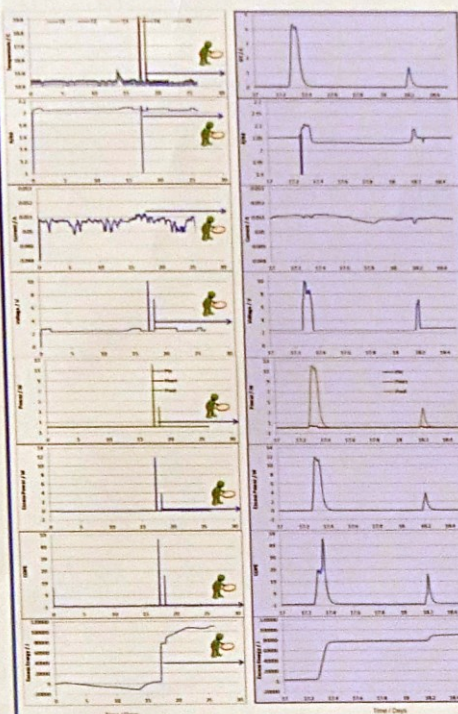
Pd/SWCNT/Pd & Pd/G/Pd Fabrication Procedure



Electrochemical characterization of Pd/SWCNT/Pd

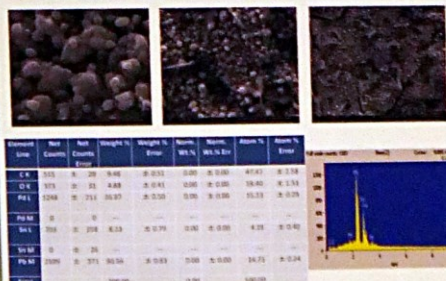


Pd/SWCNT/Pd Cathode, Excess Heat

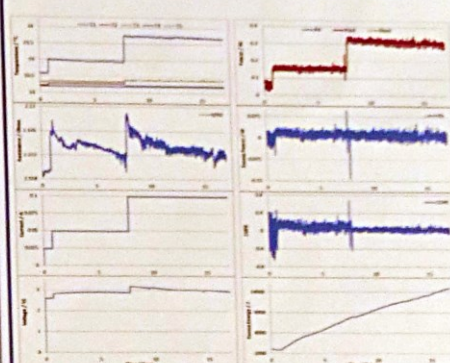


Two consecutive excess heat bursts observed during electrolysis of heavy water using a Pd-SWCNT-Pd composite cathode

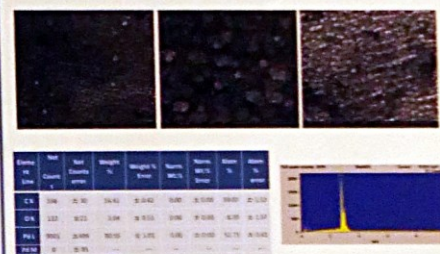
SEM and EDX results after Excess Heat



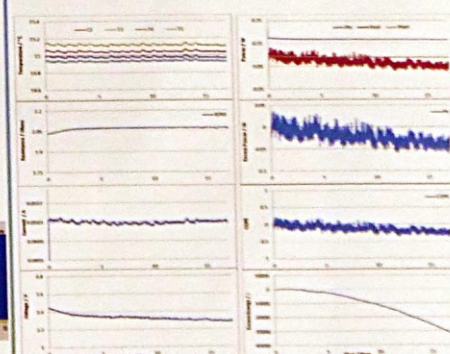
Pd/SWCNT/Pd Cathode, Without Excess Heat



SEM and EDX results without Excess Heat



Pd/ Graphene /Pd Cathode, Without Excess Heat



Conclusion

- ✓ One out of 20 cathodes produced substantial excess heat (COP 5,500%)
- ✓ Only the heat producing cathode had Sn and Pb impurities after electrolysis
- ✓ Cell voltage increases during excess heat events. This implies that there are dynamic conditions associated with electrode materials, cell impedance and electrochemical reactions
- ✓ Power spectral density (PSD) of the heat producing cathode has double peaks, similar to other cathodes which produced excess heat
- ✓ Cyclic voltammetry (CV) and electrochemical impedance spectroscopy (EIS, 1 kHz) demonstrated that SWCNT cathodes are more active, mostly due to increased surface area
- ✓ Graphene coated Pd foil decorated with Pd nanoparticle cathodes have shown no excess heat in preliminary runs
- ✓ SKINR and its collaborators plan to increase the understanding through improved control of cathode metallurgy, creating tailored surface morphologies, and comprehensive pre- and post-characterization of cathodes

Acknowledgement:

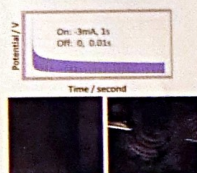
This work was fully funded by Mr. Sidney Kimmel

Abstract

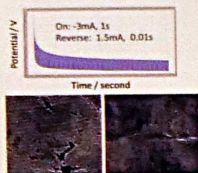
Two possible important factors which influence Anomalous Heat Effect (AHE) are:
1) the presence of micro/nano cathode surface structures; and
2) achieving high loading ratios (> 0.9 D/Pd) of deuterium (D) into the palladium (Pd) lattice.
To better understand AHE, Pd nanoparticles (PdNPs) were synthesized externally and then mixed them uniformly into $D_2O + 0.1$ M LiOD electrolyte. Subsequent electrolysis resulted in Pd nanoparticles being deposited on the surface of the palladium along with being highly loaded with D or H atoms. Post-experiment SEM images showed that the PdNPs are uniformly distributed across the surface.

Electrophoretic / Electro-deposition of Pd Nanoparticles

SEM of PdNP deposited at: Pulse current mode



SEM of PdNP deposited at: Pulse-Reverse current mode



SKINR has also studied the effect of palladium nanoparticles on H/D absorption and diffusion into palladium using a permeation electrochemical double cell using a thin palladium membrane. Hydrogen permeation efficiency, hydrogen diffusion coefficient, subsurface hydrogen concentration and total amount of hydrogen absorbed into the palladium membrane were obtained using the time-lag method.

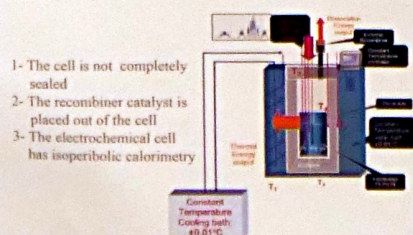
SKINR has performed electrolysis with suspensions of PdNPs at a variety of concentrations in both closed and open electrochemical cells with PdNPs. A closed cell, with an internal H_2 - D_2/O_2 catalytic recombiner never produced any excess heat. However, an open cell with an external recombiner always showed excess heat persisting for several days with an average coefficient of performance (COP) of 15 to 65 %. This excess heat was most evident at low electrolysis currents and decreased with increasing currents. The source of the anomalous excess heat measured in the open cell with an external H_2 - D_2/O_2 catalytic recombiner remains unknown and is under further investigation.

Methods & Materials

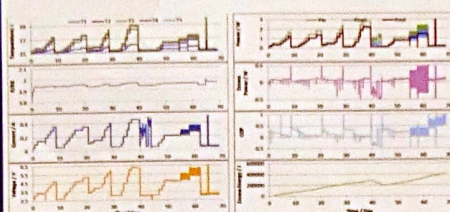
Cathode: Pd foil, 1X8 cm, 50 μ m Thickness
Rolls: from 1 mm to 50 μ m Thickness
Annealed at: 400 °C 30 min, 850 °C 60 min,
Etched: 1 min HNO_3 , 1 min 50 % Aqua Regia, 30 s HNO_3
Anode: Two Pt foils: 2x8 cm and 100 μ m Thickness
Electrolyte: Pd nano-particle suspension

Results

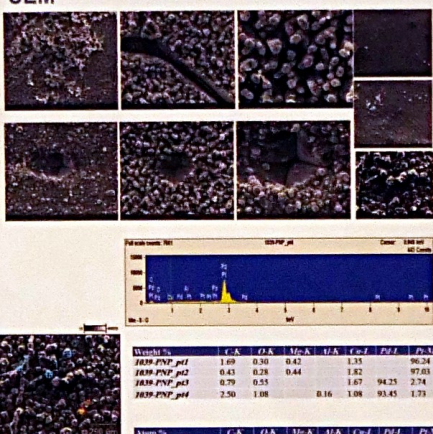
Pd Nanoparticle suspension in an electrochemical Open cell



- 1- The cell is not completely sealed
- 2- The recombiner catalyst is placed out of the cell
- 3- The electrochemical cell has isoperibolic calorimetry



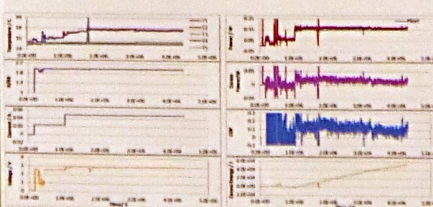
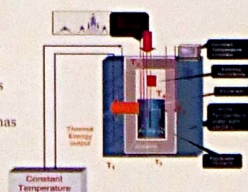
SEM



EXP	Solution	Excess Power / W	Excess Energy / J	COP	Duration / Day
1039	1X PdNP+ 0.1LiOD	0.04-0.14	4.04E+5	0.31-0.038	58
1042	1X PdNP+ 0.1LiOD	0.075-0.29	2.13E+5	0.62-0.21	27
1080	1X PdNP+ 0.1LiOD	0.05-0.048	6.23E+5	0.44-0.28	146
1085	1X PdNP+ 0.1LiOD	0.042-0.01	8.93E+4	0.31-0.05	63
1090	2X PdNP+ 0.1LiOD	0.066-0.057	1.16E+5	0.65-0.46	24
1046	0.1M LiOD	0.056-0.051	5.55E+4	0.28-0.066	8
1052	1X PdNP+ 0.1LiOD	0.08-0	4.56E+4	0.51-0	22
1056	1X PdNP+ 0.1LiOD	0.015-0	2.79E+5	0.95-0	42
1063	1X PdNP+ 0.1LiOH	0.01	1.40E+4	0.25-0	22
1057	1X PdNP+ 0.1LiOH	0.015-0.02	3.85E+5	1.0-0.25-0	55

Pd nanoparticle suspension in an electrochemical Hybrid cell

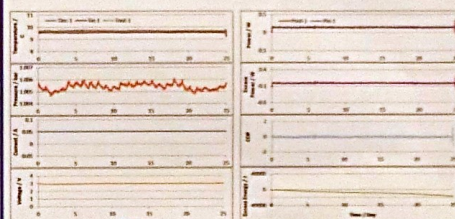
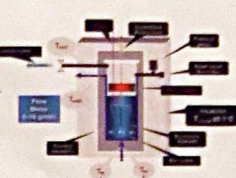
- 1- The cell is not completely sealed
- 2- The recombiner catalyst is placed inside the cell
- 3- The electrochemical cell has isoperibolic calorimetry



EXP	Solution	Excess Power / W	Excess Energy / J	COP	Duration / Day
1087	1X PdNP+ 0.1LiOD	0.034-0.035	5.81E+4	0.28-0.25	50
1092	1X PdNP+ 0.1LiOD	0.015-0	8.91E+4	0.18-0	18
1063	1X PdNP+ 0.1LiOH	0.05-0	8.34E+5	0.13-0	39

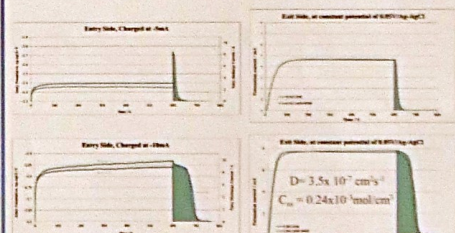
Pd Nano Particle suspension in an electrochemical Closed cell

- 1- The cell is completely sealed
- 2- The recombiner catalyst is placed inside the cell
- 3- **Type A:** The electrochemical cell has mass flow calorimeter
Type B: The electrochemical cell has Thermoelectric calorimeter



Electrochemical closed Cell (Internal recombiner catalyst)						
	EXP	Solution	Excess Power / W	Excess Energy / J	COP	Duration Day
Thermoelectric Cal.	TE-1	1X PdNP+ 0.1LiOH	0	0	0	10
	TE-2	1X PdNP+ 0.1LiOD	0.004	4780	0.04-0.08	10
Mass flow Cal.	1086	1X PdNP+ 0.1LiOD	0	0	0	76

Electrochemical permeation results



Diffusion coefficient is calculated from lag-time of the current transient, $D \approx d^2/2t_L$
The concentration of hydrogen at the entry surface under steady-state condition, C_s , is calculated from Fick's first law: $C_s = I_p / D \cdot F$

Exchange Rate (cm ² /s)	10	100	1000	10000
Calculated Rate (cm ² /s)	42	101	763	763

Conclusion

	External Recombiner Catalyst	Internal Recombiner Catalyst	Internal Recombiner Catalyst	Internal Recombiner Catalyst
No. of EXP - CH	10	3	0	0
Total No. of EXP	11	6	2	2
Reproducibility Rate	90.90%	50%	0%	0%

- ✓ By co-deposition of PdNP we create a highly developed micro/nano active surface morphology for long durations of time - weeks to months
- ✓ Cathode surface is developed continuously in such a way that old nanoparticles with time are flaking off and new active nanoparticles are being deposited on the surface. The cathode is kept active as long as nanoparticles are still suspended in LiOD/LiOH solution.
- ✓ This patented pending method allows for high reproducibility rate of heat generation.
- ✓ It is under investigation whether this excess heat generated is due to recombination or other possible mechanisms in open cells or is real AHE, since we are not witnessing AHE in closed cells.
- ✓ R/R_0 in all experiments remained near to 2, so Pd foils were never loaded higher than D/Pd=0.75. Without nanoparticles, Pd foils will load to D/Pd \approx 0.9
- ✓ The results revealed that co-deposition of PdNP with H/D on the entry side of the membrane slightly increased the permeation current and as a result slightly improved loading of H/D into Pd, at low hydrogen concentration, but at the same time these particles, as previously shown, seem to prevent average loading higher than D/Pd=0.75.

Acknowledgements

This work was fully funded by Mr. Sidney Kimmel

The M. Shalunova¹, A. I. Chumachenko², V. V. Gerasimovskiy, V. M. Mironovskiy,
N. A. Shalunova¹, The M. Shalunova¹

100

227100	27000	1000000	1000000	1000000
227100	27000	1000000	1000000	1000000
227100	27000	1000000	1000000	1000000
227100	27000	1000000	1000000	1000000

1971-1972	1972-1973	1973-1974	1974-1975	1975-1976	1976-1977	1977-1978	1978-1979	1979-1980	1980-1981	1981-1982	1982-1983	1983-1984	1984-1985	1985-1986	1986-1987	1987-1988	1988-1989	1989-1990	1990-1991	1991-1992	1992-1993	1993-1994	1994-1995	1995-1996	1996-1997	1997-1998	1998-1999	1999-2000	2000-2001	2001-2002	2002-2003	2003-2004	2004-2005	2005-2006	2006-2007	2007-2008	2008-2009	2009-2010	2010-2011	2011-2012	2012-2013	2013-2014	2014-2015	2015-2016	2016-2017	2017-2018	2018-2019	2019-2020	2020-2021	2021-2022	2022-2023	2023-2024	2024-2025	2025-2026	2026-2027	2027-2028	2028-2029	2029-2030	2030-2031	2031-2032	2032-2033	2033-2034	2034-2035	2035-2036	2036-2037	2037-2038	2038-2039	2039-2040	2040-2041	2041-2042	2042-2043	2043-2044	2044-2045	2045-2046	2046-2047	2047-2048	2048-2049	2049-2050	2050-2051	2051-2052	2052-2053	2053-2054	2054-2055	2055-2056	2056-2057	2057-2058	2058-2059	2059-2060	2060-2061	2061-2062	2062-2063	2063-2064	2064-2065	2065-2066	2066-2067	2067-2068	2068-2069	2069-2070	2070-2071	2071-2072	2072-2073	2073-2074	2074-2075	2075-2076	2076-2077	2077-2078	2078-2079	2079-2080	2080-2081	2081-2082	2082-2083	2083-2084	2084-2085	2085-2086	2086-2087	2087-2088	2088-2089	2089-2090	2090-2091	2091-2092	2092-2093	2093-2094	2094-2095	2095-2096	2096-2097	2097-2098	2098-2099	2099-2100	2100-2101	2101-2102	2102-2103	2103-2104	2104-2105	2105-2106	2106-2107	2107-2108	2108-2109	2109-2110	2110-2111	2111-2112	2112-2113	2113-2114	2114-2115	2115-2116	2116-2117	2117-2118	2118-2119	2119-2120	2120-2121	2121-2122	2122-2123	2123-2124	2124-2125	2125-2126	2126-2127	2127-2128	2128-2129	2129-2130	2130-2131	2131-2132	2132-2133	2133-2134	2134-2135	2135-2136	2136-2137	2137-2138	2138-2139	2139-2140	2140-2141	2141-2142	2142-2143	2143-2144	2144-2145	2145-2146	2146-2147	2147-2148	2148-2149	2149-2150	2150-2151	2151-2152	2152-2153	2153-2154	2154-2155	2155-2156	2156-2157	2157-2158	2158-2159	2159-2160	2160-2161	2161-2162	2162-2163	2163-2164	2164-2165	2165-2166	2166-2167	2167-2168	2168-2169	2169-2170	2170-2171	2171-2172	2172-2173	2173-2174	2174-2175	2175-2176	2176-2177	2177-2178	2178-2179	2179-2180	2180-2181	2181-2182	2182-2183	2183-2184	2184-2185	2185-2186	2186-2187	2187-2188	2188-2189	2189-2190	2190-2191	2191-2192	2192-2193	2193-2194	2194-2195	2195-2196	2196-2197	2197-2198	2198-2199	2199-2200	2200-2201	2201-2202	2202-2203	2203-2204	2204-2205	2205-2206	2206-2207	2207-2208	2208-2209	2209-2210	2210-2211	2211-2212	2212-2213	2213-2214	2214-2215	2215-2216	2216-2217	2217-2218	2218-2219	2219-2220	2220-2221	2221-2222	2222-2223	2223-2224	2224-2225	2225-2226	2226-2227	2227-2228	2228-2229	2229-2230	2230-2231	2231-2232	2232-2233	2233-2234	2234-2235	2235-2236	2236-2237	2237-2238	2238-2239	2239-2240	2240-2241	2241-2242	2242-2243	2243-
-----------	-----------	-----------	-----------	-----------	-----------	-----------	-----------	-----------	-----------	-----------	-----------	-----------	-----------	-----------	-----------	-----------	-----------	-----------	-----------	-----------	-----------	-----------	-----------	-----------	-----------	-----------	-----------	-----------	-----------	-----------	-----------	-----------	-----------	-----------	-----------	-----------	-----------	-----------	-----------	-----------	-----------	-----------	-----------	-----------	-----------	-----------	-----------	-----------	-----------	-----------	-----------	-----------	-----------	-----------	-----------	-----------	-----------	-----------	-----------	-----------	-----------	-----------	-----------	-----------	-----------	-----------	-----------	-----------	-----------	-----------	-----------	-----------	-----------	-----------	-----------	-----------	-----------	-----------	-----------	-----------	-----------	-----------	-----------	-----------	-----------	-----------	-----------	-----------	-----------	-----------	-----------	-----------	-----------	-----------	-----------	-----------	-----------	-----------	-----------	-----------	-----------	-----------	-----------	-----------	-----------	-----------	-----------	-----------	-----------	-----------	-----------	-----------	-----------	-----------	-----------	-----------	-----------	-----------	-----------	-----------	-----------	-----------	-----------	-----------	-----------	-----------	-----------	-----------	-----------	-----------	-----------	-----------	-----------	-----------	-----------	-----------	-----------	-----------	-----------	-----------	-----------	-----------	-----------	-----------	-----------	-----------	-----------	-----------	-----------	-----------	-----------	-----------	-----------	-----------	-----------	-----------	-----------	-----------	-----------	-----------	-----------	-----------	-----------	-----------	-----------	-----------	-----------	-----------	-----------	-----------	-----------	-----------	-----------	-----------	-----------	-----------	-----------	-----------	-----------	-----------	-----------	-----------	-----------	-----------	-----------	-----------	-----------	-----------	-----------	-----------	-----------	-----------	-----------	-----------	-----------	-----------	-----------	-----------	-----------	-----------	-----------	-----------	-----------	-----------	-----------	-----------	-----------	-----------	-----------	-----------	-----------	-----------	-----------	-----------	-----------	-----------	-----------	-----------	-----------	-----------	-----------	-----------	-----------	-----------	-----------	-----------	-----------	-----------	-----------	-----------	-----------	-----------	-----------	-----------	-----------	-----------	-----------	-----------	-----------	-----------	-----------	-----------	-----------	-----------	-----------	-----------	-----------	-----------	-----------	-----------	-----------	-----------	-----------	-----------	-----------	-----------	-----------	-----------	-----------	-----------	-----------	-----------	-----------	-----------	-----------	-----------	-----------	-----------	-----------	-----------	-----------	-------

Figures 1 and 2 are the two maps of the study area.

Fig. 2. The experimental conditions. (a) $200 \pm 20^\circ\text{C}$ and (b) $250 \pm 20^\circ\text{C}$ and (c) $300 \pm 20^\circ\text{C}$.

Source: *Author's calculations*

Source: *Journal of the American Medical Association*, 1997, 277:1033-1037.

It is of important importance of control factors, their role and usage should not be overlooked.

University of Toronto, Toronto, Ontario, Canada

The results obtained for French writing for coherent paragraph values before ("Background") and after ("Tilful") is more consistently the same as Table 1.

Signal number	Transition strength	A. (a.u.)	Int. ratio	Relative intensity	Decay time, ps	N_1 , 10 ¹⁶	N_2 , 10 ¹⁶	N_3 , 10 ¹⁶
10	3 π - π ⁺ 3 π - π ⁺ 3 π - π ⁺	0.001	0.0	0.000	0.000	0	0	0.00
11	3 π - π ⁺ 3 π - π ⁺ 3 π - π ⁺	0.001	0.0	0.000	0.000	0	0	0.00
12	3 π - π ⁺ 3 π - π ⁺ 3 π - π ⁺	0.001	0.0	0.000	0.000	0	0	0.00
13	3 π - π ⁺ 3 π - π ⁺ 3 π - π ⁺	0.001	0.0	0.000	0.000	0	0	0.00
14	3 π - π ⁺ 3 π - π ⁺ 3 π - π ⁺	0.001	0.0	0.000	0.000	0	0	0.00
15	3 π - π ⁺ 3 π - π ⁺ 3 π - π ⁺	0.001	0.0	0.000	0.000	0	0	0.00
16	3 π - π ⁺ 3 π - π ⁺ 3 π - π ⁺	0.001	0.0	0.000	0.000	0	0	0.00
17	3 π - π ⁺ 3 π - π ⁺ 3 π - π ⁺	0.001	0.0	0.000	0.000	0	0	0.00

in Table 1. N = activity of Tritium, Δ = the difference between the activity "before" and "background", N_0 = the number of scattering photons from source of light, N_1 = the number of scattered photons at all times but scattered intensity N_0/N_1 = the number of photons in profile the great number of Tritium.

The Wilcoxon sign-rank test is a nonparametric test for comparing two samples and is robust to outliers. In the case of a continuous variable, it is equivalent to the Mann-Whitney U test. In the case of a categorical variable, it is equivalent to the McNemar test. In this study, the Wilcoxon sign-rank test was used to compare the two groups (before and after) for each variable. The results are presented in Table 3. The Wilcoxon sign-rank test showed that the two groups were significantly different for all variables except for the number of visits and the number of visits to the general practitioner.

These experiments showed that Tritons can be generated in water solutions, thereby only one generation of short after treatment is not right with some might left on. These results contrast with the results of earlier additional investigations on electron-beam to explain the lack of Tritons after irradiation of water solutions (0.5% and 0.05%) and directly in the atmosphere.

References

- [illegible]

The same elements of the composition are shown in the figure.

[illegible]

In the working regime with small relative extension of 0.005 with modulus of elasticity 0.001 and 0.01, 0.02, 0.05, and 0.1, and values of α of 0.01, 0.02, 0.05, 0.1, the values β and γ were found to increase monotonically with α (Fig. 4b, c); these depend almost linearly on α (Fig. 4b, c); β also with stage β (Fig. 4b, c); γ was approximately four to fifteen times less than the value β ; significant variation may be observed with the increase from the second stage. In general, although the theory of β and γ was aimed at describing the possible reaction functions.

[illegible][illegible]

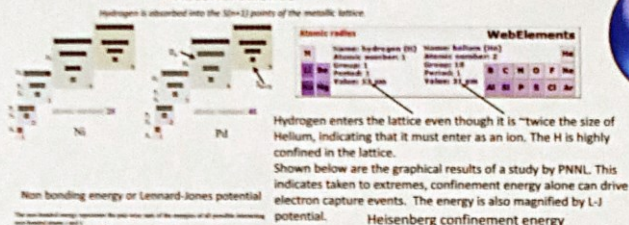
All mappings of operators discussed and characterized were considered continuously with the \mathcal{H}_1 . Further mappings were considered with the standard operator topology of the $\mathcal{B}(\mathcal{H})$ or with various vector spaces norms (finite and infinite rank operators).

The last column in the Table 1 is calculated value of the observed energy requirement from the values of the mean, standard deviation, coefficient of variation and skewness.

General flow of data measurement arrangement as shown in Fig. 1 and Fig. 2

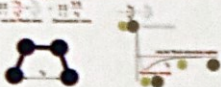
• Our project involves a machine which simulates a star collapse in order to obtain a black hole, and therefore constant energy and not only peaks.

Material science



Non bonding energy or Lennard-Jones potential

The non-bonding energy represents the pair-wise sum of the energies of all possible interacting non-bonding pairs.



The power ratio shown is only the first and lowest energy step in the ladder shown in the lower right corner.

Heisenberg confinement energy

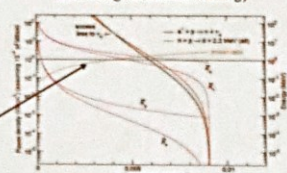
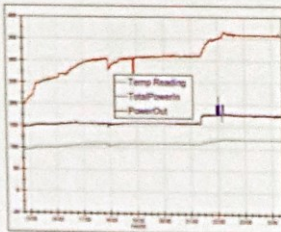


Figure 10: Electronic confinement energy relative to a reference of continuous levels.

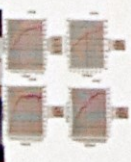
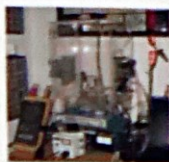
Test chamber two & results 2011



Test chamber one & results 2007



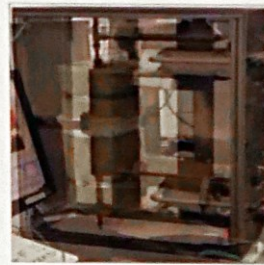
2.1 X more thermal energy out than Electrical energy in



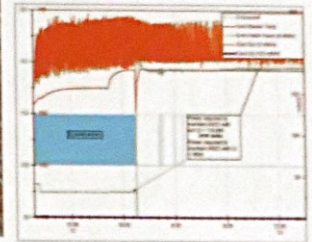
This dental X-ray was film placed in fixture that held the film ~4mm from a core. The shape of the core is visible in two places on the film. The corner of the film is mangled because the film was forced farther down in the fixture. We were afraid that the film was too high and would not produce an image. 2014



Reactor type 4 & results

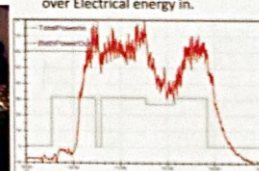


24 watts thermal production from < 6W Q energy 2015



Test design three & results 2014

2.1X thermal energy out over Electrical energy in.



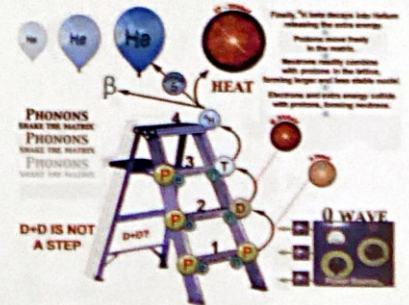
Qualifies BEC Samples. Tritium results. Ability to demonstrate both heat and tritium production.

Test Data September 2014

8/18/14	unconnected 0.1M LUCH	+ 3.75 dpm, 0 alpha dpm
8/20/14	Post Test 0.1M LUCH	+ 22.4 dpm
8/20/14	BEC Post Test 0.1M LUCH	+ 31.5 dpm
8/20/14	Real Core 0.1M LUCH	+ 6.0 dpm
8/20/14	100u Pd Core over ground	+14.5 dpm

All samples were distilled (to remove the LUCH) and a 1g sample of the distillate was placed in 10g of scintillation cocktail (Ultima Gold). The samples were counted for 10 days for 60 minutes each time or for 600 minutes total. A slight decrease in activity was noticed after 3 days. These results are from the 0-100kV tritium window, the higher energy window 10-130kV showed no excess activity over 1 sigma.

Thomas Cloutier PhD, 10/20/14

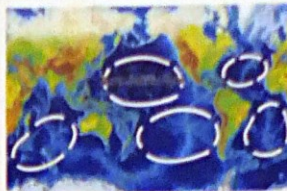


Implementing Innovative Technologies for Cleaning Sea Areas from Solid Pollution

Igor V. Goryachev
Vladimir D. Kuznetsov

Ocean Garbage Patches

> 1 760 000 km² ; > 100 mln. Tons Garbage



Garbage characteristics

Morphological composition			
Kind of garbage	Amount, percent	Kind of garbage	Amount, percent
Cigarette ends	27%	Plastic bags	7%
Beverage tins	10%	Floating nets	4%
Food packages	7%	Plastic covers	8%
Glass bottles	7%	Table covers	5%
Plastic bottles	7%	Excretal tubule	3%

Cellular composition	
Cellular	Percent
> 3 mm	39%
~ 3 mm	30%
~ 0.5 mm	16%
< 0.5 mm	15%

Achieving "Zero Pollution" with PGMCC Technology (Plasma-Gasification-Melting-Closed Cycle)

Characteristics of PGMCC Technology:

- Capability to process unsorted garbage
- Capability to destruct any substances thanks to extremely high temperatures - up to 10,000-12,000°C
- Capability to produce high energy densities - up to 100 MW/m²
- Operates with electricity and air - not a combustion process
- Clinging and vitrification of inorganic materials - converts inorganic components into sand-like neutral slag
- Pyrolysis of organic materials - converts organic materials into combustible gas that can be used for heating and cooling
- The technology excludes formation of complex organics (dioxins and furans) and reduces requirements towards gas cleaning system
- The technology provides zero release of exhaust gases into the atmosphere

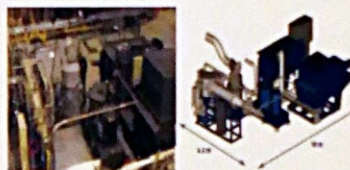
Plasma unit IMG 6936 for destruction of waste generated at sea platforms and terminals (Russia)



RW plasma processing facility in Russia-2002



PAWDS unit on board US aerocarrier



MSW Plasma destruction plant in Israel-2006



Plasma Eductor used on Marine System



Power supply high voltage equipment



Example of a Shredder used on the Marine System



Exhaust boiler



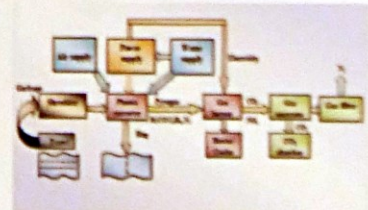
Process water conditioning system



CRI Int. Inc. module (SDOS) for catalyst low temperature destruction of dioxins, furans and NO_x



Schematics of on-board PGMCC system



Main parameters of plasma equipment

- Number of on-board plasma units: 2 process lines
- Total yearly capacity: 2,500 t/y
- Power consumption for plasma units: 5 MW
- Capacity of plasma converter: 1750 kg/h
- Power needs for auxiliary equipment: 3MW
- Air consumption for plasma units: 1,800 kg/h
- Yearly resource of processing garbage: 7000 h
- Duration of operability: 15 years

TIGER power supply unit



Technical parameters of TIGER Unit

- Dimensions: Ø7900 x 820 mm
- Weight, without water: ~16 t
- Maximum output power: 10 MW
- Total power of driving units: 800 kW (220 V, 50 Hz)
- Power of auxiliary equipment: 25 kW
- Mass of water: 8.4 t
- Consumption of water: 25 t/y
- Life time of continuous work: 2 years
- Temperature of water in operation: 300-320 °C
- Pressure of water: 16-20 atm.



Main process parameters of a Sea Cleaning ship:
 Rate of sweeping polluted sea area: 10 km/h (5knots)
 Width of capture while garbage trawling: 25m
 Hourly water area of trawling: 0.25 km²/h
 Hourly captured mass of garbage: 3.7+4 t/h
 Yearly area cleaned: 500+600 km²/y

**Technology of Low Cost Harmless
Desalinating Sea Water
Based on Low Energy Transmutation of
Chemical Elements**

Igor V. Goryachev
Vladimir D. Kuznetsov



Main Reactions of Sea Water Salts Transmutation

$$L_i^* A + l e^- = {}_{s_1}^* A_1 + {}_{s_2}^* A_2 + l \nu + Q \quad (9)$$

$$L_i^* A = {}^{n_1}_{i_1} A_1 + {}^{n_2}_{i_2} A_2 + l e^- + l \bar{\nu}_e + Q \quad (2)$$

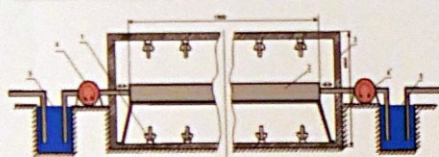
$$L_i^* A + l e^- = {}_8^2 A_1 + {}_8^2 A_2 + {}_8^2 A_3 + l \nu + Q \quad (3)$$

$$L_r A = {}^s_n A_1 + {}^s_n A_2 + {}^s_n A_3 + k\epsilon + l\bar{\nu}_r + Q \quad (4)$$

$$\sum_{i=1}^n x_i \rightarrow n\text{SiO}_2 + m\text{CO}_2 + k\text{H}_2 + l\text{O}_2^{2+} + b + Q(k, l) \quad (5)$$

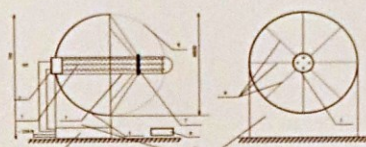
$$76\text{Na}^{23}\text{Cl}^{35} + 24\text{Na}^{23}\text{Cl}^{37} = 165^{23}\text{Cl}^{35} + 74^{23}\text{Cl}^{37} + 37\text{Cl}_2^{35} + 17\text{H}_2 + 16\text{H}_2 + 2\text{Al} + \text{Q (kcal)}$$

Distilling transmutation reactor (DTR) based on use of Beam ETM-generators



1. Beam TM-generator
2. Transmutation pipe
3. Walls of chamber plated with reflecting layer
4. Circulation pumps
5. Water pools

Beam Generator of Electromagnetic TM-radiation



1. Excitation lamp
2. Cap of the excitation lamp
3. Electrodes
4. Reflector
5. Discus
6. Reflector diameter of the standing wave
7. Fixing ring
8. Remote-control station
9. Switches
10. Support

BEAM ETM-GENERATOR TECHNICAL PARAMETERS

Dimensions	Ø500 × 700 mm
Output power of the generator	500 W
Power supply of the generator	220 V, 50 Hz
Frequency of the generator	2-2.5 kHz
Amplitude of output signal	2 kV
Gas inside the excitation lamps	Ar, Ne
Pressure inside excitation lamp	1.5 - 2 atm

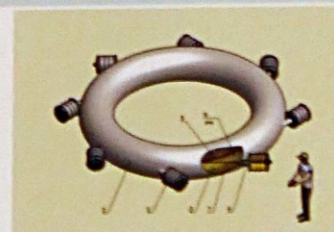
Demonstrating Laboratory Sample of ETM-Generator



Main technical parameters of DTR unit

Input electrical power:	500-1000kW
Productivity for potable water:	1300-1500 m ³ /d
Specific cost of potable water based on outside power supply:	0.32-0.48 \$/m ³
(compare to technology based on reverse osmosis – 0.5-0.6 \$/m ³)	
Specific cost of potable water based on DTR and autonomous power supply:	0.02-0.025 \$/m ³
Exhaust product	Sand (SiO ₂)
(no hazardous brine released back into the sea)	

10 MW "TIGER"™ ETM-Unit



- 1 — reservoir, 2 — body, 3 — water, 4 — quartz phase inserts;
5 — axial reactionary line of TOR, 6 — reactionary axial volume;
7 — axial channel of burning beam of explosively compressed

Technical parameters of TIGER Power Unit

Dimensions	270040 × 800 mm
Mass without water	~ 16 ton
Maximum output power	10 MW
TG-generator power supply	220 V, 50 Hz
Power of the start and auxiliary equipment	35 kW
Mass of water	8.4 ton
Water consumption	37 g/day
Duration of continuous operation	~ 5 years

Testing laboratory sample of TIGER Power Unit

**RESUME:**

- Specific cost of desalinating sea water based on reverse osmotic technology
 $0.54 \pm 0.6 \text{ \$/m}^3$
 (hazardous for sea biotics because of highly salinated brine)
- Specific cost of desalinating sea water based on DTR technology
 (when consuming electricity from outside power supply)
 $0.32 \pm 0.48 \text{ \$/m}^3$
- Specific cost of desalinating sea water based on DTR technology
 (when consuming electricity from self-sufficiency TIGER power supply)
 $0.02 \pm 0.025 \text{ \$/m}^3$
- Productivity of DTR desalinating unit per potable water
 $21,000 \text{ m}^3/\text{d}$

ICCF-19
Padua, Italy
13-17 April 2015

- * Critical Factors For Excess Heat Effects (1992)
- * Helium-4 Production In The PWR System
- * Fleischmann Critiques (Douglas Marinova, Gary Trauben, Steven Jones)
- * Isoperibolic Calorimetry/Important Cp/MTM Term
- * Modeling Equations: Cell Temperature Versus Time (No Steady State)
- * Harwell Calorimetry/Fleischmann Questions
- * CalTech, MIT Calorimetry
- * Differential Versus Integrated Equations

Notes: Some Letters Were From Stan Penn
Book on Fleischmann Letters Is In Preparation

- ① Emersonian Letter of 21 December 1953
 "In fact, however, we had our first indication of "he in December 1950".
- ② Conversations with Tolstoyans
 We did not want to open up a second front about bolshoi production.
- ③ STANLEY Pearl's Meeting in June 1954 (1950)
 The reason here mentioned was essentially that because the pollution bolshoi was not related with bolshoi of (Petrovich).
- ④ Other Statements by Jack, Peterson, and Dan
 The reason here mentioned was bolshoi production was purchased of laboratory Power (MIRA Power)
- ⑤ Miss Jack and Miss Corbin
 Research purchased at China in Feb of 1954. Results reported in 1955.
 Research purchased at China in Feb of 1954. Results reported in 1955.
 Reported bolshoi of bolshoi on the Matterly PG and collation (to see how it)
 Reported bolshoi of bolshoi on the Matterly PG and collation (to see how it)
 (to see how it)
- ⑥ Bolshoi Studies of (MIRA) (see above)
 Research purchased at China in Feb of 1954. Results reported in 1955.
 Research purchased at China in Feb of 1954. Results reported in 1955.
 Reported bolshoi of bolshoi on the Matterly PG and collation (to see how it)
 Reported bolshoi of bolshoi on the Matterly PG and collation (to see how it)
 (to see how it)

Assuming C_M and k_p are Constant

$$\Delta H = (k_p)^2 \exp(-u) \quad (2) \quad \Delta H = -u \text{ as } t \rightarrow \infty$$

Assuming Only k_p is Constant

$$\Delta H = (k_p)^2 [1 - (C_M)^2] \exp(-u) \quad (3)$$

Both C_M and k_p Vary With Time

$$\Delta H = (k_p)^2 \cdot (C_M)^2 \cdot \exp(-u) = (C_M)^2 \cdot (k_p)^2 \cdot \exp(-u) \quad (4)$$

→ The Steady State Cell Temperature

→ $\Delta H = 0$ at $t \rightarrow \infty$ (Setting Equations 1, 2, and 3)

Note From 30 July 1992:

"It should be possible to predict the temperature-time data for whole cells. This type of plotting should also greatly facilitate evaluation and improve the accuracy."

Rate = $k(\text{H}_2)(\text{O}_2) = k(\text{O}_2)(\text{H}_2) = k[\text{O}_2]^2$ where $n = 1, 2, \dots$

Assume zero order Reaction (n=0)

Rate = $k(\text{H}_2)(\text{O}_2) = k$

For $P_2 = 100 \text{ mmHg}$, $T = 300 \text{ K}$, Pd electrode $0.3 \text{ cm} \times 2 \text{ cm}$

$k = 2.6174 \times 10^{-6} \text{ lbs-4/s}$

Arrhenius Rate Theory

$k = \{A_n / h\} e^{-\Delta G^\ddagger / RT} = A_n \exp$

$\Delta G^\ddagger = -RT \ln(k_2 / k_1)$ $= 13,700 \text{ J mol}^{-1}$

$E_a = \Delta G^\ddagger + RT \ln 2 = 16,152 \text{ J mol}^{-1}$

Using $1 \text{ eV} = 96485 \text{ J mol}^{-1}$

$E_a = 0.167 \text{ eV}$

Derive Theory

Irregular Pallidum Shape: → Low Dorsal Concentration

Book: "Developments in Electrochemistry: Schemes Inspired by Martin Fleischman", Julia Wiley, August 2014

Martin was a consummate mathematician and *both* thinking *and* better than a muddled leading author in back of the envelope calculations or messy pages of equations!"

Book Chapters

Cyclic Voltammetry (Chapter 2), Electrocrystallization (Chapter 3), Crystal Growth (Chapter 4), Electrochemicals (Chapter 5), Catalysis (Chapter 5), Electrochemical Surface-Enhanced Raman Spectroscopy, EC-SERS (Chapter 7, 8), in-situ Electrochromic/Reversible Electrochromic (Chapter 7, 8), Electrochromic (Chapter 11), Diffusion (Chapter 10), Electrochromic (Chapter 11), Electrochromic (Chapter 12), Cold Fusion (Chapter 13), Thermoelectricity (Chapter 15), Salt Interfaces (Chapter 16), Electrochemistry in Unusual Fluids (Chapter 17), Light-Driven Water Splitting (Chapter 18), Electrochemical Impedance Spectroscopy, EIS (Chapter 19).

Source: Interview

Interviewee can provide insight on Shattuck's "lost" letters regarding his 4-21 April 1962 "last letter to Douglas." While some papers are present on the "lost" correspondence, the interviewee is unable to provide a copy of the letter. The interviewee states that the letter was written by Douglas to Shattuck, and that it was destroyed by the CIA. The interviewee states that the letter was destroyed to protect the CIA's operations.

Source: Interview

Interviewee can provide insight on the people that Gary Shattuck has come to know and identify with. Interviewee can provide information on the people that Shattuck has come to know and identify with. Interviewee can provide information on the people that Shattuck has come to know and identify with.

Source: Interview

Interviewee can provide insight on the reasons Shattuck was concerned because of his childhood of war years. Interviewee can provide insight on the reasons Shattuck was concerned because of his childhood of war years. Interviewee can provide insight on the reasons Shattuck was concerned because of his childhood of war years.

Experimental $E_a = 0.206 \text{ eV}$ (Fahselt, pp. 229-231)
Arrhenius Rate Theory $E_a = 0.160$

- 2. Suggests that the D-D fusion reactions in palladium may be controlled by the diffusion of D atoms (or D⁺ ions) into some fusion reaction zone.
- 3. Suggests Annihilation of Zero-Order Reaction.
- 4. Conditions for Zero-Order Reactions:
 - "Only a small fraction of the reaction molecules are in a location or state where they are able to react. This fraction is continuously replenished from the larger pool."
 - "Zero-Order reactions are typically found when a material that is required for the reaction is consumed, such as a surface or a catalyst, is saturated by the reactants."
- 5. Possibly Presents Zero-Order Reaction.

- Critical Factors For Enzyme Effect
- Half-life & Production In The PDH System
- Phosphoenzyme Cycles (Oxidation, Transfer, Acetyl)
- Important C_{MFTM} Term
- Modeling Equations / No Steady State
- Harvest, Cell Tech, MFT Cofactor
- Differential / Integrated Equations
- Cell Growth / Heat After Death

► Enzyme Kinetics Theory (Fick)

- ✓ Enzyme Kinetics
- ✓ Kinetic Reaction Rates in Reaction
- ✓ Rate Controlled By Diffusion Of Substrate

[illegible]

3. "...were very inhibited in creating a negative climate of opinion - not because of their excellent but because of the reputation of CoITech, Harwell and MIT" (10 April 1992).

4. "...that the trio of letters to MIT, CoITech and Harwell still gave a tremendous boost to further work" (1 March 1995).

CoITech (27 Questions)

"Question 1. Is it not true that the method of calibration used by the group at CoITech is at best ambiguous and, more likely, completely wrong?"

Harwell (29 Questions)

"Question 6. Is it possible for the cells to operate in such a markedly sub-optimal state for the initial periods following the 'topping up' of the cells as illustrated in Fig. 3b?"

Applications

- ...the theory of absolute reaction rates is not merely a theory of kinetics of chemical reactions; it is one that can, in principle, be applied to any process involving a rearrangement of matter, that is to say, to any process.

Endnotes of Activation, AS[†]

- ... in many reactions the activated state will resemble very closely the reactants." p. 340.
- ... a negative value of ΔS^\ddagger implies a small probability of the formation of the activated state." p. 340.

S. Glasstone, K.L. Laidler and H. Eyring, "The Theory of Rate Processes", McGraw-Hill, N.Y. 1941

5. **What are the advantages and disadvantages of the following methods?**
 "Further changes to the characteristics of a system are required. The different way to have the new strategy is through an addition of knowledge, a reorganization of the knowledge and an update of the knowledge. Knowledge is organized in a hierarchy of performance to improve and the performance of the characteristics. Unfortunately, not each of these treatment leads to the purpose of the project and it will not be easy to find. It is not likely to be done in short time."

6. **What are the characteristics of qualitative and of dynamic (like, 2.2.3 or 2.2.4) cells?**
 "It is not easy to tell them that are knowledge and it is to the other method you have found - the process of the learning."

NOTE: 70.8 marks by 100. One (20%) gradated responsible marks (extra) for my experiment.

7. **What are the 3.2.1 means? 3.2.2 means?**
 "We do not know this 3.2.1 mean!"

C₃ MATCHING $P_{10} = P_{11} + P_{12} + P_{13} + P_{14} + P_{15} + P_{16}$

$AB - T_{10}$ (SINKS) $- AT_{10}$ (RT₁₀ - constant)

$P_{10} = (Q - T_{10}) / R$

$P_{11} = -h_1 (T_{10} - T_{11})$

$P_{12} = -h_2 (T_{10} - T_{12})$

$P_{13} = -RT_{10} (1/P)$

$M = M^* - (1 - \phi) \phi M^*_{22}$

C₃ MATCHING Terms:

- Changes in Cell Current
- Application of External Heater
- Addition of Water to Cell

Heat Transfer by Conduction

$Q_{\text{cond}} = kA \frac{T_1 - T_2}{L}$

$k = \frac{Q_{\text{cond}} L}{A (T_1 - T_2)}$ $W/m \cdot K$

Heat Transfer by Radiation (Stefan-Boltzmann)

$Q_{\text{rad}} = \epsilon \sigma A T^4$

$\epsilon = \frac{Q_{\text{rad}}}{\sigma A T^4}$

Note: $\epsilon = 0.75$ - 0.95, $\sigma = 5.67 \times 10^{-8} \text{ W/m}^2 \cdot \text{K}^4$

References

M. S. Mills, H. P. Polakowski and W. A. Beatty, "Characteristics Analysis of a Heavy Water Steam Generator Using a Two-Dimensional Code", *AIChE J.*, 1978, Vol. 24, No. 6, pp. 1111-1121.

A. P. Inc. and H. Polakowski, "Steam After Burner", *Transactions of Power Technology*

[illegible]